Multidisciplinary Design Optimization of Composite Spacecraft Structures using Lamination Parameters and Integer Programming

Pranav Sanjay Borwankar

Dissertation submitted to the Faculty of the

Virginia Polytechnic Institute and State University

in partial fulfillment of the requirements for the degree of

Doctor of Philosophy

in

Aerospace Engineering

Rakesh K. Kapania, Chair

Gary D. Seidel

Mayuresh J. Patil

Manish Bansal

Daisaku Inoyama

May 4, 2023

Blacksburg, Virginia

Keywords: Integer programming, composites, multidisciplinary design optimization, spacecraft structures, structural analysis, thermal analysis

Copyright 2023, Pranav Sanjay Borwankar

Multidisciplinary Design Optimization of Composite Spacecraft Structures using Lamination Parameters and Integer Programming

Pranav Sanjay Borwankar

(ABSTRACT)

The digital transformation of engineering design processes is essential for the aerospace industry to remain competitive in the global market. Multidisciplinary design optimization (MDO) frameworks play a crucial role in this transformation by integrating various engineering disciplines and enabling the optimization of complex spacecraft structures. Since the design team consists of multiple entities from different domains working together to build the final product, the design and analysis tools must be readily available and compatible. An integrated approach is required to handle the problem's complexity efficiently.

Additionally, most aerospace structures are made from composite panels. It is challenging to optimize such panels as they require the satisfaction of constraints where the design ply thicknesses and orientations can only take discrete values prescribed by the manufacturers. Heuristics such as particle swarm or genetic algorithms are inefficient because they provide sub-optimal solutions when the number of design variables is large. They also are computationally expensive in handling the combinatorial nature of the problem.

To overcome these challenges, this work proposes a two-fold solution that integrates multiple disciplines and efficiently optimizes composite spacecraft structures by building a rapid design framework. The proposed model-based design framework for spacecraft structures integrates commercially available software from Siemens packages such as NX and HEEDS and open-source Python libraries. The framework can handle multiple objectives, constraint non-linearities, and discrete design variables efficiently using a combination of black-box

global optimization algorithms and Mixed Integer Programming (MIP)-based optimization techniques developed in this work. Lamination parameters and MIP are adopted to optimize composite panels efficiently.

The framework integrates structural, thermal and acoustic analysis to optimize the spacecraft's overall performance while satisfying multiple design constraints. Its capabilities are demonstrated in optimizing a small spacecraft structure for required structural performance under various static and dynamic loading conditions when the spacecraft is inside the launch vehicle or operating in orbit.

Multidisciplinary Design Optimization of Composite Spacecraft Structures using Lamination Parameters and Integer Programming

Pranav Sanjay Borwankar

(GENERAL AUDIENCE ABSTRACT)

The design of new spacecraft takes several years and requires significant resources. The primary design objective is to minimize spacecraft mass/cost while satisfying the mission requirements. This is done by altering the structure's geometric and material properties. Most spacecraft panels are made from composite materials where the orientations of fiber paths and the thickness of the panel determine its strength and stiffness. Finding the best values for these parameters cannot be done efficiently using existing optimization algorithms, as several combinations of orientations can give a similar performance which can be subpar. In this dissertation, mathematical programming is adopted for fast evaluation of optimum panel properties, thereby saving a significant amount of resources compared to conventional techniques. Moreover, the requirements that govern the design process are handled one at a time in an organization. This leads to discrepancies in the various teams' designs that satisfy all requirements. A framework is built to integrate all requirements to account for their conflicting nature and quickly give the best possible spacecraft structural design configuration.

Dedication

To my parents, Pallavi Borwankar and Sanjay Borwankar.

Acknowledgments

I would like to express my heartfelt gratitude to all those who have supported me throughout my journey in pursuing my Ph.D. degree.

Firstly, I would like to thank my advisor, Dr. Rakesh K. Kapania, for his invaluable guidance, unwavering support, and endless encouragement throughout my Ph.D. journey. I am grateful for his patience, wisdom, and willingness to share his knowledge and expertise. I have learned so much from him, not just about the research topic but also about life and career. I would like to thank him for believing in me and pushing me to achieve my full potential.

I would also like to thank Dr. Manish Bansal for his valuable input, support, and guidance throughout my research. His expertise in Integer Programming has been immensely helpful in shaping my research ideas and provided me with a wider perspective on the subject. I appreciate his generosity, kindness, and willingness to lend a helping hand whenever I needed it.

I would like to extend my appreciation to Dr. Gary D. Seidel and Dr. Mayuresh J. Patil for their time, effort, and expertise in providing feedback and suggestions to improve my research. Their input has been crucial in shaping the direction of my work, and I am honored to have had the opportunity to learn from them.

I would like to express my gratitude to Dr. Daisaku Inoyama and Dr. Tom Stoumbos, who collaborated with me on my research. Their support and involvement in my research have been instrumental in enriching my understanding of the spacecraft industry, and their feedback has helped me to align my research to meet the industry's needs. Additionally, I would like to thank Northrop Grumman and Siemens for providing me with the necessary

tools and resources to carry out my research.

My appreciation also goes to our structures group members, whose insightful comments, feedback, and discussions have helped to shape my ideas and refine my research. I am thankful to my colleagues/friends, Srivatsa Bhat, Sudharsan Parthasarathy, Mayank Agarwal, and Varakini Sanmugadas, for their friendship, support, and camaraderie. Their feedback, encouragement, and lively discussions have made my graduate experience all the more enjoyable and rewarding.

I would like to extend my appreciation to my friends, who have been a source of comfort and encouragement throughout my graduate studies. Their unwavering support and understanding have made the challenges of graduate school easier to overcome.

I am grateful to Virginia Tech for providing me with the resources, opportunities, and support necessary to complete my degree. The administrative staff, faculty, and other graduate students have been instrumental in creating a supportive and intellectually stimulating environment in which to work and learn.

Finally, I would like to express my heartfelt gratitude to my parents for their unwavering love and support throughout my life. Their sacrifices, encouragement, and guidance have been instrumental in shaping me into the person I am today, and I am forever grateful for their love and support.

Thank you all for your contributions to my academic and personal growth.

Contents

List of Figures xiii

List of Tables xviii

1 Introduction 1

1.1 Overview of Model-Based Space System Design 1

1.2 Design Structure Matrix Representation for MDO 6

1.3 Overview of MDO in Aerospace Applications 8

1.4 The Role of MDO in Spacecraft Structural Design 11

1.5 Use of Mixed Integer Programming for Composite Structure Optimization . 14

1.6 Research Overview 19

2 Optimization of Composite Laminates with Uniform ply Thickness 22

2.1 Laminate Analysis 23

2.2 Constraint Formulation using Binary Variables 26

2.2.1 Buckling Constraints Formulation for Stacking Sequence Optimization 26

2.2.2 Strain Constraint Formulation for Stacking Sequence Optimization . 28

2.2.3 Buckling Constraints Formulation for Ply Thickness Optimization . . 30

2.2.4 Strain Constraints Formulation for Ply Thickness Optimization . . . 32

2.3 Optimization Problem Formulation 33

2.3.1 Buckling Load Maximization - Single Level Optimization 1 (SLO1) . 33

2.3.2 Weight Minimization - Single Level Optimization 2 (SLO2) 34

2.3.3 Weight Minimization - Sequential Two-Level Optimization (STLO) . 35

2.4 Laminate optimization with Uniform Ply Thickness 37

2.4.1 Optimization for Maximum Buckling Load Design using SLO1 37

2.4.2 Optimization for Minimum Weight Design using SLO2 40

2.4.3 Optimization for Minimum Weight Design using Sequential Two-Level Approach (STLO) 43

2.4.4 Scalability with Problem Size 46

3 Optimization of Hybrid Composite Laminates with Distinct ply Thickness 48

3.1 Analysis of Hybrid Composite Laminates 48

3.2 Buckling Constraint Linearization for Stacking Sequence Optimization . . . 50

3.3 Buckling Constraint Linearization for Distinct Ply Thickness 53

3.3.1 Overview of Reformulation Techniques used for Constraint Linearization 54

3.3.2 Reformulation of Stiffness Parameters 58

3.3.3 Implementation of Cubic Linearization Techniques 61

3.4 Optimization Problem Formulation 62

3.5 Hybrid Laminate Optimization Results 64

3.5.1 Buckling Load Maximization (STLO Level 1) 64

3.5.2 Weight Minimization using Distinct Ply Thicknesses 68

3.5.3 Cost Minimization using Distinct Ply Thicknesses 71

4 Application of Integer Programming in the Optimization of Composite Structures 74

4.1 Lamination parameters and Stiffness of General Unidirectional Laminates . . 75

4.1.1 Feasible Regions in Lamination Parameter Space 77

4.1.2 Lamination Parameter Mapping 78

4.1.3 Mapping verification 81

4.2 Laminate Optimization Problem Formulation 81

4.3 Laminate Optimization with Lamination Parameters 84

5 Multidisciplinary Structural Analysis and Design Optimization (MSADO) Framework 88

5.1 MSADO Framework Description 89

5.1.1 Input and Pre-Processing 90

5.1.2 Normal Modes Analysis 90

5.1.3 Linear Static and Buckling Analysis with Mechanical Loads 93

5.1.4 Dynamic Analysis with Mechanical Loads 93

5.1.5 Acoustic Analysis 97

5.1.6 Orbital Heating Analysis 98

5.1.7 Thermal Mapping 102

5.1.8 Thermal-Stress Analysis 102

5.1.9 Response Evaluation 102

5.2 Multidisciplinary Design Optimization of Composite Laminate 103

5.2.1 Laminate Multidisciplinary Analysis Setup 104

5.2.2 Laminate Optimization with Direct Method 105

5.2.3 Individual Objective Maximization 105

5.2.4 Weight Minimization using MSADO Framework 107

6 Multidisciplinary Optimization of a Small Spacecraft 112

6.1 Finite Element Model 112

6.1.1 Component Description 112

6.1.2 Mesh and Assembly 119

6.1.3 Model Verification 124

6.2 Spacecraft Analysis Setup 131

6.2.1 Steady State Acceleration Loads 131

6.2.2 Sine and Random Loads 132

6.2.3 Shock Loads 133

6.2.4 Acoustic Loads 134

6.3 Spacecraft Optimization with Direct Method 135

6.3.1 Optimization Problem Formulation for Direct Method 135

6.3.2 MSADO Results with Direct Method 138

6.4 Spacecraft Optimization with Lamination Parameters and Mixed Integer Programming 143

6.4.1 Extension of Lamination Parameters to Thermal Analysis 144

6.4.2 Analysis of Sandwich Panels with Lamination Parameters 149

6.4.3 Optimization Problem Formulation with Lamination Parameters and Mixed Integer Programming 151

6.4.4 MSADO Results with Lamination Parameters and Mixed Integer Programming 153

7 Summary and Future Work **156**

7.1 Summary 156

7.2 Future Research Avenues 158

Bibliography **160**

List of Figures

1.1 Space System Design Architecture 3

1.2 Design Subprocess Flowchart 4

1.3 Leading MBSE Methodologies. (a) Harmony-SE process elements [1], (b) OOSEM System Development Process [2]. 5

1.4 Example Design Structure Matrix for Aircraft Design Problem [3]. 7

1.5 Example of an Extended Design Structure Matrix [4]. 8

1.6 Computational Design Environment for Composite Aircraft Wing Design [5] 9

1.7 MDO Framework for Supersonic Aircraft Optimization [6]. 10

2.1 Rectangular composite panel (a = 20 in., b = 5 in.) subjected to bi-axial loading. 23

2.2 Sequential two-level optimization process. 36

2.3 Scalability study; (a) Varying number of plies N_{max} and a fixed number of possible orientations $p = 3$, (b) Varying number of possible orientations p and a fixed number of plies $N_{max} = 100$. 47

3.1 Rectangular composite panel subjected to bi-axial loading. 49

3.2 Performance scaling comparison between GA and MILP for buckling load maximization of hybrid laminates with a minimum 50% GFRP plies, $N_x = N_y = 1\text{N/mm}$, $a/b = 2$. 67

4.1 General laminate stacking. 75

4.2 Mapping verification for the relationship between same-type lamination parameters 82

4.3 Mapping verification for the relationship between different-type lamination parameters 83

4.4 Schematic of an arbitrary composite panel. 84

4.5 FE model of a rectangular composite laminate. 85

4.6 Thickness convergence in lamination parameter optimization (step 1). 86

4.7 Thickness convergence comparison. 87

5.1 MSADO Design Structure Matrix. 91

5.2 Spacecraft subjected to acoustic excitation inside a launch vehicle. 97

5.3 Orbital heating of spacecraft. 98

5.4 MSADO Blueprint 103

5.5 Rectangular Composite Panel subjected to Bi-axial Loading. 104

5.6 Convergence plots for the objective and active constraints, (a) Objective convergence showing the total number of plies, (b) Buckling load factor convergence, (c) Fundamental frequency convergence, and (d) Buckling temperature factor convergence. 110

6.1 Spacecraft CAD Model. 113

6.2 Bus Schematic and stacking. 113

6.3 Closeout frame sections. 115

6.4 Closeout definitions for different panels. 115

6.5 Solar array schematic. 116

6.6 Electronic boxes. 117

6.7 Payload schematic. 117

6.8 Fuel tank schematic. 118

6.9 Adapter upper Ring Schematic. 119

6.10 Spacecraft mesh. 120

6.11 Spacecraft structural model assembly. 121

6.12 Fluid domain for the vibroacoustic model. 122

6.13 Vibroacoustic model setup. 122

6.14 Deployed spacecraft used in the thermal and thermo-elastic analysis. 123

6.15 Response output locations of spacecraft for dynamic analyses. 124

6.16 Schematic to show spacecraft center of mass for the baseline design. 126

6.17 Effective mass fraction of normal modes in each degree of freedom from 0 Hz to 600 Hz. 126

6.18 Normal modes of spacecraft with maximum modal mass participation in each degree of freedom. 127

6.19 Spacecraft array and cage modes. 128

6.20 Spacecraft subjected to unit acceleration load. 129

6.21 Acceleration spectral density at mount locations with different element size acoustic meshes. 130

6.22 Steady state acceleration load factors. Source: [7]. 132

6.23 Component resolution for different load cases. 132

6.24 Falcon 9 load factors for sine and random vibration analysis. Source: [7]. . . 133

6.25 Acceleration shock response spectrum [7] and synthesized time histories. . . 134

6.26 Vibroacoustic load model using distributed plane waves and sound pressure level. 135

6.27 Design variable description for spacecraft sizing optimization. 136

6.28 Design history plot for objective, frequency, shock acceleration, and thermal buckling factor. 139

6.29 Design history plot for panel wrinkling constraints. 140

6.30 Design variable history of study 2 for the number of plies and honeycomb core thickness of each panel group. 142

6.31 Design variable history of study 1 for panel fiber orientations. 143

6.32 Comparison of normal modes between baseline and optimal design. 144

6.33 Comparison of strain energy densities between baseline and optimal design corresponding to normal modes in 6.32. 145

6.34 Shock response comparison between baseline and optimal design. 146

6.35 Spacecraft modal density comparison. 147

6.36 Composite panel construction without and with honeycomb core. 150

6.37 Design variable description for the optimization of spacecraft with lamination parameters. 152

6.38 Convergence rate comparison between direct and lamination parameter based optimization. 154

List of Tables

2.1 Material properties for T300/5208 39

2.2 Maximum buckling load factor comparison using SLO1. 39

2.3 Optimal stacking sequence obtained using SLO1 (same sequence is obtained using both runs). 39

2.4 Minimum weight optimization with buckling constraints using SLO2. 42

2.5 Optimal stacking sequence obtained using SLO2 with buckling constraints (the same sequence is obtained using both runs). 42

2.6 Minimum weight optimization with buckling and strain constraints using SLO2. 42

2.7 Optimal stacking sequence obtained using SLO2 with buckling and strain constraints (the same sequence is obtained using both runs). 43

2.8 Optimal result comparison for case (a) using STLO. 44

2.9 Optimal result comparison (N=72, Θ set 2) using STLO. 45

2.10 Comparison between results obtained from SLO2 and STLO. 45

3.1 Design space comparison with linked and unlinked variables in distinct ply thickness optimization. 63

3.2 Material properties [8]. 64

3.3 Maximum buckling load factor comparison using STLO level 1, $N = 64$, $N_x = N_y = 1$N/mm, $a/b = 2$, Set 1 as Θ. 65

3.4 Optimal stacking sequence obtained using MILP for studies in Table 3.3. . . 66

3.5 Performance scaling comparison between GA and MILP for buckling load maximization of hybrid laminates with a minimum 50% GFRP plies, $N_x = N_y = 1$N/mm, $a/b = 2$. 66

3.6 Thickness optimization results using STLO level 2 - Non-hybrid laminates, $N_x = N_y = N_0$, $a/b = 2$ 69

3.7 Weight optimization results of hybrid laminates with distinct thickness, $N_x = N_y = N_0$ N/mm, $a/b = 2$, $N = 64$. 71

3.8 Optimal stacking sequence and thickness obtained using STLO for studies in Table 3.7. 71

3.9 Cost optimization results of hybrid laminates with distinct thickness, $N_x = N_y = N_0$ N/mm, $a/b = 2$, $N = 64$. 72

3.10 Optimal stacking sequence and thickness obtained using STLO for studies in Table 3.9. 73

4.1 Lamination parameter bounds for linear scaling maps. 80

4.2 Optimal results for stacking sequence retrieval optimization in step 2. 86

5.1 Optimization Formulation for Individual Objective Maximization. 107

5.2 Individual Objective Maximization Results for a 16 Ply Laminate. 107

5.3 Laminate Weight Minimization Results using MSADO Framework. 109

6.1 Material Properties of Bus Module. 114

6.2 Material Properties of Solar Array. 116

6.3 Properties of electronic boxes. 117

6.4 Optical properties of different material surfaces [9]. 123

6.5 Panel properties for baseline design. 124

6.6 Mass properties for baseline design of spacecraft. 125

6.7 Modes with maximum mass participation in each degree of freedom. 128

6.8 RMS acceleration in Gs at different mount locations. 131

6.9 Spacecraft optimization constraints. 137

6.10 Constraints that are at or near the limit from study 1. 140

6.11 Optimal face sheet stacking sequences. 141

6.12 Panel properties from optimization using lamination parameters (step 1). . . 153

6.13 Stacking sequence retrieval results for different orientation and ply thickness resolutions. 154

6.14 Actual optimal spacecraft panel properties corresponding to studies in Table 6.13. 155

Chapter 1

Introduction

1.1 Overview of Model-Based Space System Design

The desire for space exploration fueled by scientific, commercial, and government ambitions has led to the development of new technologies for spacecraft design. It has facilitated us to plan and execute previously intractable space missions effectively. The planning and design of these missions through traditional methods are done over large time frames. But, with an ever-increasing rate of research being conducted in this field, there is a continuous and rapid evolution in the design process of such missions. Thus, today's methods may be inefficient for tomorrow's planning. Also, since the time required for overall satellite development is high, the advent of new capabilities amidst the design phase requires reworking on the underlying design concepts. It has an impact on the system workflow that can incur unnecessary resource expenditure, communication mismatch between different domains, and increased scope for errors. To mitigate this, a model-based architecture must be established that can leverage existing and emerging technological capabilities to plan missions and develop state-of-the-art space systems rapidly.

Large scale system design team comprises entities from multiple domains that work in conjunction to build the final product. These domains can be primarily classified into management and engineering sectors. At a high level, the stakeholder's project requirements are classified into these two sectors. Based on these requirements, the management assigns

a budget, forms a schedule, evaluates risks, and estimates product value, whereas the engineering specialists work on the physical implementation of scientific and mathematical theories, modern manufacturing techniques, meticulous planning, and creative designs. In the initial planning phase, it is crucial to quickly narrow down a preliminary concept of the end product that roughly meets both management and engineering requirements, albeit not to everyone's great satisfaction. This accelerates product development in subsequent phases and aids in making key decisions. The initial concept is, in many cases, based on past experience, available mission data, and resources, but the modeling process can benefit to a great extent from the capability to access and implement ideas from externally available sources such as public and private firms, academic institutions, national laboratories, and literature. With the concept in hand, the high-level requirements must be hierarchically categorized for every subdomain/subsystem, and relationships between each category must be established to meet objectives efficiently.

Space systems are complex engineered systems with several levels of hierarchy. They involve interactions between multiple subsystems and individuals. Current systems engineering practices seldom capture these interactions. To facilitate rapid system development, system design preferences and individual decisions at different levels must be coherent. Model-Based Systems Engineering (MBSE) framework with the integration of Multidisciplinary Design Optimization (MDO) can capture all possible interactions between subsystems and ensure consistency in design decisions at each level. It can smooth the process from project definition to execution by minimizing rework.

Spacecraft subsystems are decomposed into components that can be designed, analyzed, and validated using different models, as shown in Fig 1.1. They are based on physics, mathematics, behaviors, or architecture. These models can be implemented for analysis and simulation, test and verification, communication, development of production codes, or

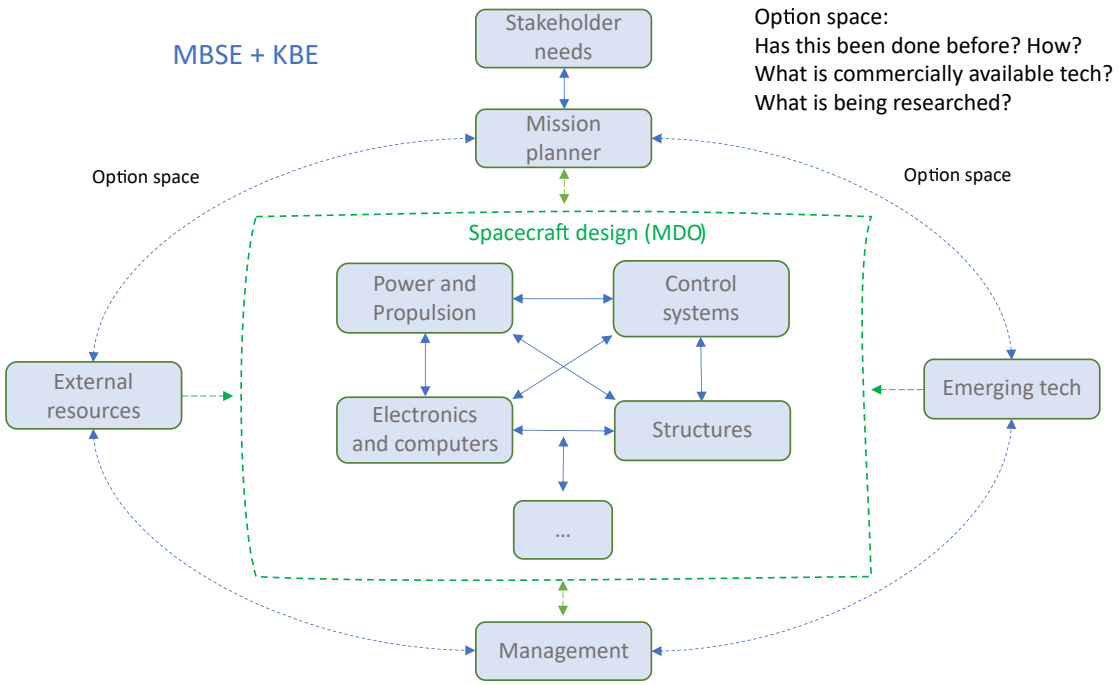

Figure 1.1: Space System Design Architecture

to introduce uncertainties. The MBSE methodology connects different models by forming a process for performing tasks, defining methods for each task, and using tools to enhance their efficiency in each environment. According to Estefan [2], the process defines "What" is to be done, the method defines "How" for each task, and the tool enhances "What" and "How" depending on the environment. In a model-driven system design, each task can be split into multiple sub-tasks and governed by sub-processes. It handles component-level designs and validates them with corresponding requirements, as shown in Fig 1.2. The methods can be based on a performance-driven engineering approach or a value-based engineering approach. The tools developed for modeling MBSE architecture use Object Management Group's Unified Modeling Language (UML) [10] and System Modeling Language (OMG SysML) [11].

Among the leading MBSE methodologies includes the IBM Telelogic Harmony-SE [1]. It uses a service request-driven modeling approach with SysML artifacts. The system structure

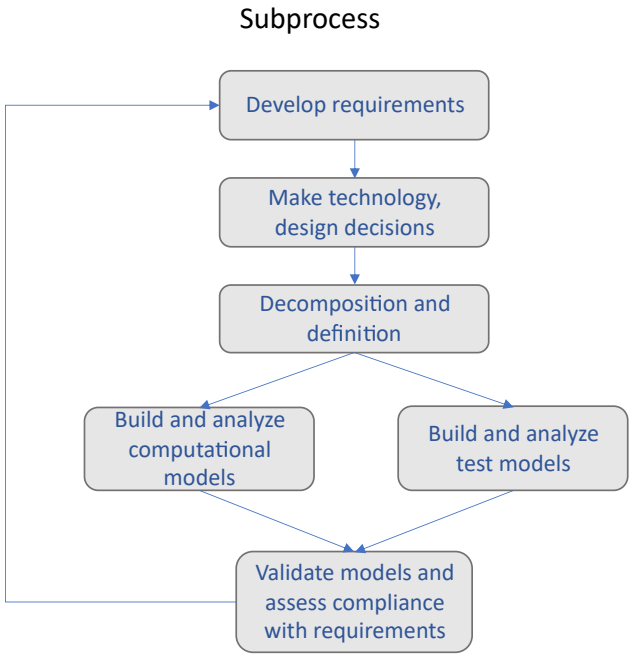

Figure 1.2: Design Subprocess Flowchart

is described by means of structure diagrams using block elements as shown in Fig 1.3a. Communication between two blocks is called a service request. The task flow in the Harmony-SE process includes three primary elements, namely requirements analysis, system functional analysis, and architectural design. As the name depicts, requirements analysis is used to analyze and classify requirements at different system levels. Based on it, the system use cases are defined for functional analysis and to determine a working concept. The subsystem architectures are then designed to develop the required product.

Another more general systems engineering method is the INCOSE Object-Oriented Systems Engineering Method or OOSEM [12, 13]. It uses a top-down model-based approach to support the specification, analysis, design, and verification of systems. By leveraging object-oriented concepts, it is possible to integrate them with object-oriented software, hardware, or other engineering methods. It also supports system-level reuse and design evolution which is one of the objectives of building a space mission design framework. OOSEM offers integrated

product development which is essential to improve communication. As seen from Fig 1.3b, it can analyze stakeholder needs, define system requirements, define logical architecture, combine candidate-allocated architectures, optimize and evaluate alternatives and validate and verify the system. The OOSEM model analyzes the current organization to determine its capabilities and derives mission requirements from the stakeholder. The mission requirements are specified in terms of mission objectives, effectiveness measures, and use cases. The scenarios for each use case are used to derive system functionality, interface, data, and performance requirements. The model is capable of utilizing risk-based requirement variation. A key aspect of OOSEM is that it provides guidelines for system decomposition based on different criteria. Other MBSE methodologies include IBM Rational Unified Process for Systems Engineering [14], Vitech Model-Based System Engineering (MBSE) Methodology [15] and Dori Object-Process Methodology [16].

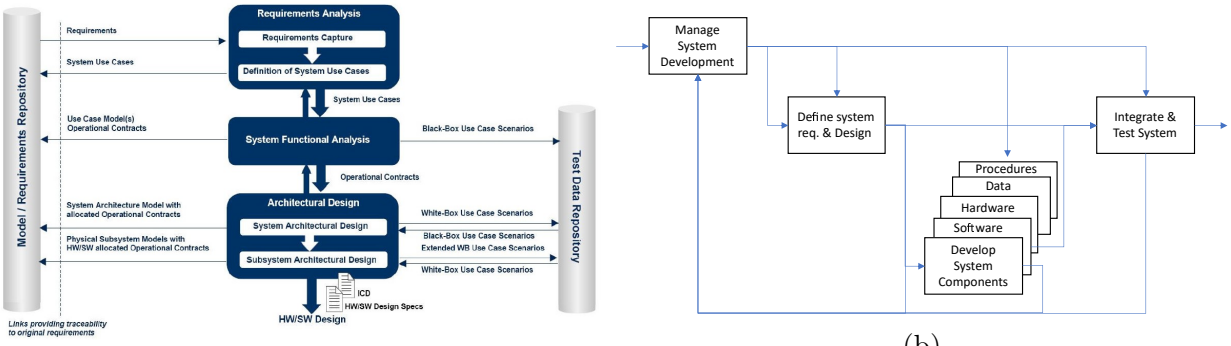

(a) (b)

Figure 1.3: Leading MBSE Methodologies. (a) Harmony-SE process elements [1], (b) OOSEM System Development Process [2].

Since, in any system design, optimization is of utmost importance, a significant effort has been made to develop tools by incorporating MBSE architectures at subsystem levels. Based on characteristics and integration capability, there are several commercial and open-source software that is used widely in academia and industries. A few commercial software for structural analysis includes Siemens NX, ABAQUS, LS-Dyna, and Ansys. This software can

be integrated into other commercial codes, such as HEEDS and Isight, or in open source codes, such as openMDAO, to build an efficient MDO framework for structural system design.

1.2 Design Structure Matrix Representation for MDO

The primary step in design optimization is to develop a structure that represents the underlying system's multiple elements and the data flow between these elements. Large-scale systems involve many disciplines, and a good information processing method is required to master the design and develop more complex techniques for solving engineering problems such as space system design. A system architecture is the structure of a system embodied in its elements, their relationships to each other, and the principles guiding its design and development. The architecture for solving an MDO problem is often overwhelmed with the flow of information, while the information processing capabilities to minimize errors are limited. A technique to overcome these barriers in developing efficient models for solving MDO problems is to use a design structure matrix (DSM) [3].

DSM is a network modeling technique that is highly flexible with applications in engineering management and development. It is used to represent the elements comprising a system and the interactions between the individual elements. DSM uses a square matrix to represent the system architecture, mapping the interactions among the set of N system elements. DSM provides a highly compact, easily scalable, and intuitively readable representation of system architecture. The cells in DSM represent the sources and destinations of the input and output interactions, identified by marks or numbers. These interactions can also be a flow of information between the elements. If one looks at the input in rows convention, examining any row in the matrix reveals all the inputs to the element in that row (which can be outputs

of other elements). Looking down at any column of the matrix shows all the outputs from the element in that column (which become inputs to other elements).

The data flow between different components can be attributed to the number of interactions, impact, or strength of each interaction. This can be represented by using numerical values, symbols, or color shades. DSM models can also be rearranged using analytical methods like clustering and sequencing. There are different types of system architecture used to represent a product, organization, process, or multi-domain system. The DSM highlights relationship patterns of particular interest to a system designer while providing a view that can support globally optimal decision-making and help orient those focused on particular elements. DSM analysis can also illuminate indirect links, change propagation, process iterations, convergence, modularity, and other important patterns and effect. An example of an aircraft design problem represented using DSM is shown in Fig 1.4.

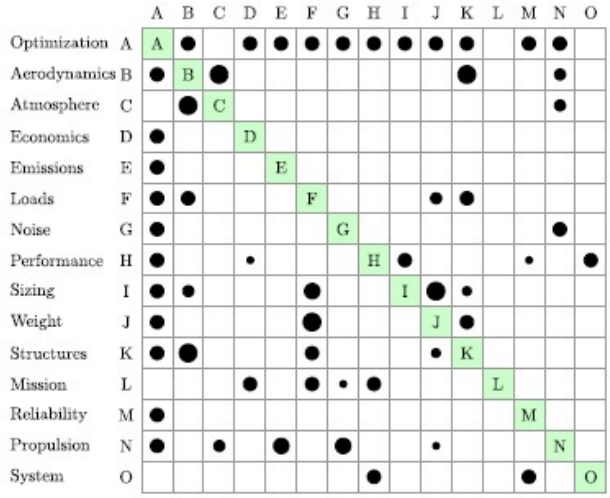

Figure 1.4: Example Design Structure Matrix for Aircraft Design Problem [3].

Numerous architectures exist for solutions to multidisciplinary design optimization problems. These architectures lack a standard way of describing the structure. A standard visual representation of these architectures can facilitate the implementation of solutions to MDO

problems. The extended design structure matrix (xDSM) by Lambe and Martins [4] extends the standard DSM to simultaneously show data dependency and process flow visualized in a single diagram. In the xDSM, a thick gray line represents data connections, while a thin black line represents process connections. Fig 1.5 shows the xDSM example for Multidisciplinary Feasible (MDF) architecture in which all the disciplines are coupled together, and multidisciplinary design analysis (MDA) is performed to compute the full set of state variables for a given choice of design variables. Mieloszyk et al. [17] presented the general idea of the optimization framework shown below according to the convention presented in work by Martins and Lambe [18]. The xDSM representation is used in several MDO studies.

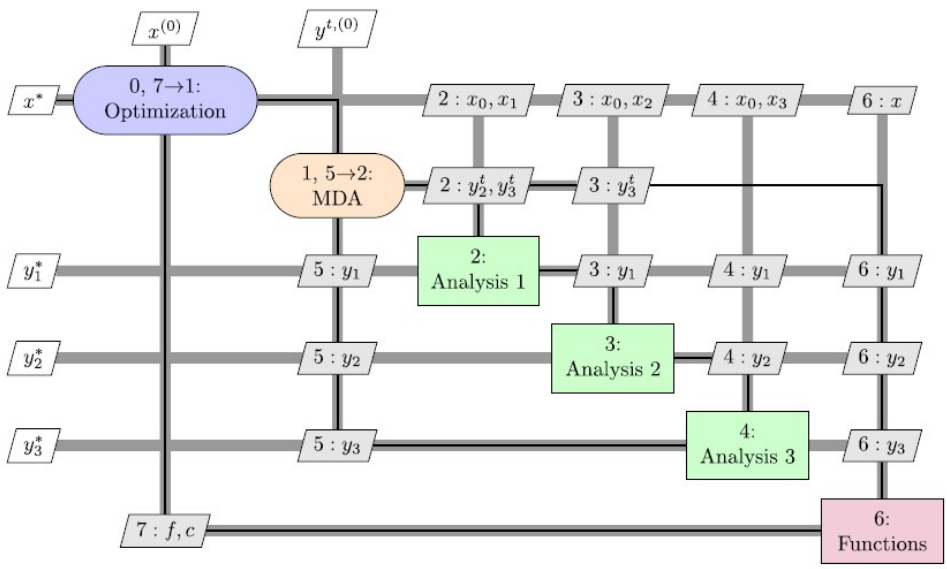

Figure 1.5: Example of an Extended Design Structure Matrix [4].

1.3 Overview of MDO in Aerospace Applications

Among recent studies, Benaouali and Kachel [19] developed an MDO framework by integrating commercial software such as Siemens NX, Ansys Fluent, ICEM and Nastran. They maximized the range of A320 while maintaining lift coefficient and structural safety. In the

forgoing study, a surrogate-based optimization strategy is adopted to reduce computational costs.

An MDO framework [5] for a low-speed composite flying-wing aircraft design is developed as shown in Fig 1.6. Three modules are developed within this framework, namely, the modeling module, the analysis module, and the optimization module. The modeling module includes geometry modeling, finite element modeling, and aeroelastic model construction. The wing outer mold line, internal structural layout of spars, and ribs locations are both parameterized in geometry modeling. Aerodynamic modeling for wing with multiple straight surfaces and conformal control surfaces are also developed. The analysis module has capabilities in structural analysis, aeroelastic analysis, and aerodynamic analysis. NASTRAN solver is used for structural and aeroelastic analyses. Virginia Tech in-house codes are used in estimation for drag and panel-level design analysis. In the optimization module, bilevel programming optimization is used to account for different types of design shape and sizing design variables. A parallel particle swarm optimization and gradient-based optimization are, respectively, used for shape and sizing optimization in the upper- and lower-level optimization problems.

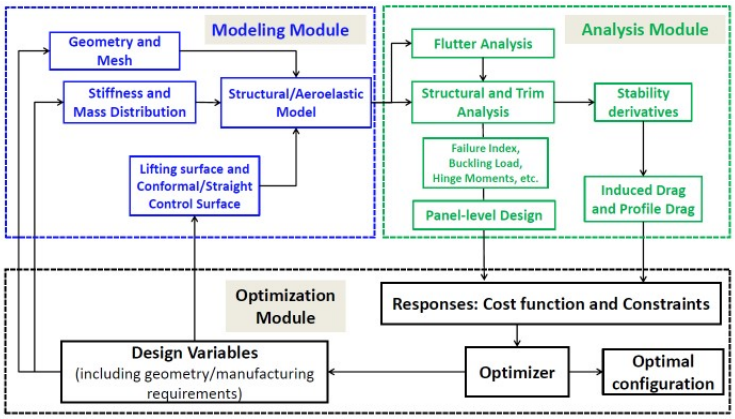

Figure 1.6: Computational Design Environment for Composite Aircraft Wing Design [5]

An MDO framework for supersonic aircraft configurations is demonstrated for a novel aircraft design by Love and Kapania [6]. They performed structural optimization of aircraft fuselage

and wing. The aircraft model used for the study is built using the VT-CST PSG program [20], which is tightly integrated with the MDO software. The MDO framework design structure matrix is shown in Fig 1.7.

	1	2	3	4	5	6	7	8	9	10	11	12	15
1	1. Input Design	Input File				Drag Polar, Engine TSFC							
2		2. VT-CST	NASTRAN Element Properties from Design Variables		NASTRAN Input Deck for Static Aeroelasticity		NASTRAN Input Deck for Static Aeroelasticity						
3			3. Sizing Model Preparation	Mapping between full set and linked set design variables									
4				4. Design Variable Demapping from Linked to Full Set	NASTRAN Full Set Design Variable Element Properties		NASTRAN Full Set Design Variable Element Properties						
5					5. Structural Weight Calculation	Structural Weight							
6						6. Fuel for Range Estimate	Fuel Weight						
7							7. Static Aeroelastic Analysis	NASTRAN .f06 with Weight and Trim Variables	Element Stresses	Forces due to aerodynamic loading			
8								8. Static Aeroelasticity Results Processor					Weight, Trim Variable Constraints
9									9. Stress Constraint Calculation				Stress Constraints
10										10. Buckling Model Generation	NASTRAN Input Deck for Global Buckling Analysis		
11											11. Buckling Analysis (NASTRAN)	NASTRAN .f06 with Buckling Eigenvalues	
12												12. Buckling Constraints Calculation	Buckling Constraints
15				NASTRAN Linked Design Variable Element Properties									13. Optimization

Figure 1.7: MDO Framework for Supersonic Aircraft Optimization [6].

A framework is established by Gur [21] for Multidisciplinary Design Optimization of a Truss-Braced-Wing (TBW) aircraft, including different modules such as structural analysis, aerodynamic analysis, and performance module. The Subsonic Ultra Green Aircraft Research (SUGAR) TBW aircraft concept is a Boeing-developed N+3 aircraft configuration in association with NASA. High aspect ratio wings provide greater aerodynamic efficiency but with a reduction in structural stability. To overcome this, truss-like support is provided to the conventional wing configuration. The truss members carry partial load axially and can change the effective bending and torsional stiffness of the wing.

Changes in the dynamic properties of an aircraft can influence the project and lead to redesign. The classical approach is based on dynamic stability analyses at the end of the design process. Thus, the inclusion of dynamic modeling within the design process is useful for optimizing the designs of vehicles. The work done by Gupta, Sanmugadas, Kapania, and Schmidt [22, 23] incorporates modeling the flight dynamics of a flexible aircraft into the

MDO framework. The methodology is based on the mean-axis formulation of the equations of motion, and the embedded aeroelastic model is based on the use of non-dimensional stability derivatives, as used in modeling rigid vehicles.

A collaborative optimization architecture for spacecraft system design with its flexibility to handle mixed-discrete nonlinear problems is demonstrated by Budianto [24]. Jilla and Miller [25] applied multidisciplinary techniques to distributed satellite systems. Hwang and Lee [26] demonstrated a large-scale multidisciplinary optimization methodology for small satellites that accounted for orbit and attitude dynamics, cell illumination, solar power, energy storage and communication, and temperature effects in the design. Wu et al. [27] used high-fidelity finite element models in the collaborative optimization architecture and enhanced the optimization process with sensitive information. As the goal of these and other similar extensive optimization studies is to design a complete system, several approximations are made to structural and component models to simplify the process.

1.4 The Role of MDO in Spacecraft Structural Design

The primary structure of a satellite must withstand different environmental loading conditions arising from its transportation to operation. It is acted upon by dynamic loads induced due to launch vehicle engine thrust, inertia loads due to its acceleration, sound pressure, wind gusts, and stage separations. In operation, the satellite is subjected to dynamic loads resulting from maneuvers and attitude corrections, whereas thermal cycles in space induce significant thermo-mechanical effects on its components. With a goal to minimize the payload weight and increase rigidity, trusses are the primary elements of choice. They are used to connect the bus module to the mission module and also to support solar arrays and antennas. Panels used on buses and solar arrays are subjected to large thermal

gradients that occur during the day and night cycles or at the time of eclipses. Sudden temperature changes induce micro-vibrations and quasi-static motions with large amplitudes as well as flutter. This was studied for bending modes by Thornton and Foster [28, 29] for a flexible solar array where they demonstrated analytical calculations to coupled thermal-structural systems and established conditions for thermal flutter as a measure of stability. Later, Chung and Thornton [30] and Murozono and Thornton [31] demonstrated a torsional buckling analysis for the same. Based on the above work, Xue et al. [32] developed a finite element scheme coupling thermal bending and torsional vibration effects for large space structures with thin-walled beam elements.

These spacecraft undergo significant rigid-body and deformable-body movements and, thus, have to be designed by considering large deformations of multibody systems. Many researchers over the decades have studied flexible multibody dynamics. Multiple issues and formulations are covered in [33, 34, 35, 36, 37, 38, 39, 40, 41] that use model-based analyses for such problems. A comprehensive review of techniques used for the same is given by Shabana [42]. Another aspect of spacecraft design is for the structure to maintain the desired shape with good accuracy under disturbances and instabilities. Different passive and active control techniques suppress dynamic effects due to maneuvering, attitude correction, and thermal effects. Among recent efforts, Yun [43] presented a two-stage vibration suppression model that uses a piezoelectric-based Stewart platform for high-frequency vibrations and fast steering mirror for low-frequency vibrations.

In the spacecraft design sector, control aspects have been considered at the early stages of the design process since the introduction of digital “fly-by-wire” control systems by NASA in the 1970s. The system allows for designs with improved maneuverability and performance by allowing relaxed stability requirements at the design phase. Deployable structures used in a spacecraft are generally highly flexible, leading to a coupling between rigid-body and flexible

dynamic modes [44]. This leads to challenges in the control design, needed for purposes like attitude and vibration control. Ignoring this aspect at earlier stages of structural design and placement of components may render the design uncontrollable. Structures with highly non-linear dynamics also require a suitable, accurate, high-order dynamic model, the absence of which may adversely affect the robustness of controllers designed at a later stage. Many times it is necessary to control only a part of the structure (such as the shape of the deployable structures), requiring tolerances as small as 1 mm [45], possibly even lesser for more recent applications. On the other hand, the limited payload and space availability in most space structures requires careful placement of actuators and sensors such that the control authority and quality of data collection remain unaffected.

The primary loads that drive the design of spacecraft structures can be classified into mechanical, acoustic, and thermal disciplines. The agglomeration of these loading environments and other mission requirements makes the structural optimization of spacecraft a multidisciplinary problem in itself. Optimization of intricate spacecraft models rests on determining optimal sizing parameters and material properties for underlying structural components that are based on a combination of springs, beams, and shells. The nature of design variables can be continuous or discrete to adhere to manufacturing capabilities. The structural response functions are derived from stresses, deformations, natural frequencies, and stability parameters. Thus, the problem is composed of a large design space with both continuous and discrete elements. Moreover, the multi-modal nature of constraints requires the use of global optimization algorithms such as Genetic Algorithms (GA), Particle Swarm Optimizer (PSO), Simulated Annealing, etc. These algorithms are implemented using sophisticated optimization techniques in the literature to not only find optimal design values but also to minimize the overall computational costs incurred with analyzing large-scale finite element models. From the perspective of academic research, these techniques are proven to give

optimal results with very high efficiency. But, in an industrial design environment, the design tools used must be robust and readily available, i.e., the tools must work effectively for multiple design problems. Thus, in this research, a multidisciplinary structural analysis and design optimization framework (MSADO) is developed purely using commercially available software and open-source tools, which can be implemented in any organization with ease and can facilitate rapid MSADO studies of spacecraft structures.

1.5 Use of Mixed Integer Programming for Composite Structure Optimization

Panels used in spacecraft's primary structures are made from composite materials to withstand quasi-static and fatigue loads. Optimization of composite laminates is a non-convex optimization problem that involves finding values of fiber orientation and thickness of multiple plies. The goal is to minimize the total weight of the laminate by satisfying various stability and strength constraints. These constraints can be linear or non-linear functions of lamination parameters which themselves are non-linear functions of design parameters. Over the last two decades, many studies have aimed to develop efficient optimization algorithms that can take into account such constraints and the discrete nature of design variables. Evolutionary algorithms have been widely used to find a globally optimal design for composite laminate configuration. Le Riche and Haftka [46] used a genetic algorithm (GA) in laminate optimization and showed that its efficiency in obtaining a good quality solution increases with an increase in the number of design variables but decreases with an increase in the number of nonlinear constraints. In that study, to increase the number of design variables, the total number of plies is increased while keeping the number of available ply orientations to be the same. An improved version with a combination of fixed and variable penalty

functions was explored in [47]. The particle swarm algorithm (PSO) used in the stacking sequence optimization for maximum fundamental frequency by Bargh and Sadr [48] was more efficient than the GA. Since multiple combinations of fiber orientations and ply thicknesses can give the same values of lamination parameters [49], most optimization algorithms struggle to obtain a converged solution when the design space is large.

Other studies developed sophisticated PSO algorithms such as vector evaluated particle swarm (VEPSO) [50] and quantum values particle swarm QPSO [51] for multi-objective requirements. A discrete PSO algorithm is presented by Chang et al. [52]. Simulated annealing is another reliable technique used in the literature to optimize composite laminates [53, 54, 55]. These studies show standard or modified meta-heuristic approaches, which are best suited for solving problems with continuous design space. Generally, in these formulations, continuous variables are rounded to the nearest integer to get discrete values of design variables. However, because of the stochastic characteristics of such meta-heuristics, they have difficulty converging to a global optimum or near-optimal solution in a reasonable time. The parameters governing these algorithms, such as the population size, crossover and mutation probability in GA or swarm size and particle velocity scaling in PSO, are problem dependent and need adjustment over multiple runs. Usually, these methods are coupled with non-heuristic optimization algorithms, such as gradient-based algorithms, to improve convergence efficiency.

Many studies have demonstrated the advantages of using multi-level formulations that use different optimization algorithms at different levels. The key concept in multi-level optimization is to decompose the problem into multiple sub-optimization problems based on convexity, the nature of design variables, and the types of constraints. These sub-optimization problems are solved in a nested or sequential manner using appropriate algorithms to reduce the complexity of the main problem and thus reduce the computational cost of optimiza-

tion. A bi-level decomposition technique was demonstrated by Schmit and Mehrinfar [56]. In this formulation, the upper level is used to minimize the structure weight subjected to strength and buckling constraints, whereas the lower level is used to optimize the geometry of composite panels. A two-level wing-box optimization is presented by Liu [57], where the problem is decomposed into wing and panel levels. The stacking sequence of each panel is optimized for buckling load at the panel level using a genetic algorithm, while the ply thickness is optimized at the wing level using GENESIS software.

A two-level optimization scheme by dividing the size and shape variables is shown in [58, 59, 60]. In these studies, the variables representing the geometry or shape of the structure are optimized first by fixing the sizing design variables, such as panel thickness and stiffener cross sections. The newly obtained shape variables are then fixed, and the design is optimized for sizing variables. This is repeated to minimize panel weight. Zhao and Kapania [61] demonstrated a bi-level approach to minimize composite laminate weight by using PSO in the upper level and a gradient-based optimizer (GBO) in the lower level. In the preceding study, the GBO is used to optimize design variables such as ply thicknesses which are assumed to be continuous, and the PSO is used to get the optimal ply orientations with discrete design space subjected to buckling and material failure constraints. The formulation significantly reduces the computation cost in comparison to the standard PSO or GA, but it is noticed that the PSO still reduces the algorithm's efficiency when there are a large number of plies considered for the composite laminates.

An alternative to tackle this concern is using mixed integer programs (MIPs) where discrete design variables such as ply thickness and orientations can be represented in terms of binary decision variables in linear or quadratic program formulations. A few decades ago, MIP in optimizing composite laminates was deemed intractable due to large computational expenses and the inability to handle constraint nonlinearities effectively. However, advancements

in computer technology and the development of advanced (branch-and-cut) algorithms for solving MIPs [62] have made it worthwhile to reevaluate the option.

These exact algorithms implicitly enumerate the solution space by generating a binary tree where at each node, the linear/continuous programming relaxation of another MIP, defined over a subset of the original solution space, is solved. As a result, these algorithms have higher chances of quickly arriving at a global optimum. Haftka et al. [63] used mixed integer linear programming (MILP) to optimize a composite panel for determining the most appropriate laminate stacking sequence. In their work, a MILP solver is used to maximize the buckling load and minimize the panel weight by varying the number of plies that have a fixed thickness value. Minimizing the panel weight subjected to buckling loads using decision variables for distinct ply thicknesses is a complex problem to solve using MIP. This is due to the cubic nature of lamination parameters with respect to thickness design variables. This problem is the one being solved in this paper.

A large-scale truss design optimization was demonstrated by Shahabsafa et al. [64], which uses mixed integer neighborhood search. In this method, the NP-hard subproblems are only solved to get an improved solution, and the next subproblem is defined in the neighborhood of this solution. A bi-level integer programming technique has been used by Zein [65] to optimize blended composite structures. The efficiency of MIP or Mixed Integer Non-linear Programs (MINLP) in solving linear or quadratic problems is higher compared to meta-heuristic solvers. But in the case of minimum weight optimization of a structure subjected to material failure and buckling constraints, there is a coupling between binary variables for ply orientations and thickness leading to higher order terms. Therefore, the problem must be decomposed into separate subproblems, each of which can be optimized using MIP or a combination of GBO and MIP.

For ease of manufacturing, composite laminates are designed with uniform thickness across all

plies. This approach has limitations on weight minimization when ply level failure constraints are involved, as even if only a single ply fails, the thickness of all plies must be increased. A design approach with non-uniform ply thickness can further help with weight savings. The use of non-uniform ply thicknesses, however, causes the lamination parameters to be cubic with respect to ply thickness design variables. Thus, the buckling constraints cannot be simplified using standard techniques and reformulation models given by Chang [66], and Adam and Forrester [67] must be used to linearize the lamination parameters with respect to thickness variables exactly. By implementing the reformulation models in this work, one can efficiently optimize a composite laminate configuration subjected to various non-linear design and manufacturing constraints.

A limitation of MIP solvers is that they require explicit expressions of constraints and the objective function. In practical application, semi-analytical approaches, such as the Ritz or Finite Element Method, are used to analyze complex structures. Herencia et al. [68] presented a two-step approach where the optimal lamination parameters are found in step 1 using GBO, and the stacking sequence is retrieved using GA. A similar approach is demonstrated by Peeters et al. [69] for a combined topology and lamination parameter optimization. In this method, the lamination parameters can be optimized relatively easily using any global or local optimization algorithm due to the smaller and continuous design space. The challenge lies in retrieving the stacking sequence for a predetermined number of plies that can match the optimum lamination parameter values as closely as possible. A beam search technique is used by Fedon et al. [70] to efficiently retrieve fiber orientations for a large number of plies. This dissertation uses a similar approach to optimize composite panels with finite element models. The panels are optimized first, assuming lamination parameters as continuous design variables. The stacking sequence and the optimal number of plies assuming fixed ply thickness are retrieved with the help of a MIP solver.

1.6 Research Overview

The research attempts to improve composite structure design optimization performance with a focus on space vehicle structures by targeting two main objectives.

1. Reduce the number of design evaluations required for the optimization of composite structures. The goal is to improve the efficiency and robustness of composite panel optimization with discrete variables.

2. Improve design evaluation performance by developing an efficient MDO framework for the multidisciplinary design of spacecraft structures.

Chapters II to IV demonstrate composite lamination parameter reformulations in terms of binary design variables. It presents the optimization of composite panels with MIP and compares the solver performance with that obtained from PSO and GA. The formulations are extended to solve hybrid laminate optimization problems with non-uniform ply thicknesses using reformulation linearization techniques. Further, optimization techniques are developed to implement the developed lamination parameter formulations to use with finite element models.

In Chapter II, the lamination parameters governing the extensional and bending stiffnesses of composite panels are formulated in terms of binary variables. Three different formulations are presented for optimizing rectangular composite laminates under bi-axial compressive loads subjected to buckling and material failure constraints. The first formulation optimizes ply fiber orientations and maximizes the buckling load for a given set of ply thicknesses. This formulation consists of buckling constraints where the lamination parameter variations are linear with respect to fiber orientation decision variables. It is generalized to work with any possible orientation values chosen from a finite set. The second formulation presents an

approach to minimize weight by minimizing the number of plies for a fixed ply thickness. A two-level approach is chosen to separate stacking sequence and thickness design variables to handle non-linear constraints where the lamination parameters are cubic and higher order. A sequential two-level methodology is adopted in the third formulation, where the stacking sequence and the ply thicknesses are optimized in separate loops in every iteration. Instead of varying the number of plies, the ply thicknesses are optimized along with the stacking sequence for a fixed number of plies.

Chapter III extends the lamination parameter formulation in Chapter II to solve optimization problems with distinct ply thicknesses and materials. A combination of different thicknesses for different plies can further help with weight savings, whereas using different materials for different plies can aid in reducing materials costs. The use of distinct ply thicknesses, however, causes the lamination parameters to be cubic with respect to ply thickness design variables. Thus, the buckling constraints cannot be simplified using standard techniques and reformulation models given by Chang [66], and Adam and Forrester [67] must be used to linearize the lamination parameters with respect to thickness variables exactly. By implementing the linearized reformulation models in this work, one can efficiently optimize a composite laminate configuration subjected to various non-linear design and manufacturing constraints.

Chapter IV further extends the techniques developed in Chapters II and III to incorporate FEM to optimize complex composite structures. The stiffness matching approach from the literature is modified to retrieve stacking sequences from lamination parameters using MIP instead of heuristic solvers.

In Chapters V and VI, a multidisciplinary structural analysis and design optimization (MSADO) framework is developed by integrating commercial software and open-source Python libraries. The framework includes modules for linear static, modal analyses, sine vi-

bration, random vibration, shock vibration, vibroacoustics, orbital heat transfer, and thermo-elastic analysis of spacecraft. These modules are integrated efficiently using HEEDS [71] and pyNastran [72]. Simplified finite element models are built for spacecraft structural, acoustic, and thermal analysis. A novel method of performing shock response analysis using shock response spectrum synthesis is proposed. Spacecraft structure with composite sandwich panels is optimized for minimum mass for various launch vehicle and in-orbit loads. The lamination parameters and MIP-based techniques developed in Chapter IV are extended for the multidisciplinary optimization of spacecraft primary structures by combining them with the MSADO framework. The thermal conductivities of the equivalent shell model are derived as functions of lamination parameters to use in thermal-structural optimization. The efficiency of this approach is compared with that achieved by the direct method. The summary of the present research and possible future avenues are described in Chapter VII.

Chapter 2

Optimization of Composite Laminates with Uniform ply Thickness

The response of any orthotropic or anisotropic composite laminate is governed by six components each for extensional stiffness A_{ij}, bending stiffnesses D_{ij} and bending-extension coupling terms B_{ij} $(i, j = 1, 2, 6)$. Additionally, with transverse shear effects, the shear stiffnesses A_{44}, A_{45} and A_{55} must be included. The stiffnesses are linear functions of lamination parameters V and material invariants U [73]. The lamination parameters are trigonometric functions of ply fiber orientations. These functions can be linearized using decision variables. This chapter presents a step-by-step reformulation of lamination parameters using binary variables that helps to make the design space convex and enables the use of mixed integer programming solvers. The work presented in this chapter is published in [74].

Three techniques are demonstrated for optimizing rectangular composite laminates under bi-axial compressive loads subjected to buckling and material failure constraints. The first formulation is used to optimize ply fiber orientations and maximize the buckling load for a given set of ply thicknesses. This formulation consists of buckling constraints where the lamination parameter variations are linear with respect to fiber orientation decision variables. It is generalized to work with any possible orientation values chosen from a finite set. The second formulation presents an approach to minimize weight by minimizing the number of plies for a fixed ply thickness. To handle non-linear constraints where the lamination

parameters are cubic and higher order with respect to design variables, a two-level approach is chosen to separate stacking sequence and thickness design variables. A sequential two-level methodology is adopted in the third formulation, where the stacking sequence and the ply thicknesses are optimized in separate loops in every iteration. As opposed to varying the number of plies, the ply thicknesses are optimized along with the stacking sequence for a fixed number of plies. In the aforementioned optimization studies, uniform ply thickness is considered to simplify the nature of constraints used in the thickness optimization level.

2.1 Laminate Analysis

A symmetric composite laminate plate under study is subjected to static bi-axial compressive loads λN_{xx} and λN_{yy} in x and y directions, respectively, as shown in Fig. 2.1, where λ is a scaling parameter. The panel has a fixed number of plies N with orientations, $\theta_1, \theta_2, \cdots,$ and θ_N, and ply thicknesses, $t_1, t_2, \cdots,$ and t_N. The ply thicknesses are treated as fixed parameters in the optimization to maximize buckling load, whereas they are considered design variables when the objective is to minimize panel weight. The panel is assumed to have a fixed and uniform geometry and material properties. It is also assumed that the loads are constant over the edges on which they are defined.

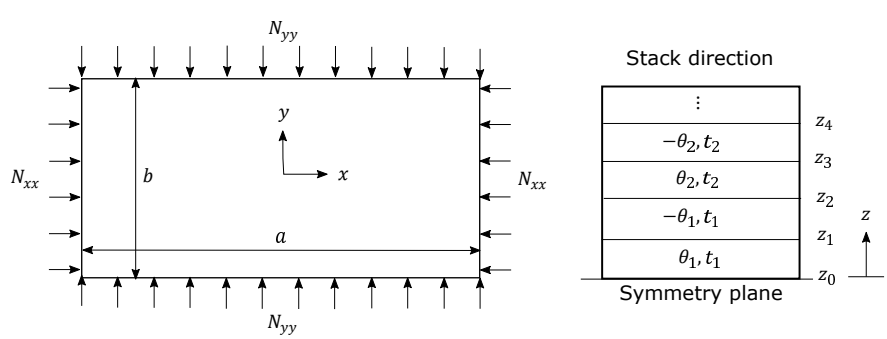

Figure 2.1: Rectangular composite panel ($a = 20$ in., $b = 5$ in.) subjected to bi-axial loading.

For a symmetric and balanced laminate, the axial and flexural stiffness coefficients are defined in terms of material invariants, U, and lamination parameters, V [73],

$$\begin{aligned}
A_{11} &= U_1V_{0A} + U_2V_{1A} + U_3V_{3A} & D_{11} &= U_1V_{0D} + U_2V_{1D} + U_3V_{3D} \\
A_{22} &= U_1V_{0A} - U_2V_{1A} + U_3V_{3A} & D_{22} &= U_1V_{0D} - U_2V_{1D} + U_3V_{3D} \\
A_{12} &= U_4V_{0A} - U_3V_{3A} & D_{12} &= U_4V_{0D} - U_3V_{3D} \\
A_{66} &= U_5V_{0A} - U_3V_{3A} & D_{66} &= U_5V_{0D} - U_3V_{3D}
\end{aligned} \tag{2.1}$$

where the material invariants $U_i, i \in \{1, \ldots, 5\}$ are given in terms of (known) local ply stiffnesses $Q_{jk}, j, k \in \{1, \ldots, 6\}$ as:

$$\begin{aligned}
U_1 &= \frac{1}{8}(3Q_{11} + 3Q_{22} + 2Q_{12} + 4Q_{66}) \\
U_2 &= \frac{1}{2}(Q_{11} - Q_{22}) \\
U_3 &= \frac{1}{8}(Q_{11} + Q_{22} - 2Q_{12} - 4Q_{66}) \\
U_4 &= \frac{1}{8}(Q_{11} + Q_{22} + 6Q_{12} - 4Q_{66}) \\
U_5 &= \frac{1}{8}(Q_{11} + Q_{22} - 2Q_{12} + 4Q_{66})
\end{aligned} \tag{2.2}$$

and V_0, V_1, and V_3 are dependent on ply orientations and thicknesses as follows:

$$\begin{aligned}
V_{0A} &= \int_{-h/2}^{h/2} dz & V_{0D} &= \int_{-h/2}^{h/2} z^2 dz \\
V_{1A} &= \int_{-h/2}^{h/2} \cos 2\theta dz & V_{1D} &= \int_{-h/2}^{h/2} z^2 \cos 2\theta dz \\
V_{3A} &= \int_{-h/2}^{h/2} \cos 4\theta dz & V_{3D} &= \int_{-h/2}^{h/2} z^2 \cos 4\theta dz
\end{aligned} \tag{2.3}$$

Here, h is the total thickness of the laminate, and z is the distance of a ply from the plane of symmetry. Writing the extensional and bending stiffnesses in terms of material invariants and lamination parameters helps in separating the terms that are dependent on design variables (ply fiber orientations and ply thicknesses). In turn, it helps us introduce binary decision variables comfortably in the lamination parameters expressions, as shown in the next section. Panel failure occurs if either the maximum load exceeds the critical buckling load or the local strains induced in any of the plies exceed the allowable limit. The buckling load factor λ_b for applied bi-axial compressive loads is given as in [75],

$$\lambda(m,n) = \pi^2 \frac{D_{11}(m/a)^4 + 2(D_{12} + 2D_{66})(m/a)^2(n/b)^2 + D_{22}(n/b)^4}{(m/a)^2 N_{xx} + (n/b)^2 N_{yy}} \tag{2.4}$$

where m and n are integer numbers that show the number of half waves of buckling mode shapes in x and y directions, respectively. The laminate instability occurs when a critical load scaling parameter, λ_{cr}, exceeds the minimum value of $\lambda_b(m,n)$ for all m and n. The material strength is characterized by using a maximum strain theory. The ply strains are a function of axial stiffnesses A_{11}, A_{22}, A_{12}, and A_{66}. For bi-axial loads and symmetric and balanced laminate, mid-plane shear strains, γ_{xy} go to zero under the action of normal strains. Thus, for a unit value of λ the longitudinal strain, ε_{xx}, and transverse strain, ε_{yy}, can be written as a function of A_{11}, A_{22}, and A_{12},

$$\begin{aligned} \varepsilon_{xx} &= \frac{N_{xx}A_{22} - N_{yy}A_{12}}{A_{11}A_{22} - A_{12}^2} \\ \varepsilon_{yy} &= \frac{N_{yy}A_{11} - N_{xx}A_{12}}{A_{11}A_{22} - A_{12}^2} \end{aligned} \tag{2.5}$$

In the material coordinate system, the ply strains can be obtained from Eqn 2.5 using coordinate framework transformation. Thus, for ply $k \in \{1, \ldots, N\}$, the longitudinal strain ε_1^k , transverse strain ε_2^k and shear strain ε_{12}^k are defined as in Eqn 2.6. The material fails

when the normal or shear strains in ply k are larger than the corresponding failure strains.

$$\begin{aligned} \varepsilon_1^k &= \cos^2\theta_k\varepsilon_{xx} + \sin^2\theta_k\varepsilon_{yy} \\ \varepsilon_2^k &= \sin^2\theta_k\varepsilon_{xx} + \cos^2\theta_k\varepsilon_{yy} \\ \varepsilon_{12}^k &= \sin 2\theta_k(\varepsilon_{yy} - \varepsilon_{xx}) \end{aligned} \tag{2.6}$$

2.2 Constraint Formulation using Binary Variables

Composite laminate failure may happen either due to instability or material failure. Even though most panel optimization studies [46, 50, 53, 54, 55] only use stability constraints as it is usually the dominant failure mode, in certain design configurations, the panels may fail due to material failure before the critical buckling load is reached. Thus both buckling and strain constraints are used to govern the failure in this study. Binary decision variables are used to choose ply orientation and thickness from a predefined set in an MINLP formulation where the buckling and strain constraints are defined in terms of the binary variables. To use a multi-level optimization technique, the formulation of constraints with respect to two classes of binary variables, namely, stacking sequence variables and ply thickness variables, is shown next.

2.2.1 Buckling Constraints Formulation for Stacking Sequence Optimization

The buckling load factor for the bi-axial load case is given in Eq. (2.4). Suppose a composite laminate is made up of N plies with symmetry (total plies = $2N$) where each ply can take a value from a given finite set of orientations $\Theta = \{\theta_1, \theta_2, \ldots, \theta_p\}$. For a single ply, with p available orientations to choose from, there are p binary variables associated with it. Thus,

for N plies, the total number of binary design variables for the fiber path orientations are Np. the vector $\mathbf{x}$ of binary design variables can be written as

$$\mathbf{x} = [x_{11}, x_{12} \cdots x_{1p}, x_{21}, x_{22} \cdots x_{2p} \cdots x_{kl} \cdots x_{N1}, x_{N2} \cdots x_{Np}]^T \tag{2.7}$$

$$\mathrm{X} = \begin{array}{c|c} & \overrightarrow{\text{Orientations}} \\ & \begin{array}{cccc} \theta_1 & \theta_2 & \dots & \theta_p \end{array} \\ \text{Ply} \downarrow \begin{array}{c} 1 \\ 2 \\ \vdots \\ k \\ \vdots \\ N \end{array} & \begin{pmatrix} x_{11} & x_{12} & \dots & x_{1p} \\ x_{21} & x_{22} & \dots & x_{2p} \\ & \vdots & & \\ x_{k1} & x_{k2} & \dots & x_{kp} \\ & \vdots & & \\ x_{N1} & x_{N2} & \dots & x_{Np} \end{pmatrix} \end{array} \tag{2.8}$$

where, x_{kl} is the binary variable associated with ply k and orientation $\theta_l \in \Theta$, i.e., $x_{kl} = 1$ if the ply k has orientation θ_l and 0 otherwise. Note that for each ply k, $\sum_{l=1}^{p} x_{kl} = 1$ ensures that only one orientation is assigned to the ply. For better visualization to the reader, the design variable vector is reshaped in the matrix form X as (2.8). As a result, the integral for V_{0D}, V_{1D} and V_{3D} from Eq. (2.3) can be expressed in terms of x_{kl} as

$$\begin{aligned} V_{0D} &= \frac{2}{3} \sum_{k=1}^{N} \left[(z_k^3 - z_{k-1}^3) \sum_{l=1}^{p} x_{kl} \right] \\ V_{1D} &= \frac{2}{3} \sum_{k=1}^{N} \left[(z_k^3 - z_{k-1}^3) \sum_{l=1}^{p} x_{kl} \cos 2\theta_l \right] \\ V_{3D} &= \frac{2}{3} \sum_{k=1}^{N} \left[(z_k^3 - z_{k-1}^3) \sum_{l=1}^{p} x_{kl} \cos 4\theta_l \right] \end{aligned} \tag{2.9}$$

where z_k is the thickness coordinate for the top surface of the $k-$th ply and z_{k-1} is the bottom surface thickness coordinate of the $k-$th ply. Note that since ply thickness is fixed, the buckling expressions in Eq. (2.9) are linear functions of $\mathbf{x}$. The above calculation can be simplified by separating the design variable and writing the lamination parameters and flexural stiffnesses in vector form i.e., using each term that is inside the summation as a vector element. The stiffnesses D_{11}, D_{22}, D_{12}, and D_{66} can be represented as

$$D_{11} = \mathbf{d}_{(\mathbf{11})}{}^T\mathbf{x}; \quad D_{22} = \mathbf{d}_{(\mathbf{22})}{}^T\mathbf{x}; \quad D_{12} = \mathbf{d}_{(\mathbf{12})}{}^T\mathbf{x}; \quad D_{66} = \mathbf{d}_{(\mathbf{66})}{}^T\mathbf{x} \tag{2.10}$$

where $\mathbf{d}_{(\mathbf{ij})}, i, j \in \{(1,1),(2,2),(1,2),(6,6)\}$, are vectors of size Np whose elements $d^k_{l(ij)}$ represent the flexural stiffness D_{ij} of ply k having an orientation θ_l. The task of the optimizer is to choose values from the above-defined vectors for flexural stiffnesses such that the summation of chosen values will lead to optimal flexural stiffnesses of the laminate.

2.2.2 Strain Constraint Formulation for Stacking Sequence Optimization

In symmetric laminates, strains are a function of extensional stiffness A_{ij}, which needs to be represented using binary variables $\mathbf{x}$. By using a similar approach as that used for obtaining Eq. (2.10), the extensional stiffness can be written as a function of binary design variables as:

$$A_{11} = \mathbf{a}_{(\mathbf{11})}{}^T\mathbf{x}; \quad A_{22} = \mathbf{a}_{(\mathbf{22})}{}^T\mathbf{x}; \quad A_{12} = \mathbf{a}_{(\mathbf{12})}{}^T\mathbf{x}. \tag{2.11}$$

The element $a^k_{l(ij)}$ of vector $\mathbf{a_{(ij)}}$ represent the axial stiffness A_{ij} of ply k having an orientation θ_l where $(i,j) \in \{(1,1),(2,2),(1,2)\}$. the global strains are written as in Eq. (2.5) as:

$$\begin{aligned} \varepsilon_{xx} &= \frac{[N_{xx}\mathbf{a_{(22)}}^T - N_{yy}\mathbf{a_{(12)}}^T]\mathbf{x}}{\mathbf{x}^T[\mathbf{a_{(11)}}\mathbf{a_{(22)}}^T - \mathbf{a_{(12)}}\mathbf{a_{(12)}}^T]\mathbf{x}} \\ \varepsilon_{yy} &= \frac{[N_{yy}\mathbf{a_{(11)}}^T - N_{xx}\mathbf{a_{(12)}}^T]\mathbf{x}}{\mathbf{x}^T[\mathbf{a_{(11)}}\mathbf{a_{(22)}}^T - \mathbf{a_{(12)}}\mathbf{a_{(12)}}^T]\mathbf{x}} \end{aligned} \tag{2.12}$$

To transform the strains from Eq. (2.12) into the material coordinate system, three column vectors are defined $\mathbf{c}$, $\mathbf{s}$ and $\mathbf{s_2}$ to represent the values for $\cos^2\theta$, $\sin^2\theta$ and $\sin 2\theta$, respectively; i.e., $\mathbf{c} = [\cos^2\theta_1, \cos^2\theta_2, \ldots, \cos^2\theta_p]$, $\mathbf{s} = [\sin^2\theta_1, \sin^2\theta_2, \ldots, \sin^2\theta_p]$ and $\mathbf{s_2} = [\sin 2\theta_1, \sin 2\theta_2, \ldots, \sin 2\theta_p]$. To get the strain in ply k, these vectors are used along with a transformation matrix H_k such that only design variables associated with ply k are multiplied with the respective p orientations. If $j_s = (k-1)p + 1$ is the starting index of the design variables associated with ply k, then the ending index $j_e = kp$. The transformation matrix H_k is a sparse matrix having dimensions $(Np \times p)$ with elements in rows and columns ranging from j_s to j_e forming an identity matrix. ply strains from Eq. (2.6) can be written as a function of stacking sequence binary variables as:

$$\begin{aligned} \varepsilon^k_1 &= \frac{\mathbf{x}^T\{H_k\mathbf{c}[N_{xx}\mathbf{a_{(22)}}^T - N_{yy}\mathbf{a_{(12)}}^T] + H_k\mathbf{s}[N_{yy}\mathbf{a_{(11)}}^T - N_{xx}\mathbf{a_{(12)}}^T]\}\mathbf{x}}{\mathbf{x}^T[\mathbf{a_{(11)}}\mathbf{a_{(22)}}^T - \mathbf{a_{(12)}}\mathbf{a_{(12)}}^T]\mathbf{x}} \\ \varepsilon^k_2 &= \frac{\mathbf{x}^T\{H_k\mathbf{s}[N_{xx}\mathbf{a_{(22)}}^T - N_{yy}\mathbf{a_{(12)}}^T] + H_k\mathbf{c}[N_{yy}\mathbf{a_{(11)}}^T - N_{xx}\mathbf{a_{(12)}}^T]\}\mathbf{x}}{\mathbf{x}^T[\mathbf{a_{(11)}}\mathbf{a_{(22)}}^T - \mathbf{a_{(12)}}\mathbf{a_{(12)}}^T]\mathbf{x}} \\ \varepsilon^k_{12} &= \frac{\mathbf{x}^T H_k\mathbf{s_2}\{N_{yy}\mathbf{a_{(11)}}^T + (N_{yy} - N_{xx})\mathbf{a_{(12)}}^T - N_{xx}\mathbf{a_{(22)}}^T\}\mathbf{x}}{\mathbf{x}^T[\mathbf{a_{(11)}}\mathbf{a_{(22)}}^T - \mathbf{a_{(12)}}\mathbf{a_{(12)}}^T]\mathbf{x}} \end{aligned} \tag{2.13}$$

Equations (2.13) have quadratic expressions in the form of $\mathbf{x}^T Q\mathbf{x}$, in both the numerator and the denominator. It can be equated with the allowable strain values and rearranged to get a quadratic expression with respect to design variables $\mathbf{x}$. This holds true if N_{xx} and N_{yy} are constant. If Eq. (2.13) is to be used in the buckling load maximization problem, the

variable for buckling load factor λ must be multiplied to the R.H.S. making it a cubic mixed integer programming problem. This problem can be avoided by including strain constraints only at the thickness optimization level.

2.2.3 Buckling Constraints Formulation for Ply Thickness Optimization

Using the buckling constraint in the minimum weight design requires the inclusion of thickness variables. This leads to a 4th order polynomial constraint that can be handled by efficient linearization of constraints and the use of multi-level optimization techniques. The order of the buckling constraint w.r.t design variables can be reduced by using two optimization levels. In one level, ply thicknesses are fixed, and the laminate is optimized for stacking sequence leading to linear and quadratic expressions of constraints w.r.t $\mathbf{x}$. The second level is used for finding optimal thickness values by fixing ply orientations resulting in a cubic expression. This is because the bending stiffness matrix, $\boldsymbol{D}$, is a cubic function of ply thickness (see Eqs. (2.1) and (2.3)). Let $\mathbf{y}$ be the vector of binary design variables associated with a finite set of thickness values $\mathrm{T} = \{t_1, t_2, \cdots, t_q\}$ such that

$$\mathbf{y} = [y_{11}, y_{12} \cdots y_{1q}, y_{21}, y_{22} \cdots y_{2q} \cdots y_{kl} \cdots y_{N1}, y_{N2} \cdots y_{Nq}]^T \tag{2.14}$$

where, y_{kl} is the binary variable associated with ply k and thickness $t_l \in \mathrm{T}$. The lamination parameters V_{0D}, V_{1D} and V_{3D} are cubic functions of ply thickness coordinates z_k. For a fixed ply orientation $\hat{\theta}_k \in \Theta$, Eq. (2.9) for a symmetric layup can be rewritten as:

$$
\begin{aligned}
V_{0D} &= \frac{2}{3}\sum_{k=1}^{N}(z_k^3 - z_{k-1}^3) = \frac{2}{3}z_N^3 \\
V_{1D} &= \frac{2}{3}\sum_{k=1}^{N}(z_k^3 - z_{k-1}^3)\cos 2\hat{\theta}_k \\
&= \frac{2}{3}\left[z_N^3\cos 2\hat{\theta}_N + z_{N-1}^3(\cos 2\hat{\theta}_{N-1} - \cos 2\hat{\theta}_N) + \cdots + z_1^3(\cos 2\hat{\theta}_1 - \cos 2\hat{\theta}_2)\right] \\
V_{3D} &= \frac{2}{3}\sum_{k=1}^{N}(z_k^3 - z_{k-1}^3)\cos 4\hat{\theta}_k \\
&= \frac{2}{3}\left[z_N^3\cos 4\hat{\theta}_N + z_{N-1}^3(\cos 4\hat{\theta}_{N-1} - \cos 4\hat{\theta}_N) + \cdots + z_1^3(\cos 4\hat{\theta}_1 - \cos 4\hat{\theta}_2)\right]
\end{aligned}
\tag{2.15}
$$

Special Case with all Plies having Same Thickness. Assuming that all plies have the same thickness, then the number of binary variables in $\mathbf{y}$ reduces from Nq to q. Specifically, $\mathbf{y} := [y_1, y_2, \ldots, y_q]^T \in \{0,1\}^q$ where $y_l = 1$ when all plies have thickness $t_l \in T$ and 0, otherwise. Let $\mathbf{t} := [t_1, t_2, \ldots, t_q]^T$. Then, the z-distance of each ply in terms of ply thicknesses are

$$
\begin{aligned}
z_0 &= 0 \\
z_k &= z_{k-1} + \sum_{l=1}^{q} t_l y_l = k\mathbf{t}^T\mathbf{y}, \quad \text{for } k = 1, \ldots, N, \\
\therefore z_k^3 &= k^3\left(\mathbf{t}^T\mathbf{y}\right)^3
\end{aligned}
\tag{2.16}
$$

It is important to note that $\sum_{l=1}^{q} y_l = 1$ because all the plies have the same thickness and they can have only one value from T. As a consequence, $\Pi_{l\in S} y_i = 0$ for all $S \subseteq \{1, \ldots, q\}$ where $|S| \geq 2$. This implies that any product of y variables with at least different indices is equal to 0. Therefore, $\left(\mathbf{t}^T\mathbf{y}\right)^3 = \sum_{l=1}^{q} t_l^3 y_l^3 = \sum_{l=1}^{q} t_l^3 y_l$. The last equality is because $y_l \in \{0,1\}$. This gives:

$$
z_k^3 = k^3\sum_{l=1}^{q} t_l^3 y_l = k^3\left(\mathbf{t}^{\circ 3}\right)^T\mathbf{y} \tag{2.17}
$$

where the notation '$\circ$' represents Hadamard or element-wise operation. In this special case, the cubic expression of z - distances in terms of ply thicknesses (2.17) is linear w.r.t $\mathbf{y}$. Thus, the lamination parameters in Eq. (2.15) become linearly dependent on ply thickness variables as

$$\begin{aligned} V_{0D} &= \frac{2}{3}\sum_{k=1}^{N}(z_k^3 - z_{k-1}^3) = \frac{2}{3}N^3\left(\mathbf{t}^{\circ 3}\right)^T\mathbf{y} \\ V_{1D} &= \frac{2}{3}\sum_{k=1}^{N}\left\{\left[k^3-(k-1)^3\right]\cos 2\hat{\theta}_k\right\}\left(\mathbf{t}^{\circ 3}\right)^T\mathbf{y} \\ V_{3D} &= \frac{2}{3}\sum_{k=1}^{N}\left\{\left[k^3-(k-1)^3\right]\cos 4\hat{\theta}_k\right\}\left(\mathbf{t}^{\circ 3}\right)^T\mathbf{y} \end{aligned} \tag{2.18}$$

This is similar to calculating flexural stiffnesses D_{ij} and buckling load factor λ for a given set of thicknesses and selecting the thickness that gives the optimal buckling load factor.

2.2.4 Strain Constraints Formulation for Ply Thickness Optimization

Strains in ply k with fixed ply orientations $\hat{\theta}_k$ and variable thickness can be written as

$$\begin{aligned} \varepsilon_1^k &= \frac{\{\cos^2\hat{\theta}_k[N_{xx}\mathbf{a_{(22)}}^T - N_{yy}\mathbf{a_{(12)}}^T] + \sin^2\hat{\theta}_k[N_{yy}\mathbf{a_{(11)}}^T - N_{xx}\mathbf{a_{(12)}}^T]\}\mathbf{y}}{\mathbf{y}^T[\mathbf{a_{(11)}}\mathbf{a_{(22)}}^T - \mathbf{a_{(12)}}\mathbf{a_{(12)}}^T]\mathbf{y}} \\ \varepsilon_2^k &= \frac{\{\sin^2\hat{\theta}_k[N_{xx}\mathbf{a_{(22)}}^T - N_{yy}\mathbf{a_{(12)}}^T] + \cos^2\hat{\theta}_k[N_{yy}\mathbf{a_{(11)}}^T - N_{xx}\mathbf{a_{(12)}}^T]\}\mathbf{y}}{\mathbf{y}^T[\mathbf{a_{(11)}}\mathbf{a_{(22)}}^T - \mathbf{a_{(12)}}\mathbf{a_{(12)}}^T]\mathbf{y}} \\ \varepsilon_{12}^k &= \frac{\sin 2\hat{\theta}_k\{N_{yy}\mathbf{a_{(11)}}^T + (N_{yy}-N_{xx})\mathbf{a_{(12)}}^T - N_{xx}\mathbf{a_{(22)}}^T\}\mathbf{y}}{\mathbf{y}^T[\mathbf{a_{(11)}}\mathbf{a_{(22)}}^T - \mathbf{a_{(12)}}\mathbf{a_{(12)}}^T]\mathbf{y}} \end{aligned} \tag{2.19}$$

Rearranging Eq. (2.19) will result in quadratic expressions in $\mathbf{y}$ in the form: $\mathbf{y}^TQ\mathbf{y} - B\mathbf{y} = 0$.

Special Case. For plies with uniform thickness, the strain expression can be linearized similar to the buckling expressions. By fixing the orientation values in vectors $\mathbf{c}$, $\mathbf{s}$, and $\mathbf{s2}$ and using

element-wise operations ($\circ$), the system of linear equations for $\varepsilon_{\mathbf{1}}, \varepsilon_{\mathbf{2}}$ and $\varepsilon_{\mathbf{12}}$ can be obtained.

$$\begin{aligned}
\varepsilon_{\mathbf{1}} &= \frac{\{\mathbf{c}[N_{xx}\mathbf{a}_{(\mathbf{22})}{}^T - N_{yy}\mathbf{a}_{(\mathbf{12})}{}^T] + \mathbf{s}[N_{yy}\mathbf{a}_{(\mathbf{11})}{}^T - N_{xx}\mathbf{a}_{(\mathbf{12})}{}^T]\}\mathbf{y}}{[\mathbf{a}_{(\mathbf{11})} \circ \mathbf{a}_{(\mathbf{22})} - \mathbf{a}_{(\mathbf{12})} \circ \mathbf{a}_{(\mathbf{12})}]^T\mathbf{y}} \\
\varepsilon_{\mathbf{2}} &= \frac{\{\mathbf{s}[N_{xx}\mathbf{a}_{(\mathbf{22})}{}^T - N_{yy}\mathbf{a}_{(\mathbf{12})}{}^T] + \mathbf{c}[N_{yy}\mathbf{a}_{(\mathbf{11})}{}^T - N_{xx}\mathbf{a}_{(\mathbf{12})}{}^T]\}\mathbf{y}}{[\mathbf{a}_{(\mathbf{11})} \circ \mathbf{a}_{(\mathbf{22})} - \mathbf{a}_{(\mathbf{12})} \circ \mathbf{a}_{(\mathbf{12})}]^T\mathbf{y}} \\
\varepsilon_{\mathbf{12}} &= \frac{\mathbf{s2}\{N_{yy}\mathbf{a}_{(\mathbf{11})}{}^T + (N_{yy} - N_{xx})\mathbf{a}_{(\mathbf{12})}{}^T - N_{xx}\mathbf{a}_{(\mathbf{22})}{}^T\}\mathbf{y}}{[\mathbf{a}_{(\mathbf{11})} \circ \mathbf{a}_{(\mathbf{22})} - \mathbf{a}_{(\mathbf{12})} \circ \mathbf{a}_{(\mathbf{12})}]^T\mathbf{y}}
\end{aligned} \tag{2.20}$$

2.3 Optimization Problem Formulation

Optimization of composite laminates can either be for maximizing the failure load for a fixed ply thickness or minimizing the weight for a fixed failure load threshold. The latter problem has additional design variables for thicknesses. This section demonstrates three ways to solve a laminate optimization problem using MILP/MINLP.

2.3.1 Buckling Load Maximization - Single Level Optimization 1 (SLO1)

Maximization of the failure load having linear buckling constraints can be formulated as a MILP, as shown in [63] and given in section IV. The objective is to maximize the minimum buckling load obtained from different half-sine wave configurations. A maximum of five half-sine waves are chosen in both the x and y directions to capture the minimum value of buckling load factor ($m_{def} = n_{def} = 5$). This is required since the buckling mode number with minimum load factor value is not fixed for composite laminates. The first constraint ensures that the minimum λ of all possible buckling load factors is maximized. The second constraint ensures that only one orientation is assigned to each ply. The third constraint enforces ply contiguity to a maximum of 4 plies of the same orientation, while the fourth constraint

enforces balance by ensuring that every alternate ply of a particular fiber orientation is followed by a ply of the same negative fiber orientation. This constraint requires that the number of symmetric plies is even. The formulation is a MILP optimization with λ_{cr} as a continuous design variable and x_{kl} as a binary variable for $k = 1, \ldots, N$ and $l = 1, \ldots, p$.

$$
\begin{array}{lll}
\textbf{maximize} & \lambda_{cr} & \\
\textbf{w.r.t} & \mathbf{x} & \\
\textbf{s.t.} & \lambda_{cr} \leq \lambda_b(\mathbf{x}, m, n) & m = 1, \ldots, m_{def}; \;\; n = 1, \ldots, n_{def} \\
 & \sum_{l=1}^{p} x_{kl} = 1 & k \; = \; 1, \ldots, N \\
 & \sum_{i=k}^{k+3} x_{li} \leq 4 & k = 1, \ldots, N-4; \;\; l = 1, \ldots, p \\
 & x_{l_1,k} - x_{l_2,k+1} = 0 & \forall \; l_1, l_2 \in \{1, \ldots, p\} \text{ with } \theta_{l_1} = -\theta_{l_2} \\
 & & k = 1, 3, \ldots, N-1 \\
 & \mathbf{x} \in \{0,1\}^{pN} & \\
 & \lambda_{cr} \geq 0 &
\end{array}
$$

2.3.2 Weight Minimization - Single Level Optimization 2 (SLO2)

For the problem focusing on weight minimization, the total number of plies with a fixed ply thickness is used as the minimization function. The buckling load factor formulated with Eq. (2.9) and failure strain from Eq. (2.13) are used as linear and quadratic constraints. The idea is to assume an upper limit for the total number of plies and set the values of corresponding binary variables to 0 or 1 if a ply is occupied or unoccupied, respectively. This maximum limit on the number of plies defines the total number of binary design variables required for the optimization.

Here, the laminate weight is given by $W = \sum_{k=1}^{N} \sum_{l=1}^{p} x_{kl}$ assuming ply thickness and material properties are constant across the laminate. Parameter λ_0 is the design buckling load factor of the laminate. Likewise, parameters $\varepsilon_1^{t,c}, \varepsilon_2^{t,c}$ and ε_{12}^{s} are allowable longitudinal, transverse, and shear strains in tension and compression, respectively evaluated at the buckling load.

$$
\begin{array}{lll}
\textbf{minimize} & W(\mathbf{x}) = \sum_{k=1}^{N}\sum_{l=1}^{p} x_{kl} & \\
\textbf{w.r.t} & \mathbf{x} & \\
\textbf{s.t.} & \lambda_0 \leq \lambda_b(\mathbf{x}, m, n) & m = 1, \ldots, m_{def};\ \ n = 1, \ldots, n_{def} \\
 & \sum_{l=1}^{p} x_{kl} \leq 1 & k\ =\ 1, \ldots, N \\
 & \sum_{i=k}^{k+3} x_{li} \leq 4 & k = 1, \ldots, N-4;\ \ l = 1, \ldots, p \\
 & x_{l_1,k} - x_{l_2,k+1} = 0 & \forall\ l_1, l_2 \in \{1, \ldots, p\} \text{ with } \theta_{l_1} = -\theta_{l_2} \\
 & & k = 1, 3, \ldots, N-1 \\
 & \sum_{l=1}^{p} x_{lk+1} - \sum_{l=1}^{p} x_{kl} \leq 0 & k\ =\ 1, \ldots, N-1 \\
 & \varepsilon_1^k \leq \varepsilon_1^{t,c} & \\
 & \varepsilon_2^k \leq \varepsilon_2^{t,c} & k = 1, \ldots, N \\
 & \varepsilon_{12}^k \leq \varepsilon_{12}^{s} & \\
 & \mathbf{x} \in \{0, 1\}^{pN} &
\end{array}
$$

The second constraint from SLO1 is changed to inequality in SLO2 to allow the laminate to have empty plies. The third and fourth constraints are the same as that from SLO1, whereas the fifth constraint ensures that empty plies, if any, lie on the outside. The problem can be solved as an integer linear program (ILP) with only buckling constraints or a quadratically constrained linear program (QCLP) with the inclusion of strain constraints.

2.3.3 Weight Minimization - Sequential Two-Level Optimization (STLO)

Another way to minimize the weight of a laminate is to change the ply thickness instead of the number of plies. Adding thickness design variables renders both buckling and strain constraints 4th order polynomials in terms of binary design variables (orientation and thickness). The optimization problem can be split into two different optimization problems, which can be solved sequentially. It allows for faster convergence and enables the use of MILP in both subproblems. The STLO process is shown in Figure 2.2.

$$
\begin{array}{llll}
\textbf{minimize} & W = \mathbf{t}^T\mathbf{y} \text{ (Level 2)} & \textbf{maximize} & \lambda_{cr} \text{ (Level 1)} \\
\textbf{w.r.t} & \mathbf{y} & \textbf{w.r.t} & \mathbf{x} \\
\textbf{s.t.} & \lambda_0 \leq \lambda_b(\mathbf{y}, m, n) & \textbf{s.t.} & \lambda_{cr} \leq \lambda_b(\mathbf{x}, m, n) \quad m = 1, \ldots, m_{def} \\
 & & & \qquad\qquad\qquad\qquad\qquad\quad n = 1, \ldots, n_{def} \\
 & \varepsilon_1^k \leq \varepsilon_1^{t,c} & & \sum_{l=1}^{p} x_{kl} = 1 \quad k = 1, \ldots, N \\
 & \varepsilon_2^k \leq \varepsilon_2^{t,c} & & \sum_{i=k}^{k+3} x_{li} \leq 4 \quad k = 1, \ldots, N-4 \\
 & & & \qquad\qquad\qquad\qquad\qquad\quad l = 1, \ldots, p \\
 & \varepsilon_{12}^k \leq \varepsilon_{12}^s & & x_{l_1,k} - x_{l_2,k+1} = 0 \quad \forall\ l_1, l_2 \in \{1, \ldots, p\} \\
 & & & \qquad\qquad\qquad\qquad\qquad\quad \text{with } \theta_{l_1} = -\theta_{l_2} \\
 & \mathbf{y} \in \{0,1\}^q & & \lambda_{cr} \geq 0 \\
 & & & \mathbf{x} \in \{0,1\}^{pN}
\end{array}
$$

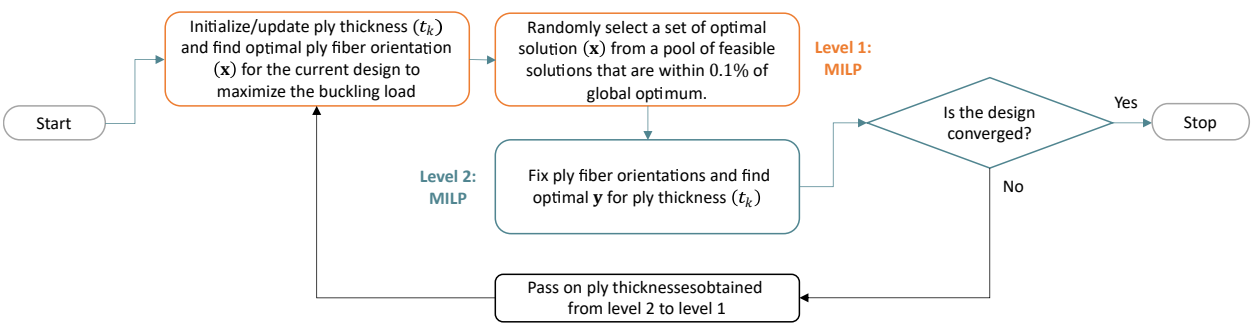

Figure 2.2: Sequential two-level optimization process.

Both optimization levels are solved sequentially and independently, but they share only the optimal ply orientation and thickness information. Level 1 of the optimizer is used to maximize the buckling load for initial ply thickness values. The ply fiber orientations obtained from level 1 are passed on to level 2 as fixed values, and the weight is minimized by finding new values of ply thicknesses. Thickness values obtained from level 2 are passed back to level 1 for stacking sequence optimization.

In level 1, MIP is solved for a global optimum for fiber orientations for fixed ply thicknesses, whereas, at level 2, it is solved for a global optimum for ply thickness for fixed fiber orientations. Even if MILP gives a global optimum solution for maximum buckling load and minimum thickness separately in each level, when two levels are paired together, a global

optimum solution is not guaranteed for the whole problem. The STLO can oscillate between two sub-optimal values. Thus, to improve the chances of finding a global optimum for the entire problem, the information about multiple local optimum solutions for ply stacking sequence optimization (level 1) is used. It is possible that a sub-optimal stacking sequence can yield better ply thickness values and, in turn yields a better solution overall. The solution pool containing values for local optima (buckling load) is used to randomly select a solution within 0.1% of the global optimum. The stacking sequence corresponding to this local solution is passed to level 2 for weight minimization. At the end of each cycle, the best design is retained by comparing it to the previous best. This also mitigates the possibility of oscillation between two sub-optimal solutions.

2.4 Laminate optimization with Uniform Ply Thickness

2.4.1 Optimization for Maximum Buckling Load Design using SLO1

To demonstrate the capability of MILP for different sizes of problems, the results from SLO1 are compared to those from a standard PSO. Initially, the SLO1 is used to optimize laminate configurations with a total number of plies of $2N = 48$ and 144. Each laminate is optimized for a stacking sequence with ply orientations chosen from the following two sets.

$$\begin{aligned} &\text{Set 1: } \Theta \in \{0^\circ, 45^\circ, 90^\circ\} \\ &\text{Set 2: } \Theta \in \{0^\circ, 15^\circ, 30^\circ, 45^\circ, 60^\circ, 75^\circ, 90^\circ\} \end{aligned} \tag{2.21}$$

In the first set, θ can take values in the interval of 45°, whereas in the second set, a 15° interval is used to increase the design space and complexity. The total laminate thickness

is kept constant at 0.24 in. This results in fixed ply thickness of 0.005 in. (=0.24/48) and 0.00167 in. (=0.24/144), respectively, for the two configurations studied here. With advancements in manufacturing technology, it is now possible to make laminates with very thin plies (ply thickness as small as 7.0E-4 in. [76]) that have advantages in terms of material failure over conventional thick plies. The second configuration depicts this by reducing the ply thickness but keeping the overall laminate thickness the same. The buckling load factor is computed for $\frac{N_{yy}}{N_{xx}} = 0.5$ where $N_{xx} = 1$ lb/in.. Material properties used in this study are given in Table 2.1. The optimization is done using commercially available software, *Gurobi* [77], which uses a branch and cut algorithm. All default parameters except '*PoolSearchMode*' are used to set up the solver. The '*PoolSearchMode*' parameter is set to 1 to find multiple nearby optimum values. A machine with an Intel Xeon W2265 (12 cores, 24 threads) CPU and 128 GB RAM is used for all studies. The solver automatically uses parallelization on all cores while performing node search in the branch and bound technique. The optimum buckling load factor values and solver times (given in parenthesis) are compared in Table 2.2 for four cases:

- Case (a): $N = 24$ with Θ set 1.
- Case (b): $N = 72$ with Θ set 1.
- Case (c): $N = 24$ with Θ set 2.
- Case (d): $N = 72$ with Θ set 2.

The optimization is run twice in each case to check its robustness. The optimal stacking sequences obtained using SLO1 are given in Table 2.3.

From the four cases, i.e., $N \in \{24, 72\}$ and $\Theta \in \{\text{Set 1, Set 2}\}$, MILP is much faster than PSO with a solver time of less than 1 second in comparison to 6.36 seconds (on average) for

Table 2.1: Material properties for T300/5208

E_1(msi)	E_2(msi)	G_{12}(msi)	ν_{12}
18.5	1.89	0.93	0.3

Table 2.2: Maximum buckling load factor comparison using SLO1.

Case	λ_{cr} (run time in seconds)			
	PSO		SLO1 with MILP	
	run #1	run #2	run #1	run #2
(a)	9999.12 (6.43)	9999.15 (6.29)	9999.15 (0.12)	9999.15 (0.13)
(b)	10136.14 (180)	10140.26 (180)	10686.17 (0.08)	10686.17 (0.08)
(c)	10059.65 (18.65)	10059.82 (17.96)	10059.87 (0.08)	10059.87 (0.08)
(d)	Ø(180)	Ø(180)	10750.44 (0.1)	10750.44 (0.1)

Note: Ø denotes an infeasible solution resulting from non-convergence of results in 100 PSO iterations.

Table 2.3: Optimal stacking sequence obtained using SLO1 (same sequence is obtained using both runs).

Case	Optimal stacking sequence
(a)	$[\pm 45/90_4/(\pm 45)_3/90_2/\pm 45/90_2/\pm 45/90_4]_S$
(b)	$[(\pm 60)_5/(\pm 75)_2/(\pm 60)_4/\pm 75]_S$
(c)	$[(\pm 45)_2/90_4/\pm 45/90_2/(\pm 45)_2/90_4/\pm 45/90_4/(\pm 45)_4/90_2/\pm 45/90_2/(\pm 45)_3/90_2/$ $\pm 45/90_2/(\pm 45)_3/90_2/(\pm 45)_5/90_2]_S$
(d)	$[(\pm 60)_2/\pm 75/(\pm 60)_5/\pm 75/(\pm 60)_{18}/\pm 75/(\pm 60)_3/\pm 75/(\pm 60)_4]_S$

the PSO for case (a) and upwards of 180 seconds for case (b). The optimal values of PSO and MIP are very close to each other and agree well with those available in the literature [61]. In cases where the number of available orientations is high (cases (b) and (d)), the PSO struggles to obtain a converged solution before the limit of 100 iterations is reached with 1000 particles (100,000 function evaluations). This can be attributed to the large increase in combinatorial space in case (b) and case (d) with $7^{24} = 1.9 \times 10^{20}$ and $7^{72} = 7 \times 10^{60}$ possible orientation combinations respectively. An increase in the combinatorial space significantly increases the total number of local minima. Case (c) has 2.25×10^{35} possible combinations, which are more than case (b), but it is able to converge to an optimum.

One reason for the PSO not being able to converge in the specified time is that, even though the number of possible combinations in case (b) is less than that in case (c), the number of optimal combinations is higher as there are more choices for the optimizer. Another reason might be because of the rounding of continuous design variables to their nearest integer values. The higher the number of orientation values needed to round off, the higher the chances for the PSO to drift away from the optimum. Thus, despite having less number of design variables in case (b), case (c) can converge much faster to the optimal solution. Increasing the number of design variables by increasing the number of plies and orientations renders the PSO inefficient. It cannot yield a feasible solution in a reasonable time frame which is taken to be 180s. The time required for MILP to get a solution is lower than a standard PSO when the problem has a linear objective function and constraints. Therefore, the meager computational cost of MILP can be leveraged in a multi-level formulation.

2.4.2 Optimization for Minimum Weight Design using SLO2

In SLO2, the value of critical buckling load found from the buckling load maximization study is used as the design buckling load factor λ_0 on the panel with $N_{xx} = 1$ lb/in. and $\frac{N_{yy}}{N_{xx}} = 0.5$. The allowable strains are kept constant across layups at $\varepsilon_{11} = 0.008, \varepsilon_{22} = 0.029$ and $\varepsilon_{12} = 0.015$ with an additional safety factor of 1.5. For easier process validation, four cases are chosen for SLO2 that correspond to the four SLO1 cases, with $N_{max} \in \{50, 100\}$ and $\Theta \in \{\text{Set1, Set2}\}$ where N_{max} is the maximum number of plies the laminate can have in the optimization. The four cases for SLO2 are as follows:

- Case (a): $N_{max} = 50$ with ply thickness = 0.005 in. and Θ set 1.
- Case (b): $N_{max} = 50$ with ply thickness = 0.005 in. and Θ set 2.
- Case (c): $N_{max} = 100$ with ply thickness = 0.00167 in. and Θ set 1.

- Case (d): $N_{max} = 100$ with ply thickness = 0.00167 in. and Θ set 2.

The number of binary variables used in each case is given by $N_{max} \times p$. Since the maximum load for the cases with ply thickness of 0.005in. and 0.00167in. from Table 2.2 is used as the limit load, the optimization should return the same number of plies as that used for the corresponding SLO1 cases to obtain the minimum weight design with buckling load constraint. Additionally, the optimization is performed with buckling-only constraints and with both buckling and strain constraints to assess the performance of the QCLP solver. In the absence of bending loads, the strain constraints are computed for each fiber orientation instead of each ply to reduce the total number of constraints in the model. The number of quadratic constraints in such problems equals $6p$ (accounting for both negative and positive strains).

From Table 2.4 and 2.5, SLO2 with ILP obtains a minimum number of plies $N_{opt} = 24$ for case (a) and case (b), and $N_{opt} = 72$ for case (c) and case (d). This is easily validated from SLO1 case inputs. Setting $N_{max} = 50$ leads to 150 binary variables for case (a) and 350 binary variables for case (b), whereas $N_{max} = 100$ leads to 300 and 700 binary variables for case (c) and case (d) respectively. Similar to that observed in SLO1, PSO takes significantly longer to obtain a converged solution for all cases, especially in case (d), where the combinatorial space is large. With the addition of quadratic strain constraints, the optimum number of plies is higher in all the cases compared to buckling-only optimization as seen from Table 2.6 with the laminate stacking sequence provided in Table 2.7. As ply contiguity and adjacency constraints are used, even a small violation of failure constraints leads to adding a ply pair to maintain a balanced configuration leading to designs with only an even number of plies. Additionally, it is observed that there is a significant increase in solution times with the QCLP compared to ILP as the number of design variables is increased. But the actual wall clock time is much less, indicating that the method efficiently solves quadratically constrained

laminate optimization problems.

Table 2.4: Minimum weight optimization with buckling constraints using SLO2.

Case	λ_0	N_{opt} (run time in seconds)			
		PSO		SLO2 with ILP	
		run #1	run #2	run #1	run #2
(a)	9999.15	24 (12.87)	24 (11.56)	24 (0.07)	24 (0.07)
(b)	10686.17	32 (180)	31 (180)	24 (0.1)	24 (0.1)
(c)	10059.87	92 (180)	93 (180)	72 (0.08)	72 (0.08)
(d)	10750.44	Ø(180)	Ø(180)	72 (0.12)	72 (0.12)

Note: Ø denotes an infeasible solution resulting from non-convergence of results in the specified time frame of 180s or 100 PSO iterations.

Table 2.5: Optimal stacking sequence obtained using SLO2 with buckling constraints (the same sequence is obtained using both runs).

Case	Optimal stacking sequence
(a)	$[90_2/(\pm 45)_3/90_2/\pm 45/90_4/\pm 45/90_2/\pm 45/90_2/\pm 45]_S$
(b)	$[(\pm 60)_5/(\pm 75)_4/(\pm 60)_4/\pm 75]_S$
(c)	$[90_4/\pm 45/90_4/\pm 45/90_4/(\pm 45)_7/90_2/(\pm 45)_{13}/90_2/(\pm 45)_6]_S$
(d)	$[(\pm 60)_5/\pm 75/(\pm 60)_6/\pm 75/(\pm 60)_2/\pm 75/(\pm 60)_{12}/\pm 75/(\pm 60)_3/\pm 75/(\pm 60)_3]_S$

Table 2.6: Minimum weight optimization with buckling and strain constraints using SLO2.

Case	λ_0	N_{opt} (run time in seconds)			
		PSO		SLO2 with QCLP	
		run #1	run #2	run #1	run #2
(a)	9999.15	24 (66.45)	24 (68.81)	26 (0.23)	26 (0.23)
(b)	10686.17	Ø(180)	Ø(180)	26 (1.63)	26 (1.64)
(c)	10059.87	Ø(180)	Ø(180)	74 (1.24)	74 (1.25)
(d)	10750.44	Ø(180)	Ø(180)	74 (5.2)	74 (5.18)

Note: Ø denotes an infeasible solution resulting from non-convergence of results in the specified time frame of 180s or 100 PSO iterations.

Table 2.7: Optimal stacking sequence obtained using SLO2 with buckling and strain constraints (the same sequence is obtained using both runs).

Case	Optimal stacking sequence
(a)	$[0_2/90_2/\pm 45/0_2/90_2/\pm 45/90_4/\pm 45/90_2/0_2/(\pm 45)_2]_S$
(b)	$[0_2/(\pm 60)_3/\pm 75/(\pm 60)_3/(\pm 45)_2/(\pm 15)_2/0_2]_S$
(c)	$[0_2/90_4/\pm 45/90_2/\pm 45/90_2/(\pm 45)_8/90_4/\pm 45/90_4/(\pm 45)_8/0_2/$ $\pm 45/0_4/(\pm 45)_2/0_2/\pm 45/0_2]_S$
(d)	$[(\pm 60)_3/\pm 75/\pm 60/(\pm 75)_2/\pm 60/\pm 75/\pm 60/\pm 30/\pm 60/$ $\pm 30/(\pm 60)_2/\pm 75/\pm 45/(\pm 30)_3/90_2/\pm 15/0_2/90_2/(\pm 45)_2/$ $\pm 30/\pm 60/90_2/(\pm 15)_2/\pm 30/0_2/\pm 45/\pm 15/0_2/\pm 15]_S$

2.4.3 Optimization for Minimum Weight Design using Sequential Two-Level Approach (STLO)

In this approach, the STLO is adopted by using MILP at both levels enabling the use of discrete design space for ply thicknesses. Linear expressions of lamination parameters from Eq. (2.9) and Eq. (2.18) are used in level 1 and level 2, respectively, to build buckling constraints. The effect of including strain constraints only at level 2 on the optimization results is also demonstrated. Cases (a) and (d) from the SLO1 optimization study are used for the STLO study.

An initial ply thickness must be specified to run the optimization from level 1. Ply thickness values are chosen from a set $\mathrm{T} = \{0.001\text{in.}, 0.00105\text{in.}, 0.0011\text{in.}, \ldots, 0.008\text{in.}\}$ for case (a) and $\mathrm{T} = \{0.0008\text{in.}, 0.00085\text{in.}, 0.0009\text{in.}, \ldots, 0.003\text{in.}\}$ for case (d). The design is optimized such that the buckling load factor is higher than $\lambda_0 = 9999.15$ and $\lambda_0 = 10,750.44$ with $N_{xx} = 1$ lb/in. and $\frac{N_{yy}}{N_{xx}} = 0.5$. for the two cases respectively. The results compared to those from PSO for discrete thicknesses are given in Table 2.8. The failure load is chosen based on values of the maximum buckling load obtained from the single-level optimization (SLO1). As the thickness values used in SLO1 for cases (a) and (d) are 0.005 in. and 0.00167 in., respectively, the optimizer must output these values as global optimum ply thickness.

Optimization is done using different values of initial ply thicknesses to check the impact of the initial design point (ply thickness) on the solution.

Results in Table 2.8 show the optimal solution for case (a), and Table 2.9 shows optimal values for case (d). It is observed that STLO obtains optimum values for all initial design points considered, and these values can be verified as global optimums from SLO1 and SLO2. The STLO converges in 4 iterations with a run time of fewer than 2 seconds in most cases. This is much faster and more robust than the PSO. As seen in the results for the previous two formulations, the PSO struggles with a higher number of discrete design variables (Table 2.9).

Table 2.8: Optimal result comparison for case (a) using STLO.

Parameters	Runs/ Thickness	Volume (in.^{3})		Ply thickness (in.)		run time (s)	
		B	SB	B	SB	B	SB
PSO with different runs	#1	24	24.24	0.005	0.00505	9.165	15.58
	#2	24	24.24	0.005	0.00505	9.54	13.745
STLO with initial ply thickness (in.)	0.001	24	24	0.005	0.005	1.017	1.78
	0.003	24	24	0.005	0.005	1.32	1.32
	0.005	24	24	0.005	0.005	1.2	1.26
	0.007	24	24	0.005	0.005	1.084	1.104

B - Only buckling constraints.
SB - Strain and buckling constraints.

Even though the results for $(N, \Theta \text{ set}) = (72,\ 2)$ converge for 'buckling constraint only' optimization, the addition of strain constraints increases the ply thickness from 0.0017 in. to over 0.002 in. in all cases. The stacking sequence is optimized in level 1 for buckling constraints only, and the optimal configuration to prevent buckling may or may not be ideal for preventing material failure. Using a fixed stacking sequence during level 2 optimization, which is optimized for buckling load only, can increase ply thickness to satisfy strain constraints. A way to mitigate this and to further improve weight reduction is to use non-

Table 2.9: Optimal result comparison (N=72, Θ set 2) using STLO.

Parameters	Runs/ Thickness	Volume (in.^{3})		Ply thickness (in.)		run time (s)	
		B	SB	B	SB	B	SB
PSO with different runs	#1	Ø	Ø	Ø	Ø	170 (max)	170 (max)
	#2	Ø	Ø	Ø	Ø	170 (max)	170 (max)
STLO with initial ply thickness (in.)	0.001	24.48	24.48	0.0017	0.0017	2.13	3.06
	0.003	24.48	28.8	0.0017	0.002	2.04	1.96
	0.005	24.48	28.8	0.0017	0.002	1.96	1.97
	0.007	24.48	28.8	0.0017	0.002	3.18	2.59

B - Only buckling constraints.
SB - Strain and buckling constraints.
Note: Ø denotes an infeasible solution resulting from non-convergence of results in a predefined number of PSO iterations.

Table 2.10: Comparison between results obtained from SLO2 and STLO.

Constraints	Case	Volume (in.^{3})		Average run time (s)	
		SLO2	STLO	SLO2	STLO
Buckling	(a)	24	24	0.07	1.15
	(d)	24.72	24.48	1.24	2.025
Buckling and Strain	(a)	26	24.24	0.23	1.37
	(d)	24.716	28.8	5.19	2.93

uniform ply thicknesses to change the thickness of only those plies in which strain constraints are violated. In such a scenario, the buckling constraints at level 2 can no longer be simplified directly; they require a reformulation for their linearization. It will also enable the use of hybrid laminates having plies with different materials that have different thicknesses. The application of reformulation linearization techniques (RLT) in laminate optimization is investigated in chapter III.

A comparison between SLO2 and STLO results is also given in Table 2.10. SLO2 and STLO offer two approaches to weight minimization depending on the optimization problems. Both formulations have the same optimal volume when only buckling constraints are included. Any

slight discrepancy is due to the thickness set T used in STLO that does not include the ply thickness value used in SLO2. It forces the optimizer in STLO to choose a higher thickness value from T. This is mainly observed in case (d) results which include strain constraints. SLO2 is much faster than STLO for linear constraints, whereas using quadratic constraints for strains leads to increased computational costs with larger design spaces. STLO has the advantage of having linear constraints for strains, reducing the computational costs in such scenarios.

2.4.4 Scalability with Problem Size

To check the optimization scalability, SLO2 is chosen since it has linear and quadratic constraints. The number of design variables depends on the maximum number of plies N_{max} and the size of orientation set p. The number of linear constraints depends on the number of buckling modes included ($m \times n$), N_{max}, and p. The number of quadratic constraints depends only on p. In this study, the number of buckling modes is fixed at 25 ($m = n = 5$), N_{max}, and p is varied, and the solver time is plotted against these variations in Fig 2.3. It shows the optimizer's efficiency in handling problems with different numbers of plies and orientation values.

Increasing the number of plies by keeping p constant increases the number of linear constraints associated with ply restrictions. It does not increase the number of quadratic constraints associated with strains since only in-plane loads are applied. Although this is the case, since the size of the quadratic coefficient matrix Q increases with the number of design variables, an increased run time is observed with more plies. Increasing the number of orientations by keeping N_{max} constant increases both types of constraints. Moreover, the size and the number of quadratic constraints are increased in such cases. Hence, there is a

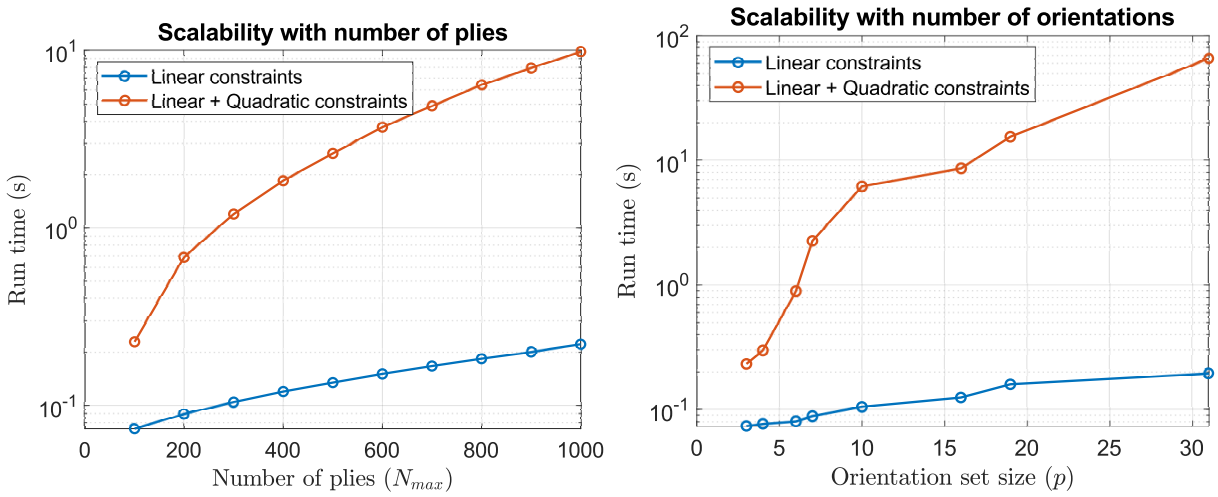

(a) (b)

Figure 2.3: Scalability study; (a) Varying number of plies N_{max} and a fixed number of possible orientations $p = 3$, (b) Varying number of possible orientations p and a fixed number of plies $N_{max} = 100$.

steeper increase in run time when quadratic constraints are involved. The two scalability studies state that the optimization problem can be solved within a minute for a reasonably large number of plies and orientations.

Chapter 3

Optimization of Hybrid Composite Laminates with Distinct ply Thickness

The formulations derived in Chapter II are limited to analyzing laminates having plies of the same thickness and material. In this chapter, the previously employed lamination parameter formulation is extended to enable laminate designs with plies of different thicknesses and materials, thereby leading to MIP with cubic constraints. The linearization techniques are employed to convert cubic constraints of buckling load factors in terms of binary variables into sets of linear constraints that are efficiently solved with optimization algorithms for MIPs.

3.1 Analysis of Hybrid Composite Laminates

A simply-supported symmetric and balanced composite laminated plate similar to the one used in chapter II is subjected to static bi-axial compressive loads λN_{xx} and λN_{yy} in x and y directions, respectively, as shown in Fig. 3.1. The scaling parameter λ is considered the same for the bi-axial compressive loads. The panel has a fixed number of plies N with orientations, $\hat{\theta}_1, \hat{\theta}_2, \cdots$, and $\hat{\theta}_N$, ply thicknesses, $\hat{t}_1, \hat{t}_2, \cdots$, and $\hat{t}_N$ and materials $\hat{\mu}_1, \hat{\mu}_2, \cdots$, and $\hat{\mu}_N$. The panel is assumed to have a fixed and uniform geometry, whereas the material properties are allowed to vary across plies.

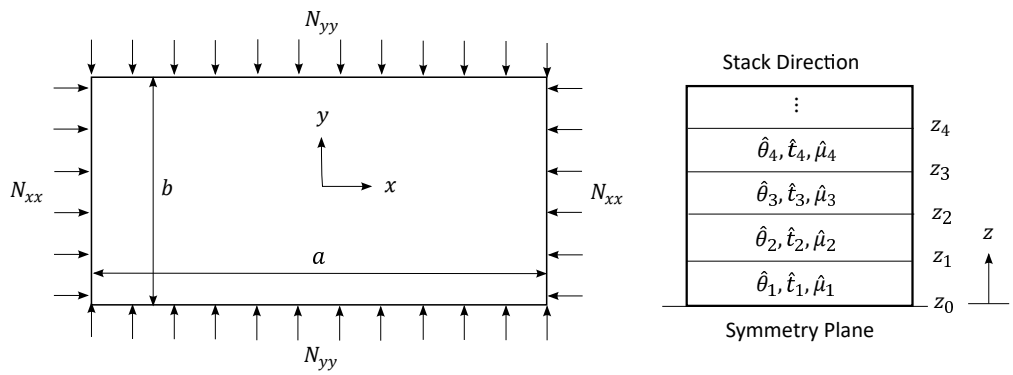

Figure 3.1: Rectangular composite panel subjected to bi-axial loading.

Hybrid unidirectional laminates can be analyzed similarly to conventional laminates using classical lamination theory or first-order shear deformation theory as shown in [78]. The extensional and flexural stiffness elements for hybrid laminates are computed as,

$$
\begin{aligned}
A_{11} &= \sum_{k=1}^{N} \left(U_1^k V_{0A}^k + U_2^k V_{1A}^k + U_3^k V_{3A}^k\right) & D_{11} &= \sum_{k=1}^{N} \left(U_1^k V_{0D}^k + U_2^k V_{1D}^k + U_3^k V_{3D}^k\right) \\
A_{22} &= \sum_{k=1}^{N} \left(U_1^k V_{0A}^k - U_2^k V_{1A}^k + U_3^k V_{3A}^k\right) & D_{22} &= \sum_{k=1}^{N} \left(U_1^k V_{0D}^k - U_2^k V_{1D}^k + U_3^k V_{3D}^k\right) \\
A_{12} &= \sum_{k=1}^{N} \left(U_4^k V_{0A}^k - U_3^k V_{3A}^k\right) & D_{12} &= \sum_{k=1}^{N} \left(U_4^k V_{0D}^k - U_3^k V_{3D}^k\right) \\
A_{66} &= \sum_{k=1}^{N} \left(U_5^k V_{0A}^k - U_3^k V_{3A}^k\right) & D_{66} &= \sum_{k=1}^{N} \left(U_5^k V_{0D}^k - U_3^k V_{3D}^k\right)
\end{aligned}
\tag{3.1}
$$

where $U_i^k, i \in \{1, \ldots, 5\}$ is the invariant of the material of ply k that are defined in terms of

(known) local ply material stiffnesses $Q^k_{jl}, j, l \in \{1, \ldots, 6\}$ as:

$$\begin{aligned}
U^k_1 &= \frac{1}{8}(3Q^k_{11} + 3Q^k_{22} + 2Q^k_{12} + 4Q^k_{66}) \\
U^k_2 &= \frac{1}{2}(Q^k_{11} - Q^k_{22}) \\
U^k_3 &= \frac{1}{8}(Q^k_{11} + Q^k_{22} - 2Q^k_{12} - 4Q^k_{66}) \\
U^k_4 &= \frac{1}{8}(Q^k_{11} + Q^k_{22} + 6Q^k_{12} - 4Q^k_{66}) \\
U^k_5 &= \frac{1}{8}(Q^k_{11} + Q^k_{22} - 2Q^k_{12} + 4Q^k_{66})
\end{aligned} \tag{3.2}$$

and V^k_0, V^k_1, and V^k_3 are dependent on ply orientations and thicknesses as follows:

$$\begin{aligned}
V^k_{0A} &= \frac{2}{3}\left(z_k - z_{k-1}\right) & V^k_{0D} &= \frac{2}{3}\left(z^3_k - z^3_{k-1}\right) \\
V^k_{1A} &= \frac{2}{3}\left(z_k - z_{k-1}\right)\cos 2\hat{\theta}_k & V^k_{1D} &= \frac{2}{3}\left(z^3_k - z^3_{k-1}\right)\cos 2\hat{\theta}_k \\
V^k_{3A} &= \frac{2}{3}\left(z_k - z_{k-1}\right)\cos 4\hat{\theta}_k. & V^k_{3D} &= \frac{2}{3}\left(z^3_k - z^3_{k-1}\right)\cos 4\hat{\theta}_k.
\end{aligned} \tag{3.3}$$

3.2 Buckling Constraint Linearization for Stacking Sequence Optimization

For a bi-axial load case, the buckling load factor is given by Eq. (2.4). Let a composite laminate be made up of N plies with symmetry (total plies = $2N$), and each ply can take a value from a given finite set of orientations $\Theta = \{\theta_1, \theta_2, \ldots, \theta_p\}$. Additionally, each ply can be made from different materials that are chosen from a set $\mathrm{M} = \{\mu_1, \mu_2, \ldots, \mu_h\}$. For a single ply, with p available orientations and h materials to choose from, there are $p \times h$ binary variables associated with it. Thus, for N plies, the total number of binary design variables for the fiber path orientations, including material variations, is $h.p.N$. The vector

$\mathbf{x}$ of binary design variables can be written as

$$\mathbf{x} = [x_{111}, x_{112} \cdots x_{11p}, x_{211}, x_{212} \cdots x_{h1p} \cdots x_{ikl} \cdots x_{1N1}, x_{1N2} \cdots x_{hNp}]^T \tag{3.4}$$

$$\mathrm{X} = \begin{array}{c} \\ \\ \\ \\ \\ \\ \\ \text{Ply} \end{array} \begin{array}{c} \\ \\ \\ \\ \\ \\ \\ \end{array} \begin{array}{c} \mu_1 \qquad\qquad\qquad\qquad \mu_2 \qquad\qquad\qquad\qquad \cdots \quad \mu_i \quad \cdots \quad \mu_h \\ \hline \theta_1 \quad \theta_2 \quad \cdots \quad \theta_p \quad \theta_1 \quad \theta_2 \quad \cdots \quad \theta_p \quad \cdots \quad \theta_l \quad \cdots \quad \theta_p \\ \begin{array}{c} 1 \\ 2 \\ \vdots \\ k \\ \vdots \\ N \end{array} \left(\begin{array}{cccc|cccc|ccc} x_{111} & x_{112} & \cdots & x_{11p} & x_{211} & x_{212} & \cdots & x_{21p} & \cdots & x_{i1l} & \cdots & x_{h1p} \\ x_{121} & x_{122} & \cdots & x_{12p} & x_{221} & x_{222} & \cdots & x_{22p} & \cdots & x_{i2l} & \cdots & x_{h2p} \\ & \vdots & & & & \vdots & & & & \vdots & & \\ x_{1k1} & x_{1k2} & \cdots & x_{1kp} & x_{2k1} & x_{2k2} & \cdots & x_{2kp} & \cdots & x_{ikl} & \cdots & x_{hkp} \\ & \vdots & & & & \vdots & & & & \vdots & & \\ x_{1N1} & x_{1N2} & \cdots & x_{1Np} & x_{2N1} & x_{2N2} & \cdots & x_{2Np} & \cdots & x_{iNl} & \cdots & x_{hNp} \end{array}\right) \end{array} \tag{3.5}$$

where, x_{ikl} is the binary variable associated with ply k having an orientation $\theta_l \in \Theta$ and material $\mu_i \in \mathrm{M}$ i.e., $x_{ikl} = 1$ if the ply k has orientation θ_l with material μ_i and 0 otherwise. Note that for each ply k, $\sum_{i=1}^{h} \sum_{l=1}^{p} x_{ikl} = 1$ ensures that only one orientation and one material are assigned to the ply. The design variable vector for hybrid laminates, when reshaped as a matrix, takes the form X as (3.5).

For example, a hybrid composite laminate made of CFRP and GFRP plies with stacking sequence $\left[\pm 45^C / 0_2^C / 90_2^G\right]_S$ will form a matrix as shown in Eq. (3.6). The superscripts C and G on the angles in the stacking sequence are used to represent the ply material (C: CFRP, G: GFRP). Based on the definition of the stacking sequence of laminates given in Fig. 3.1,

the matrix of X is given in the following

$$
\mathrm{X} = \begin{array}{c} \\ 1 \\ 2 \\ 3 \\ 4 \\ 5 \\ 6 \end{array}
\begin{array}{c}
\begin{array}{cccccc} \text{CFRP} & & & \text{GFRP} & & \\ \hline 0^\circ & 45^\circ & 90^\circ & 0^\circ & 45^\circ & 90^\circ \end{array} \\
\left(\begin{array}{ccc|ccc}
0 & 0 & 0 & 0 & 0 & 1 \\
0 & 0 & 0 & 0 & 0 & 1 \\
1 & 0 & 0 & 0 & 0 & 0 \\
1 & 0 & 0 & 0 & 0 & 0 \\
0 & 1 & 0 & 0 & 0 & 0 \\
0 & 1 & 0 & 0 & 0 & 0
\end{array}\right)
\end{array}
\tag{3.6}
$$

As a result, the lamination parameters for ply k and material i from Eq. (3.3) can be expressed in terms of x_{ikl} as

$$
\begin{aligned}
V_{0Di}^{k} &= \frac{2}{3}\left[(z_k^3 - z_{k-1}^3)\sum_{l=1}^{p} x_{ikl}\right] \\
V_{1Di}^{k} &= \frac{2}{3}\left[(z_k^3 - z_{k-1}^3)\sum_{l=1}^{p} x_{ikl}\cos 2\theta_l\right] \\
V_{3Di}^{k} &= \frac{2}{3}\left[(z_k^3 - z_{k-1}^3)\sum_{l=1}^{p} x_{ikl}\cos 4\theta_l\right]
\end{aligned}
\tag{3.7}
$$

Substituting Eq. (3.7) in Eq. (3.1), the expressions for flexural stiffness in binary variables are written as

$$
\begin{aligned}
D_{11} &= \sum_{k=1}^{N}\sum_{i=1}^{h}\left(U_{1i}^{k}V_{0Di}^{k} + U_{2i}^{k}V_{1Di}^{k} + U_{3i}^{k}V_{3Di}^{k}\right) \\
D_{22} &= \sum_{k=1}^{N}\sum_{i=1}^{h}\left(U_{1i}^{k}V_{0Di}^{k} - U_{2i}^{k}V_{1Di}^{k} + U_{3i}^{k}V_{3Di}^{k}\right) \\
D_{12} &= \sum_{k=1}^{N}\sum_{i=1}^{h}\left(U_{4i}^{k}V_{0Di}^{k} - U_{3i}^{k}V_{3Di}^{k}\right) \\
D_{66} &= \sum_{k=1}^{N}\sum_{i=1}^{h}\left(U_{5i}^{k}V_{0Di}^{k} - U_{3i}^{k}V_{3Di}^{k}\right)
\end{aligned}
\tag{3.8}
$$

The ply thickness is assumed to be fixed while optimizing for stacking sequence, which makes the expressions in Eq. (3.8) linear functions of $\mathbf{x}$. Writing the flexural stiffnesses in vector form, i.e., using each term that is inside the summation as a vector element, the stiffnesses D_{11}, D_{22}, D_{12}, and D_{66} can be represented as

$$
D_{11} = \mathbf{d}_{(\mathbf{11})}{}^{T}\mathbf{x}; \quad D_{22} = \mathbf{d}_{(\mathbf{22})}{}^{T}\mathbf{x}; \quad D_{12} = \mathbf{d}_{(\mathbf{12})}{}^{T}\mathbf{x}; \quad D_{66} = \mathbf{d}_{(\mathbf{66})}{}^{T}\mathbf{x} \tag{3.9}
$$

where $\mathbf{d}_{(\mathbf{uv})}, u, v \in \{(1,1),(2,2),(1,2),(6,6)\}$, are vectors of size hpN whose elements $d_{(uv)}^{ilk}$ represent the flexural stiffness D_{uv} of ply k having an orientation θ_l and material μ_i. The optimal combination of x_{ikl} will result in the desired values of flexural stiffnesses in Eqn (3.9).

3.3 Buckling Constraint Linearization for Distinct Ply Thickness

Constraint formulation in terms of ply thickness variables follows a similar process as that for stacking sequence variables. The difference is that the bending stiffness matrix, $\boldsymbol{D}$, is

a cubic function of ply thickness (see Eqs. (3.1) and (3.3)). Let $\mathbf{y}$ be the vector of binary design variables associated with a finite set of thickness values $\mathrm{T} = \{t_1, t_2, \cdots, t_q\}$ such that

$$\mathbf{y} = [y_{11}, y_{12} \cdots y_{1q}, y_{21}, y_{22} \cdots y_{2q} \cdots y_{kl} \cdots y_{N1}, y_{N2} \cdots y_{Nq}]^T \tag{3.10}$$

where, y_{kl} is the binary variable associated with ply k and thickness $t_l \in \mathrm{T}$ similar to that used in Chapter II. The lamination parameters V_{0D}, V_{1D} and V_{3D} are cubic functions of ply thickness coordinates z_k. Note that the fiber orientations and the ply materials are fixed when optimizing for ply thicknesses. Thus, for a fixed value of ply fiber orientation $\hat{\theta}_k \in \Theta$ and material $\hat{\mu}_k \in \mathrm{M}$, Eq. (3.7) for a symmetric layup can be rewritten as:

$$\begin{aligned} V_{0D}^k &= \frac{2}{3}(z_k^3 - z_{k-1}^3) \\ V_{1D}^k &= \frac{2}{3}(z_k^3 - z_{k-1}^3)\cos 2\hat{\theta}_k \\ V_{3D}^k &= \frac{2}{3}(z_k^3 - z_{k-1}^3)\cos 4\hat{\theta}_k \end{aligned} \tag{3.11}$$

3.3.1 Overview of Reformulation Techniques used for Constraint Linearization

The coupled expressions in terms of binary variables resulting from Eq. (3.11) include a combination of linear, quadratic, and cubic terms in the elements of $\mathbf{y}$ (presented later in Section VI.B). Therefore, the cubic problem has to be linearized before passing it on to the MILP solver. This can be achieved using reformulation techniques given by Chang [66] and Adam-Forrester [67]. These techniques simplify the actual non-linear problem by adding auxiliary continuous variables that represent the product of two or more binary variable terms. By imposing additional linear constraints on auxiliary variables, the solution of each reformulated problem is the same as that of the original problem. A brief description of the

above-mentioned linearization techniques is given next.

Chang's Linearization Approach

Let a general cubic constraint be written as

$$l(\mathbf{x},\mathbf{w}) + \sum_{i=1}^{n} g_i(\mathbf{x},\mathbf{w})x_i + \sum_{i=1}^{n}\sum_{j=1}^{i-1} h_{ij}(\mathbf{x},\mathbf{w})x_i x_j \geq C, \tag{3.12}$$

where $\mathbf{x} \in \{0,1\}^n$ and $\mathbf{w} \in \mathbb{R}^{n_w}$. In Eqn. (3.12), $l(\mathbf{x},\mathbf{w}), g(\mathbf{x},\mathbf{w})$ and $h(\mathbf{x},\mathbf{w})$ are linear functions of binary variables $\mathbf{x}$ and continuous variables $\mathbf{w}$ whereas C is a constant. Each quadratic expression $g_i(\mathbf{x},\mathbf{w})x_i$ is replaced by a continuous design variable ξ_i and similarly, the cubic expression $h_{ij}(\mathbf{x},\mathbf{w})x_i x_j$ is replaced by continuous design variables η_{ij}. This results in a reformulation given in (3.13) with additional constraints given in (3.14). In these inequalities, G_i and H_{ij} are known bounds that must be greater than the maximum absolute value that functions g_i and h_{ij} can attain, respectively. The set of linear inequalities given in (3.14) make sure that ξ_i and η_{ij} attain a value which is equal to $g_i(\mathbf{x},\mathbf{w})x_i$ and $h_{ij}(\mathbf{x},\mathbf{w})x_i x_j$ respectively in the original expression. Specifically, if the variable $x_i = 0$, (3.14b) forces ξ_i to be 0 and (3.14d) forces η_{ij} to be 0, thus making sure that both $g_i(\mathbf{x},\mathbf{w})x_i$ and $h_{ij}(\mathbf{x},\mathbf{w})x_i x_j$ are 0. If $x_i = 1$, the (3.14a) constraints ξ_i to be equal to $g_i(\mathbf{x},\mathbf{w})$. Similarly, if both x_i and x_j are equal to 1, the third constraint forces η_{ij} to be equal to $h_{ij}(\mathbf{x},\mathbf{w})$ as expected from the original expression. The set of equations can be viewed as 'if else' statements written in mathematical form to allow conditional statement implementations in MILP solvers.

$$l(\mathbf{x},\mathbf{w}) + \sum_{i=1}^{n} \xi_i + \sum_{i=1}^{n}\sum_{j=1}^{i-1} \eta_{ij} \geq C \tag{3.13}$$

$$|G_i|(1-x_i) + g_i(\mathbf{x},\mathbf{w}) \geq \xi_i \geq |G_i|(x_i - 1) + g_i(\mathbf{x},\mathbf{w}) \tag{3.14a}$$

$$|G_i|x_i \geq \xi_i \geq -|G_i|x_i \tag{3.14b}$$

$$|H_{ij}|(2 - x_i - x_j) + h_{ij}(\mathbf{x}, \mathbf{w}) \geq \eta_{ij} \geq |H_{ij}|(x_i + x_j - 2) + h_{ij}(\mathbf{x}, \mathbf{w}) \tag{3.14c}$$

$$|H_{ij}|x_i \geq \eta_{ij} \geq -|H_{ij}|x_i \tag{3.14d}$$

$$|H_{ij}|x_j \geq \eta_{ij} \geq -|H_{ij}|x_j \tag{3.14e}$$

The reformulated problem has a maximum of $n(n+1)/2$ additional continuous variables and $5n(n+1)$ additional linear constraints.

Adam-Forrester's Linearization Approach

As opposed to Chang's model, Adam-Forrester's model uses Glover's technique [79] (a method to linearize quadratic terms) twice to reduce the total number of additional constraints required for reformulation. To apply Glover's method, the cubic constraint in (3.12) is rearranged as

$$l(\mathbf{x}, \mathbf{w}) + \sum_{i=1}^{n} \left[g_i(\mathbf{x}, \mathbf{w}) + \sum_{j=1}^{i-1} h_{ij}(\mathbf{x}, \mathbf{w}) x_j \right] x_i \geq C. \tag{3.15}$$

In the first step, $h_{ij}(\mathbf{x}, \mathbf{w})x_j$ in (3.15) is replaced by continuous variables η_{ij} with four additional inequalities, as follows:

$$l(\mathbf{x}, \mathbf{w}) + \sum_{i=1}^{n} \left[g_i(\mathbf{x}, \mathbf{w}) + \sum_{j=1}^{i-1} \eta_{ij} \right] x_i \geq C \tag{3.16}$$

$$\begin{aligned} &h_{ij}(\mathbf{x}, \mathbf{w}) - H_{ij}^{-}(1 - x_j) \geq \eta_{ij} \geq h_{ij}(\mathbf{x}, \mathbf{w}) - H_{ij}^{+}(1 - x_j) \\ &H_{ij}^{+} x_j \geq \eta_{ij} \geq H_{ij}^{-} x_j \end{aligned} \tag{3.17}$$

Here, H_{ij}^{-} and H_{ij}^{+} are lower and upper bounds on $h_{ij}(\mathbf{x}, \mathbf{w})$ respectively. In the second step, the term inside the square bracket that is multiplied by x_i in (3.16) is replaced by another

continuous variable ξ_i and four more inequalities. The final reformulation is given as

$$l(\mathbf{x}, \mathbf{w}) + \sum_{i=1}^{n} \xi_i \geq C \tag{3.18}$$

with inequalities (3.17) and

$$\begin{gathered} g_i(\mathbf{x}, \mathbf{w}) + \sum_{j=1}^{i-1} \eta_{ij} - G_i^-(1 - x_j) \geq \xi_i \geq g_i(\mathbf{x}, \mathbf{w}) + \sum_{j=1}^{i-1} \eta_{ij} - G_i^+(1 - x_j) \\ G_i^+ x_i \geq \xi_i \geq G_i^- x_i, \end{gathered} \tag{3.19}$$

where G_i^- and G_i^+ are lower and upper bounds on $g_i(\mathbf{x}, \mathbf{w})$ respectively. Similar to Chang's model, (3.17) and 3.19 are mathematical representations of conditional statements. This model requires $n(n+1)/2$ additional continuous variables but $4n(n+1)$ additional linear constraints. In case of problems where the design parameter values must always be positive, $G_i^- x_i = H_{ij}^- x_j = 0$ and the number of additional constraints reduce to $3n(n+1)$.

Both models require the same number of additional variables, but Adam-Forrester's model requires $2n(n+1)$ fewer constraints, i.e., four fewer additional constraints for every additional variable. An important difference between the two models lies in the design variable definition. The additional variables are defined as independent variables for quadratic and cubic terms in the case of Chang's model. In contrast, the additional variables representing the quadratic terms are coupled with those representing the cubic terms in Adam-Forrester's model. The lamination parameters are reformulated using both models, and the optimization results are compared to study the impact of two different reformulations on solver efficiency.

3.3.2 Reformulation of Stiffness Parameters

To apply reformulation techniques for the laminate problem, the expressions for flexural stiffnesses in Eqn. (3.1) must be simplified into sets of linear, bi-linear, and tri-linear terms that can be arranged in the form given on the left-hand side of (3.12) and (3.15). For the simplification process, first, Eqn. (3.10) is written as a matrix of sub-vectors of $\mathbf{y}$ having size $q \times N$ that correspond to individual plies.

$$Y = \left[\mathbf{y}_{(1)}, \mathbf{y}_{(2)}, \ldots, \mathbf{y}_{(k)}, \ldots, \mathbf{y}_{(N)}\right] \tag{3.20}$$

where the sub-vectors or columns are

$$\begin{aligned} \mathbf{y}_{(1)} &= [y_{11}, y_{12}, \cdots, y_{1q}]^T \\ \mathbf{y}_{(2)} &= [y_{21}, y_{22}, \cdots, y_{2q}]^T \\ &\vdots \\ \mathbf{y}_{(N)} &= [y_{N1}, y_{N2}, \cdots, y_{Nq}]^T \end{aligned} \tag{3.21}$$

Next, a vector of functions $\mathbf{r} = [r_1, r_2, \cdots, r_N]$ is defined such that the elements of $\mathbf{r}$ are linear expressions that represent the thickness of each ply of the laminate, i.e.,

$$\begin{aligned} r_1 &= t_1 y_{11} + t_2 y_{12} + \cdots + t_q y_{1q} \\ r_2 &= t_1 y_{21} + t_2 y_{22} + \cdots + t_q y_{2q} \\ &\vdots \\ r_N &= t_1 y_{N1} + t_2 y_{N2} + \cdots + t_q y_{Nq} \end{aligned} \tag{3.22}$$

Using the fact that only one thickness value can be assigned to each ply, i.e., $\sum_{j=1,\ldots,q} y_{ij} = 1$ for all $i \in \{1, \ldots, N\}$, the square and cube of elements of $\mathbf{r}$ can be defined, i.e., $\mathbf{r}^{\circ 2} =$

$[r_1^2, r_2^2, \cdots, r_N^2]$ and $\mathbf{r}^{\circ 3} = [r_1^3, r_2^3, \cdots, r_N^3]$ as a linear function of y, i.e.,

$$\begin{aligned} r_i^2 = (t_1)^2 y_{i1} + (t_2)^2 y_{i2} + \cdots + (t_q)^2 y_{iq} &= \left(\mathbf{t}^{\circ 2}\right)^T \mathbf{y}_{(i)} \\ \therefore \mathbf{r}^{\circ 2} &= \left(\mathbf{t}^{\circ 2}\right)^T \mathrm{Y} \\ \mathbf{r}^{\circ 3} &= \left(\mathbf{t}^{\circ 3}\right)^T \mathrm{Y} \end{aligned} \tag{3.23}$$

Lastly, z_k (distance of the top surface of ply k from the plane of symmetry) can be written in terms of elements of $\mathbf{r}$ as shown in Eqn. (3.24)

$$z_k = \sum_{i=1}^{k} r_i \tag{3.24}$$

Now, after defining the basic parameters required for simplification, the flexural stiffnesses D_{uv} where, $u, v \in \{(1,1), (2,2), (1,2), (6,6)\}$ are written as

$$D_{uv} = \sum_{k=1}^{N} \left(z_k^3 - z_{k-1}^3\right) c_k \tag{3.25}$$

where, c_k is a constant that depends on material invariants from Eq. (3.2) and fiber orientations of ply k i.e., $\hat{\theta}_k$. The decomposition of Eqn. (3.25) into linear, quadratic, and cubic terms is done using well-known mathematical identities and previously established parameters in Eqn. (3.22), (3.23) and (3.24). Using the identity for the difference between two cubes, $z_k^3 - z_{k-1}^3$ can be written as

$$z_k^3 - z_{k-1}^3 = (z_k - z_{k-1})^3 + 3(z_k - z_{k-1}) z_k z_{k-1} \tag{3.26}$$

From Eqn. (3.24), $z_k - z_{k-1} = r_k$ and thus, Eqn. (3.26) becomes

$$z_k^3 - z_{k-1}^3 = r_k^3 + 3 r_k z_k z_{k-1} \tag{3.27}$$

Similarly, the second term on the right-hand side of Eqn. (3.27) can be written as

$$3r_k z_k z_{k-1} = 3r_k(r_k + z_{k-1})z_{k-1} = 3r_k^2 \sum_{i=1}^{k-1} r_i + 3r_k \left(\sum_{i=1}^{k-1} r_i \right)^2 \tag{3.28}$$

Equation (3.28) can be further simplified by expanding and rearranging the square of the summation of r_i as shown in Eqn. (3.29).

$$\left(\sum_{i=1}^{k-1} r_i \right)^2 = \sum_{i=1}^{k-1} r_i^2 + 2 \sum_{i=1}^{k-1} \sum_{j=1}^{i-1} r_i r_j \tag{3.29}$$

From Eqns. (3.26), (3.27), (3.28) and (3.29), the flexural stiffness expression can be written in terms of r as

$$D_{uv} = \sum_{k=1}^{N} \left(r_k^3 + 3r_k^2 \sum_{i=1}^{k-1} r_i + 3r_k \sum_{i=1}^{k-1} r_i^2 + 6r_k \sum_{i=1}^{k-1} \sum_{j=1}^{i-1} r_i r_j \right) c_k \tag{3.30}$$

From Eqn. (3.23), $r_i^2 = \left(\mathbf{t}^{\circ 2}\right)^T \mathbf{y}_{(i)}, r_k^2 = \left(\mathbf{t}^{\circ 2}\right)^T \mathbf{y}_{(k)}$ and $r_k^3 = \left(\mathbf{t}^{\circ 3}\right)^T \mathbf{y}_{(k)}$. Thus, the final expression for flexural stiffnesses in terms of ply thickness binary variables becomes

$$\begin{aligned} D_{uv} = \sum_{k=1}^{N} \Bigg[& \left(\mathbf{t}^{\circ 3}\right)^T \mathbf{y}_{(k)} + 3 \left(\mathbf{t}^{\circ 2}\right)^T \mathbf{y}_{(k)} \sum_{i=1}^{k-1} \mathbf{t}^T \mathbf{y}_{(i)} + 3\mathbf{t}^T \mathbf{y}_{(k)} \sum_{i=1}^{k-1} \left(\mathbf{t}^{\circ 2}\right)^T \mathbf{y}_{(i)} \\ & + 6\mathbf{t}^T \mathbf{y}_{(k)} \sum_{i=1}^{k-1} \sum_{j=1}^{i-1} \mathbf{t}^T \mathbf{y}_{(i)} \mathbf{t}^T \mathbf{y}_{(j)} \Bigg] c_k. \end{aligned} \tag{3.31}$$

Equation (3.31) contains terms that are separated into sets having linear, quadratic, and

cubic dependencies on $\mathbf{y}$.

Linear terms:	$\left(\mathbf{t}^{\circ 3}\right)^T \mathbf{y}_{(k)}$
Quadratic terms:	$3\left(\mathbf{t}^{\circ 2}\right)^T \mathbf{y}_{(k)} \sum_{i=1}^{k-1} \mathbf{t}^T \mathbf{y}_{(i)} + 3\mathbf{t}^T \mathbf{y}_{(k)} \sum_{i=1}^{k-1} \left(\mathbf{t}^{\circ 2}\right)^T \mathbf{y}_{(i)}$
Cubic terms:	$6\mathbf{t}^T \mathbf{y}_{(k)} \sum_{i=1}^{k-1} \sum_{j=1}^{i-1} \mathbf{t}^T \mathbf{y}_{(i)} \mathbf{t}^T \mathbf{y}_{(j)}$

The expression for D_{uv} in Eqn. (3.31) is in the required form, in which linearization techniques of both Chang [66] and Adam-Forrester [67] can be employed.

3.3.3 Implementation of Cubic Linearization Techniques

The use of reformulation techniques exponentially increases the size of the optimization problem. The problem size of optimizing a laminate with distinct ply thicknesses depends on the total number of plies N and cardinality of the thickness set T, i.e., $|\mathrm{T}| = q$. With the simplified formulation, the maximum number of additional variables required for reformulation is given by $Nq + {}^{N}C_3$. The first term (Nq) represents additional variables required for quadratic reformulation and the second term $({}^{N}C_3)$ denotes the number of variables that are needed for cubic reformulation. This is a significant increase in the design space which needs to be reduced to increase MILP solver efficiency. The dependency on the number of plies can be eliminated by means of variable linking. In this study, it is assumed that plies with the same orientations also have the same thickness values. This makes the thickness optimization dependent on the number of unique orientations assigned to the laminate. The maximum number of additional design variables is restricted to $n_u q + {}^{n_u}C_3$ where $n_u \leq hp$ is the number of unique non-negative orientations in the layup of a balanced laminate.

By using variable linking, Eqn. (3.31) can be further simplified by rewriting the product of

the same binary variables as the variable itself. The newly formed linear and quadratic terms can be combined with the existing linear and quadratic parts of the expressions reducing the total number of unique cubic terms to operate on. Another advantage of linking is that it helps to maintain a balanced and symmetric configuration without the need for additional constraints. A comparison of design space with and without variable linking for different stacking sequences and single buckling constraints is shown in Table 3.1. The stacking sequences Table 3.1 are given as follows:

1. Layup 1: $[0/90/\pm 45/90/0]_S$
2. Layup 2: $[0/\pm 30/\pm 45/90_2/0]_S$
3. Layup 3: $[0/\pm 30/\pm 45/\pm 60/90]_S$
4. Layup 4: $[0/\pm 15/\pm 30/\pm 45/\pm 60/\pm 75/90]_S$

From the data for the first two layups, the addition of new plies significantly increases the number of unlinked (additional) variables. On the contrary, increasing the set size q has a relatively small effect on the design space. From the last layup, the gap between the number of unlinked and linked variables decreases as the number of unique orientations increases. Design variable linking is used in the STLO process to efficiently find optimum thickness values for every orientation.

3.4 Optimization Problem Formulation

Based on the STLO framework shown in Fig. 2.2, the optimization problem of weight or cost minimization is split into two different optimization subproblems, which are solved in a sequential manner.

Table 3.1: Design space comparison with linked and unlinked variables in distinct ply thickness optimization.

Layup	q	n_u	No. of base variables		No. of additional variables	
			Unlinked	Linked	Unlinked	Linked
1	9	3	54	27	1674	108
2	9	4	72	36	4608	360
3	11	5	88	55	6864	1265
4	15	7	180	105	49680	7980

$$
\begin{array}{llll}
\textbf{minimize} & W \text{ or } C \text{ (Level 2)} & \textbf{maximize} & \lambda_{cr} \text{ (Level 1)} \\
\textbf{w.r.t} & \mathbf{y} & \textbf{w.r.t} & \mathbf{x} \\
\textbf{s.t.} & \lambda_b(\mathbf{y}, m, n) \geq 1 & \textbf{s.t.} & \lambda_{cr} \leq \lambda_b(\mathbf{x}, m, n) \qquad m = 1, \ldots, m_{def}, \\
 & & & \qquad n = 1, \ldots, n_{def} \\
 & \mathbf{y} \in \{0,1\}^{n_u q} & & \sum_{i=1}^{h} \sum_{l=1}^{p} x_{ikl} = 1 \qquad k = 1, \ldots, N \\
 & & & \sum_{j=k}^{k+4} x_{ilj} \leq 4 \qquad k = 1, \ldots, N-2, \\
 & & & \qquad l = 1, \ldots, p \\
 & & & \qquad i = 1, \ldots, h \\
 & & & x_{i_1,l_1,k} - x_{i_2,l_2,k+1} = 0 \quad \forall\ l_1, l_2 \in \{1, \ldots, p\}, \\
 & & & \qquad i_1, i_2 \in \{1, \ldots, h\}, \\
 & & & \qquad \text{with } \theta_{l_1} = -\theta_{l_2} \\
 & & & \sum_{l=1}^{p} \sum_{k=1}^{N} x_{ikl} \geq N_i \qquad i = 1, \ldots, h \\
 & & & \lambda_{cr} \geq 0 \\
 & & & \mathbf{x} \in \{0,1\}^{hpN}
\end{array}
$$

The first constraint in level 1 ensures that the minimum λ_b of all possible buckling load factors is maximized. The second constraint ensures that only one orientation and one material are assigned to each ply. The third constraint enforces ply contiguity to a maximum of 4 plies of the same orientation. The fourth constraint enforces balance by ensuring that every alternate ply of a particular fiber orientation is followed by a ply of the same negative fiber orientation; this constraint requires that the number of symmetric plies is even. Finally, the fifth constraint is imposed to maintain a minimum number of plies N_i of material μ_i. Level 2 is used to adjust the thicknesses of each ply once and thus, only includes the buckling load constraint.

3.5 Hybrid Laminate Optimization Results

The optimization is done initially to maximize the buckling load factor of non-hybrid and hybrid laminates. The weight minimization results using distinct ply thicknesses are presented thereafter. Plies made of CFRP and GFRP are considered for hybridization with different ratios. The material properties (μ_1 : CFRP, μ_2 : GFRP) used in this study are given in Table 3.2. Two sets of orientations are chosen as shown in Eq (3.32) with $p = 3$ and $p = 7$. The optimization is done using commercially available software, *Gurobi* [77] which uses the branch and cut algorithm. All default parameters except '*PoolSearchMode*' are used to set up the solver. The '*PoolSearchMode*' parameter is set to 1 to find multiple nearby optimum values. A machine with an Intel Xeon W2265 (12 cores, 24 threads) CPU and 128 GB RAM is used for all studies. The solver automatically uses parallelization on all cores while performing node search in the branch and cut technique.

$$\begin{aligned} &\text{Set 1: } \Theta \in \{0^\circ, 45^\circ, 90^\circ\} \\ &\text{Set 2: } \Theta \in \{0^\circ, 15^\circ, 30^\circ, 45^\circ, 60^\circ, 75^\circ, 90^\circ\} \end{aligned} \tag{3.32}$$

Table 3.2: Material properties [8].

Material	E_1(MPa)	E_2(MPa)	G_{12}(MPa)	ν_{12}	Mass density ρ (kg/mm^3)	Cost factor α
CFRP	181E+03	10.3E+03	7.17E+03	0.28	1.6E-06	8
GFRP	38.6E+3	8.27E+03	4.14E+03	0.26	1.8E-06	1

3.5.1 Buckling Load Maximization (STLO Level 1)

STLO level 1 is used for buckling load maximization studies. The total number of plies is fixed to $N = 64$ to validate results with the literature. A constraint is added to the problem

to set the minimum number of GFRP plies. This is crucial as the optimization without this constraint will always result in the laminate with all plies made of the material with the highest bending stiffness. The laminate length $a = 508$ mm is chosen with an aspect ratio $a/b = 2$. The ply thickness is fixed at $t = 0.127$ mm for all plies. The results from STLO level 1 using MILP are compared with those obtained from GA and given by Karakaya [8]. A GA with a generalized elitist selection method is used as demonstrated in [80]. In GA, the maximization problem is solved as a minimization problem with a negative objective using the exterior penalty function for constraint satisfaction. The problem thus solved is the one to minimize $-\lambda_{cr} + \sum_{i=1}^{n} P_i \max[0, g_i]^2$. Here, P_i is a penalty factor and $g_i \leq 0$ is a constraint. The design variables are integers with values 1 to p that represent every angle from Θ. A population size of 50 used with 200 generations, mutation probability of 0.1, uniform crossover, roulette selection, and the elitist ratio of 0.04 provided the best results. The penalty factor is set to 100 to be in the same order of magnitude as the buckling load factor. The best of 20 GA runs is used for comparison.

Table 3.3: Maximum buckling load factor comparison using STLO level 1, $N = 64$, $N_x = N_y = 1$N/mm, $a/b = 2$, Set 1 as Θ.

Study	Minimum GFRP %	Mass (kg)	λ_{cr}			(N_C, N_G)
			GA	MILP	Karakaya [8]	
1	0	1.678	940.56	940.56	940.66	(64, 0)
2	50	1.783	851.286	852.24	835.83	(32, 32)
3	75	1.835	640.66	645.25	636.652	(16, 48)
4	87.5	1.862	458.02	470.49	488.78	(8, 56)

The buckling load maximization results are given in Table 3.3 along with stacking sequences in Table 3.4. The applied load is fixed at $N_x = N_y = 1$N/mm. A minimum GFRP % is specified as a constraint which results in four studies with different numbers of CFRP and GFRP plies. The results match well with the literature with both, GA and MILP. The discrepancy between values obtained using MILP and Karakaya is due to the latter being

Table 3.4: Optimal stacking sequence obtained using MILP for studies in Table 3.3.

Study	Optimal stacking sequence
1	$\left[90_4^C/\pm 45^C/90_4^C/\pm 45^C/90_2^C/\pm 45^C/90_4^C/(\pm 45)_2^C/90_4^C/\pm 45^C/90_2^C\right]_S$
2	$\left[90_4^C/\pm 45^C/90_4^C/\pm 45^C/90_2^C/\pm 45^C/90_4^G/\pm 45^G/90_4^G/\pm 45^G/90_4^G\right]_S$
3	$\left[90_2^C/\pm 45^C/90_4^C/90_2^G/\pm 45^G/90_4^G/(\pm 45)_2^G/90_4^G/\pm 45^G/90_4^G/\pm 45^G\right]_S$
4	$\left[90_4^C/(\pm 45)_7^G/90_2^G/(\pm 45)_2^G/90_2^G/(\pm 45)_3^G\right]_S$

obtained without ply adjacency constraints. In the literature, the number and the location of GFRP plies are fixed before optimization but in this study, a constraint is put only on the minimum number of plies. From Table 3.4, the optimization automatically groups the GFRP plies in the middle while the CFRP plies are laid outside to maximize the bending stiffness as expected.

Table 3.5: Performance scaling comparison between GA and MILP for buckling load maximization of hybrid laminates with a minimum 50% GFRP plies, $N_x = N_y = 1$N/mm, $a/b = 2$.

Θ	N	t_k (mm)	Variables		λ_{cr}		Solver time (s)	
			GA	MILP	GA	MILP	GA	MILP
Set 1	16	0.508	8	48	843.72	843.72	0.23	0.05
	32	0.254	16	96	852.05	852.84	2.26	0.06
	48	0.169	24	144	852.87	852.96	4.62	0.08
	64	0.127	32	192	851.28	852.24	10.1	0.09
	128	0.0635	64	384	814.26	853.17	>33.2	0.12
	256	0.0318	128	768	615.49	855.04	>113	0.2
	512	0.0159	256	1536	442.21	854.14	>195	0.33
Set 2	16	0.508	8	112	881.60	881.60	0.46	0.06
	32	0.254	16	224	886.92	887.07	3.32	0.09
	48	0.169	24	336	888.97	889.16	6.63	0.12
	64	0.127	32	448	884.56	889.14	15.3	0.17
	128	0.0635	64	896	857.85	889.17	>39.1	0.21
	256	0.0318	128	1792	680.21	893.38	>147	0.54
	512	0.0159	256	3584	569.9	893.38	>220	0.98

A study is performed to compare the performance of the MILP solver to that of GA for various sizes of design spaces. The number of plies and orientation sets are changed to

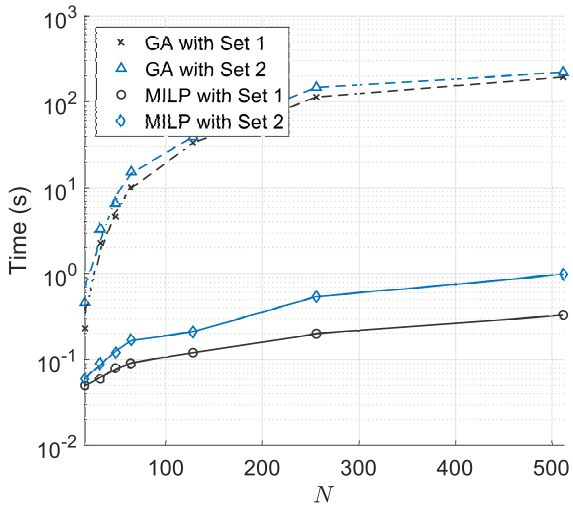

Figure 3.2: Performance scaling comparison between GA and MILP for buckling load maximization of hybrid laminates with a minimum 50% GFRP plies, $N_x = N_y = 1$N/mm, $a/b = 2$.

observe the wall clock time of the solvers. The ply thickness is changed with the number of plies to keep the total thickness constant. The minimum number of GFRP plies is fixed to 50%. From Table 3.5, the MILP solver can optimize hybrid laminate problems with a large number of plies and orientation set size within a second. The GA, due to the presence of a large number of local minima struggles to obtain a global optimum as the number of plies is increased. Additionally, the GA algorithm parameters like the population size and the number of generations are adjusted for each run to get the best possible output. Even with more than 100 runs using different algorithm parameter values, GA converges prematurely to an optimum that is far below the global value for $N > 64$. The collective time involved in rerunning GA with different parameter values is several orders of magnitude high compared to MILP. The performance scaling is represented in Fig. 3.2.

3.5.2 Weight Minimization using Distinct Ply Thicknesses

Initially, thickness optimization is performed using only STLO level 2 for different predetermined layups to analyze the performance of reformulation techniques in solving cubically constrained non-hybrid laminate optimization problems using MILP. The results for the same are presented in Table 3.6 for different design load values N_0. The thickness set $\mathrm{T} \in \{0.003\text{in.}, 0.007\text{in.}\}$ is defined in steps of 0.0005 in. which corresponds to $\mathrm{T} \in \{0.0762\text{mm}, 0.1778\text{mm}\}$ in steps of 0.0127mm. Three different layups used for this study are as follows:

1. Layup 1: $[0/90/\pm 45/90/0]_S$
2. Layup 2: $[0_2/(\pm 45)_3/90_4/\pm 45/90_2]_S$
3. Layup 3: $[0/\pm 15/\pm 30/\pm 45/\pm 60/\pm 75/90]_S$

The first two layups used for optimization have the same set of unique angles but a different number of plies and stacking sequences, whereas the third layup has a higher number of unique angles. The column showing the number of variables and constraints includes auxiliary (additional) variables and constraints as well. Since up to 5 half sine waves are used in both in-plane directions resulting in 25 buckling constraints, the total number of additional constraints is increased significantly. The buckling load factor of the optimal design is calculated analytically using Classical Lamination Theory (CLT) for verification.

By comparing the first two layups, it can be observed that both have three unique orientations, which results in the same number of design variables and constraints. Reformulating with Chang's model yields a higher number of constraints, and as a result, the solver takes more computational time to arrive at an optimal solution. Reformulating using Adam-Forrester's model yields an optimum solution in $\approx 1/6^{th}$ of the time required for Chang's

Table 3.6: Thickness optimization results using STLO level 2 - Non-hybrid laminates, $N_x = N_y = N_0$, $a/b = 2$

Layup		1	2	3
Unique orientations		$[0, 45, 90]$	$[0, 45, 90]$	$[0, 30, 45, 60, 90]$
Design load N_0 (N/mm)		10	150	10
Chang's model	No. of Vars	2727	2727	21420
	No. of Constraints	14878	14878	126030
	time (s)	13.89	4.82	799.3
Adam-Forrester's model	Vars	2727	2727	21420
	Constraints	8128	8128	64155
	time (s)	1.52	0.937	130.85
Optimal volume (10^5 mm^3)		1.343	3.245	1.442
Optimal thickness for every orientation (mm)		$[0.165, 0.178, 0.178]$	$[0.089, 0.178, 0.152]$	$[0.076, 0.076, 0.089, 0.14, 0.178]$
Buckling load factor		1.001	1.001	1.015

model. Even with the same number of variables and constraints, optimization using the second layup is much faster than the first layup (0.937s vs. 1.52s). This can be attributed to the nature of the MIP solver, as the ordering of variables and constraints can impact the solver's efficiency. With the addition of two unique orientations in the third layup, the complexity increases significantly, especially for Chang's model, for which the number of constraints is almost double that of Adam-Forrester's model. The time taken for the optimizer is largely increased as well. From the overall thickness optimization results, Adam-Forrester's model is relatively more efficient, so it is used for the complete mass and cost minimization of laminates using STLO.

For weight minimization of hybrid laminates, the design loads obtained from buckling load maximization are chosen with constraints on the minimum number of GFRP plies. Here, the thickness set $\mathrm{T} \in \{0.004\text{in.}, 0.006\text{in.}\}$ is defined in steps of 0.0005 in. which corresponds to $\mathrm{T} \in \{0.1016\text{mm}, 0.1524\text{mm}\}$ in steps of 0.0127mm. The mass of the laminate is computed as $W = ab\sum_{k=1}^{N}(t_k\rho_k)$. To study the trade-off between mass and cost, a cost value is an

output with the cost function $C = ab\sum_{k=1}^{N}(t_k\rho_k\alpha_k)$. The optimization results obtained using distinct ply thicknesses are compared with those obtained for uniform ply thicknesses. A performance factor δ is introduced to see the benefit of using distinct ply thicknesses. The factor is related to the cost-to-weight ratio obtained using both methods and is computed as given in Eqn. (3.33). A positive value of δ indicates that both functions are either increasing or decreasing, whereas a negative value of δ indicates a trade-off where one is increasing and the other is decreasing. In weight minimization, $-1 \geq \delta \geq 1$ is favorable as the reduction in weight is more than the increase in cost, whereas, in cost minimization, $\delta \leq -1$ or $\delta \geq 1$ is favorable as it shows that the decrease in cost is higher than the increase in weight.

$$\delta = \frac{\text{\% Change in cost from uniform ply thickness to distinct ply thickness}}{\text{\% Change in weight from uniform ply thickness to distinct ply thickness}} \tag{3.33}$$

From Table 3.7, the minimum mass obtained using uniform ply thicknesses for the first four cases can be verified as the global optimum by comparing it with the results from Table 3.3. Using the STLO with distinct ply thicknesses reduces weight in all cases since the thickness of GFRP plies is reduced while that of CFRP is increased. This is observed from ply thickness values in Table 3.8 where the GFRP plies having orientations 45° and 90° have relatively lower thicknesses compared to their CFRP counterparts. This reduction in weight is only favorable in Cases 2 and 5 where $\delta = -0.75$ and 0.96, respectively, whereas $\delta < -1$ in other cases shows that there is a significant increase in cost. Case 5 is special as by using more orientation values, the optimizer can obtain a design with lower thickness with the distinct thickness formulation. Moreover, since all plies are made of CFRP, the cost is also reduced. This is an advantage of using different thicknesses for different plies. As α for CFRP is 8 times that of GFRP, a slight increase in CFRP material significantly increases the cost of the laminate.

Table 3.7: Weight optimization results of hybrid laminates with distinct thickness, $N_x = N_y = N_0$ N/mm, $a/b = 2$, $N = 64$.

Case	N_0	Θ	Minimum GFRP plies	Uniform thickness thickness		Distinct ply thickness		δ
				Mass (kg)	Cost	Mass (kg)	Cost	
1	940.66	Set 1	0	1.678	13.424	1.678	13.424	-
2	852.24	Set 1	32	1.783	7.656	1.754	7.751	-0.75
3	645.25	Set 1	48	1.835	4.771	1.776	5.302	-3.46
4	470.49	Set 1	56	1.862	3.330	1.832	3.580	-4.17
5	940.66	Set 2	0	1.678	13.424	1.656	13.256	0.96
6	852.24	Set 2	32	1.783	7.656	1.719	8.474	-3.05

Table 3.8: Optimal stacking sequence and thickness obtained using STLO for studies in Table 3.7.

Case	Optimal stacking sequence with distinct ply thickness
1	$\left[90_4^C/\pm 45^C/90_4^C/\pm 45^C/90_2^C/\pm 45^C/90_4^C/(\pm 45)_2^C/90_4^C/\pm 45^C/90_2^C\right]_S$
2	$\left[90_2^C/\pm 45^C/90_4^C/\pm 45^C/90_2^C/\pm 45^C/90_2^C/90_4^G/\pm 45^G/90_4^G/\pm 45^G/0_4^G\right]_S$
3	$\left[90_2^C/\pm 45^C/90_4^C/90_2^G/\pm 45^G/90_2^G/(\pm 45)_3^G/90_4^G/\pm 45^G/90_2^G/\pm 45^G\right]_S$
4	$\left[90_4^C/(\pm 45)_8^G/90_4^G/(\pm 45)_2^G/90_4^G\right]_S$
5	$\left[(\pm 75)_3^C/\pm 60^C/\pm 75^C/(\pm 60)_2^C/(\pm 75)_5^C/(\pm 60)_3^C/90_2^C\right]_S$
6	$\left[(\pm 75)_2^C/\pm 60^C/(\pm 75)_2^C/\pm 60^C/(\pm 75)_2^C/\pm 75^G/\pm 60^G/ \pm 75^G/\pm 60^G/(\pm 75)_2^G/(\pm 60)_2^G\right]_S$
	Ply thickness for every orientation (θ: t (mm))
1	$45^C : 0.127,\ 90^C : 0.127$
2	$45^C : 0.1397,\ 90^C : 0.1524,\ 0^G : 0.1016,\ 45^G : 0.1143,\ 90^G : 0.1016$
3	$45^C : 0.1524,\ 90^C : 0.1524,\ 45^G : 0.1143,\ 90^G : 0.1143$
4	$90^C : 0.1524,\ 45^G : 0.1143,\ 90^G : 0.1397$
5	$60^C : 0.127,\ 75^C : 0.127,\ 90^C : 0.1016$
6	$60^C : 0.127,\ 75^C : 0.1524,\ 60^G : 0.1016,\ 75^G : 0.1016$

3.5.3 Cost Minimization using Distinct Ply Thicknesses

The hybrid laminate optimization problem is again solved with the cost function C as the objective function instead of mass W. As opposed to previous studies, a constraint is put on the maximum number of GFRP plies instead of a minimum number of GFRP plies.

The results are presented in Tables 3.9 and 3.10 where the mass and cost values obtained using uniform ply thicknesses are the same as that obtained using weight minimization. Contrary to weight minimization, when the laminates are optimized using a distinct thickness formulation for cost, the optimizer tries to increase the thickness of GFRP plies and reduce the thickness of CFRP plies as expected. It is observed that all cases are favorable for cost optimization as the reduction in cost is significant compared to the increase in mass. Additionally, it is observed that using more orientations in case 6 with distinct ply thicknesses helps in obtaining better designs compared to Case 2 as the weight penalty is lower. Using distinct ply thicknesses increases the size of discrete objective function space (q vs. $n_u q +^{n_u} C_3$ for uniform and distinct cases, respectively). With the combination of ply thicknesses, an improvement in the laminate design can thus be found that is not possible with uniform ply thicknesses.

Table 3.9: Cost optimization results of hybrid laminates with distinct thickness, $N_x = N_y = N_0$ N/mm, $a/b = 2$, $N = 64$.

Case	N_0	Θ	Maximum GFRP plies	Uniform ply thickness		Distinct ply thickness		δ
				Mass (kg)	Cost	Mass (kg)	Cost	
1	940.66	Set 1	0	1.678	13.424	1.678	13.424	-
2	852.24	Set 1	32	1.783	7.656	1.846	6.836	-3.06
3	645.25	Set 1	48	1.835	4.771	1.928	4.278	-2.06
4	470.49	Set 1	56	1.862	3.33	1.96	3.136	-1.12
5	940.66	Set 2	0	1.678	13.424	1.656	13.256	0.96
6	852.24	Set 2	32	1.783	7.656	1.824	6.67	-5.6

Table 3.10: Optimal stacking sequence and thickness obtained using STLO for studies in Table 3.9.

Case	Optimal stacking sequence with distinct ply thickness
1	$\left[90_4^C/\pm 45^C/90_4^C/\pm 45^C/90_2^C/\pm 45^C/90_4^C/(\pm 45)_2^C/90_4^C/\pm 45^C/90_2^C\right]_S$
2	$\left[90_4^C/\pm 45^C/90_4^C/\pm 45^C/90_4^C/90_4^G/\pm 45^G/90_4^G/(\pm 45)_2^G/0_2^G\right]_S$
3	$\left[90_2^C/\pm 45^C/90_4^C/90_2^G/\pm 45^G/90_2^G/\pm 45^G/90_4^G/\pm 45^G/90_4^G/(\pm 45)_2^G/0_2^G\right]_S$
4	$\left[90_4^C/(\pm 45)_8^G/90_2^G/\pm 45^G/90_2^G/\pm 45^G/90_4^G\right]_S$
5	$\left[(\pm 75)_3^C/\pm 60^C/\pm 75^C/(\pm 60)_2^C/(\pm 75)_5^C/(\pm 60)_3^C/90_2^C\right]_S$
6	$\left[\pm 60^C/(\pm 75)_5^C/\pm 60^C/\pm 75^C/(\pm 75)_4^G/(\pm 60)_3^G/\pm 45^G\right]_S$
	Ply thickness for every orientation (θ: t (mm))
1	$45^C : 0.127,\ 90^C : 0.127$
2	$45^C : 0.127,\ 90^C : 0.1016,\ 0^G : 0.1524,\ 45^G : 0.1524,\ 90^G : 0.1524$
3	$45^C : 0.1016,\ 90^C : 0.1016,\ 0^G : 0.1016,\ 45^G : 0.1397,\ 90^G : 0.1524$
4	$90^C : 0.1016,\ 45^G : 0.1524,\ 90^G : 0.1016$
5	$60^C : 0.127,\ 75^C : 0.127,\ 90^C : 0.1016$
6	$60^C : 0.1143,\ 75^C : 0.1016,\ 45^G : 0.1524,\ 60^G : 0.1524,\ 75^G : 0.1524$

Chapter 4

Application of Integer Programming in the Optimization of Composite Structures

With the requirement of explicit expressions for integer programming solvers, the formulations derived in Chapters II and III cannot be directly implemented to optimize complex structures with the finite element method. In this chapter, a two-step procedure is devised for the same as in [81, 82, 83]. In step 1, the lamination parameters are assumed as continuous design variables from which the composite laminates are analyzed as homogenized shells. This can be done using finite element solvers. The lamination parameter space is proven to be convex and greatly reduces the optimization complexity. Once the optimal lamination parameter values are found, the stacking sequence is retrieved from the explicit relationship between lamination parameters and ply fiber orientations with the help of MIP.

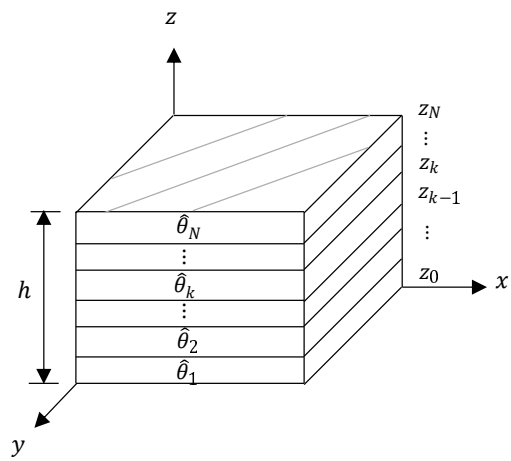

Figure 4.1: General laminate stacking.

4.1 Lamination parameters and Stiffness of General Unidirectional Laminates

For general unidirectional lamina stacks shown in Fig. 4.1, the lamination parameters given in Eqn. (2.3) are normalized with respect to laminate thickness h with $\bar{z} = z/h$ and rewritten here as,

$$\begin{aligned} v_{[1A,2A,3A,4A]} &= \sum_{k=1}^{N} \left\{ (\bar{z}_k - \bar{z}_{k-1}) \left[\cos 2\hat{\theta}_k, \sin 2\hat{\theta}_k, \cos 4\hat{\theta}_k, \sin 4\hat{\theta}_k \right] \right\} \\ v_{[1B,2B,3B,4B]} &= 2 \sum_{k=1}^{N} \left\{ \left(\bar{z}_k^2 - \bar{z}_{k-1}^2 \right) \left[\cos 2\hat{\theta}_k, \sin 2\hat{\theta}_k, \cos 4\hat{\theta}_k, \sin 4\hat{\theta}_k \right] \right\} \\ v_{[1D,2D,3D,4D]} &= 4 \sum_{k=1}^{N} \left\{ \left(\bar{z}_k^3 - \bar{z}_{k-1}^3 \right) \left[\cos 2\hat{\theta}_k, \sin 2\hat{\theta}_k, \cos 4\hat{\theta}_k, \sin 4\hat{\theta}_k \right] \right\} \end{aligned} \tag{4.1}$$

Each of the lamination parameters v in Eqn. 4.1 is bounded between -1 and 1. The in-plane/extensional, coupling, out-of-plane/bending, and shear stiffness components A_{ij}, B_{ij}, D_{ij} $(i, j = 1, 2, 6)$ and $A_{ij}(i, j = 4, 5)$ respectively are linear functions of lamination parameters and are given in Eqn. (4.2a) to Eqn. (4.2d).

In-plane stiffness:

$$\begin{Bmatrix} A_{11} \\ A_{22} \\ A_{12} \\ A_{66} \\ A_{16} \\ A_{26} \end{Bmatrix} = h \begin{bmatrix} 1 & v_{1A} & v_{3A} & 0 & 0 \\ 1 & -v_{1A} & v_{3A} & 0 & 0 \\ 0 & 0 & -v_{3A} & 1 & 0 \\ 0 & 0 & -v_{3A} & 0 & 1 \\ 0 & v_{2A}/2 & v_{4A} & 0 & 0 \\ 0 & v_{2A}/2 & -v_{4A} & 0 & 0 \end{bmatrix} \begin{Bmatrix} U_1 \\ U_2 \\ U_3 \\ U_4 \\ U_5 \end{Bmatrix} \tag{4.2a}$$

Bending-extension coupling stiffness:

$$\begin{Bmatrix} B_{11} \\ B_{22} \\ B_{12} \\ B_{66} \\ B_{16} \\ B_{26} \end{Bmatrix} = \frac{h^2}{4} \begin{bmatrix} 1 & v_{1B} & v_{3B} & 0 & 0 \\ 1 & -v_{1B} & v_{3B} & 0 & 0 \\ 0 & 0 & -v_{3B} & 1 & 0 \\ 0 & 0 & -v_{3B} & 0 & 1 \\ 0 & v_{2B}/2 & v_{4B} & 0 & 0 \\ 0 & v_{2B}/2 & -v_{4B} & 0 & 0 \end{bmatrix} \begin{Bmatrix} U_1 \\ U_2 \\ U_3 \\ U_4 \\ U_5 \end{Bmatrix} \tag{4.2b}$$

Out-of-plane stiffness:

$$\begin{Bmatrix} D_{11} \\ D_{22} \\ D_{12} \\ D_{66} \\ D_{16} \\ D_{26} \end{Bmatrix} = \frac{h^3}{12} \begin{bmatrix} 1 & v_{1D} & v_{3D} & 0 & 0 \\ 1 & -v_{1D} & v_{3D} & 0 & 0 \\ 0 & 0 & -v_{3D} & 1 & 0 \\ 0 & 0 & -v_{3D} & 0 & 1 \\ 0 & v_{2D}/2 & v_{4D} & 0 & 0 \\ 0 & v_{2D}/2 & -v_{4D} & 0 & 0 \end{bmatrix} \begin{Bmatrix} U_1 \\ U_2 \\ U_3 \\ U_4 \\ U_5 \end{Bmatrix} \tag{4.2c}$$

Shear stiffness:

$$\begin{Bmatrix} A_{44} \\ A_{55} \\ A_{45} \end{Bmatrix} = \frac{5h}{6} \begin{bmatrix} 1 & v_{1A} \\ 1 & -v_{1A} \\ 0 & -v_{2A} \end{bmatrix} \begin{Bmatrix} U_6 \\ U_7 \end{Bmatrix} \tag{4.2d}$$

where $U_i (i = 1, 2, \ldots, 5)$ are given in Eqn. (2.2) and U_6, U_7 are calculated as

$$\begin{Bmatrix} U_6 \\ U_7 \end{Bmatrix} = \begin{bmatrix} 1/2 & 1/2 \\ 1/2 & -1/2 \end{bmatrix} \begin{Bmatrix} G_{23} \\ G_{13} \end{Bmatrix} \tag{4.3}$$

4.1.1 Feasible Regions in Lamination Parameter Space

Since the lamination parameters are functionals of layup function $\hat{\theta}(z)$, they are not independent and must be restricted to a set of feasible regions for the design to be valid in optimization step 1. Relationships between different lamination parameters that govern the feasible design space in step 1 are given in the literature [83, 84, 85] and presented in Eqn. (4.4) and Eqn. (4.5) with $i = 1, 2, 3, 4$ and $j = A, D$. These inequalities constitute a set of 23 non-linear constraints that provide a necessary representation of feasible design space. The constraints defined in Eqn. (4.4) relate either in-plane or out-of-plane stiffnesses to each other and are valid for symmetric laminates, i.e., $v_{iB} = 0$.

$$v_{1j}^2 + v_{2j}^2 \leq 1 \tag{4.4a}$$

$$2v_{1j}^2 - v_{3j} \leq 1 \tag{4.4b}$$

$$2(1 + v_{3j})v_{2j}^2 - 4v_{1j}v_{2j}v_{4j} + 4v_{4j}^2 - \left(v_{3j} - 2v_{1j}^2 + 1\right)(1 - v_{3j}) \leq 0 \tag{4.4c}$$

The constraints defined in Eqn. (4.5) relate in-plane stiffness to out-of-plane and coupling terms.

$$\frac{1}{4}\left(v_{iA}+1\right)^3-1 \leq v_{iD} \leq \frac{1}{4}\left(v_{iA}+1\right)^3-1 \tag{4.5a}$$

$$4\left(v_{iA}+1\right)\left(v_{iD}+1\right) \geq \left(v_{iA}+1\right)^4 \tag{4.5b}$$

$$4\left(v_{iA}-1\right)\left(v_{iD}-1\right) \geq \left(v_{iA}-1\right)^4 \tag{4.5c}$$

$$5\left(v_{1A}-v_{1D}\right)^2-2\left(1+v_{3A}-2v_{1A}^2\right) \leq 0 \tag{4.5d}$$

While the inequalities defined in Eqn. (4.4) and Eqn. (4.5) are crucial for lamination parameter optimization, their set is incomplete for relationships of coupled lamination parameters v_{iB}. A symmetric and balanced laminate is used for most practical designs, which makes $v_{2A}, v_{4A} = 0$, along with coupling terms. The stiffness values for D_{16} and D_{26} are very small compared to other elements in D and v_{2D} and v_{4D} can be set to 0. Thus, in this study for lamination parameter optimization in step 1, only four lamination parameters (v_{1A}, v_{3A}, v_{1D} and v_{3D}) are considered design variables. After substituting other lamination parameters as 0 in Eqn. (4.4) and Eqn. (4.5), the design constraint set reduces to 15 inequalities. The optimization in step 1 can be further simplified using linear scaling maps.

4.1.2 Lamination Parameter Mapping

Instead of directly using the inequalities defined in the previous section as constraints, a variable transformation can be used that maps the newly defined variables to feasible lamination parameters [84]. Using Eqn. (4.4) and Eqn. (4.5), every point in the computational space can be mapped to a feasible value of lamination parameters. Let β_{ij} be a variable in computational space with bounds -1 and 1 that maps to lamination parameter v_{ij}. The

linear scaling equation is given as,

$$v_{ij} = \frac{1}{2}\left(L^u_{ij} + L^l_{ij}\right) + \frac{1}{2}\left(L^u_{ij} - L^l_{ij}\right)\beta_{ij}, \quad i = 1,3 \text{ and } j = A, D \tag{4.6}$$

The upper and lower bounds L^u_{ij} and L^l_{ij} are obtained step-wise by assuming one of the $\beta_{ij} = v_{ij}$ and solved for unknown v in terms of known v_{ij} successively using feasible region inequalities.

The lamination parameter v_{3A} is chosen as the starting point as in [84], which makes $v_{3A} = \beta_{3A}$. By solving Eqn. (4.4a) in terms of v_{1A}, the lower and upper bounds are found as

$$-\sqrt{0.5\left(v^2_{3A}+1\right)} \leq v_{1A} \leq \sqrt{0.5\left(v^2_{3A}+1\right)} \tag{4.7}$$

From Eqn. (4.7), $L^l_{1A} = -\sqrt{0.5\left(v^2_{3A}+1\right)}$ and $L^u_{1A} = \sqrt{0.5\left(v^2_{3A}+1\right)}$. Substituting it in Eqn. (4.6) gives,

$$v_{1A} = \beta_{1A}\sqrt{0.5\left(v^2_{3A}+1\right)} \tag{4.8}$$

After evaluating v_{1A} from Eqn. (4.8), Eqn. (4.5a) and Eqn. (4.5d) can be solved for v_{1D} in terms of v_{1A} and v_{3A} to give four inequalities for v_{1D} as shown in Eqn. (4.9).

$$\begin{gathered}\frac{1}{4}\left(v_{1A}+1\right)^3 - 1 \leq v_{1d} \leq \frac{1}{4}\left(v_{1A}-1\right)^3 + 1 \\ v_{1A} - \sqrt{\frac{2}{5}}\sqrt{1 - 2v^2_{1A} + v_{3A}} \leq v_{1d} \leq v_{1A} + \sqrt{\frac{2}{5}}\sqrt{1 - 2v^2_{1A} + v_{3A}}\end{gathered} \tag{4.9}$$

with

$$\begin{aligned} L^l_{1D} &= \max\left\{\frac{1}{4}\left(v_{1A}+1\right)^3 - 1, \quad v_{1A} - \sqrt{\frac{2}{5}}\sqrt{1 - 2v^2_{1A} + v_{3A}}\right\} \\ L^u_{1D} &= \min\left\{\frac{1}{4}\left(v_{1A}-1\right)^3 + 1, \quad v_{1A} + \sqrt{\frac{2}{5}}\sqrt{1 - 2v^2_{1A} + v_{3A}}\right\} \end{aligned} \tag{4.10}$$

The bounds in Eqn. (4.10) are substituted in Eqn. (4.6) to get the map for v_{1D}.

Similarly, inequalities in Eqn. (4.4b) and Eqns. (4.5a,b and c) are solved for bounds on v_{3D}. By removing the redundancies i.e., Eqn. (4.5b) and Eqn. (4.5c), the four remaining inequalities for v_{3D} are given in Eqn. (4.11).

$$\begin{aligned} 2v_{1D}^2 - 1 &\leq 1 \\ \frac{1}{4}\left(v_{3A}+1\right)^3 - 1 &\leq \frac{1}{4}\left(v_{3A}-1\right)^3 + 1 \end{aligned} \tag{4.11}$$

with

$$\begin{aligned} L_{3D}^l &= \max\left\{\frac{1}{4}\left(v_{3A}+1\right)^3 - 1, \quad 2v_{1D}^2 - 1\right\} \\ L_{3D}^u &= \min\left\{\frac{1}{4}\left(v_{3A}-1\right)^3 + 1, \quad 1\right\} \end{aligned} \tag{4.12}$$

The map for v_{3D} is obtained by substituting bounds from Eqn. (4.12) in Eqn. (4.6). The bounds for four lamination parameters used in this work are given in Table 4.1.

Table 4.1: Lamination parameter bounds for linear scaling maps.

v_{ij}	L_{ij}^l	L_{ij}^u
v_{1A}	$-\sqrt{0.5\left(v_{3A}^2+1\right)}$	$\sqrt{0.5\left(v_{3A}^2+1\right)}$
v_{3A}	-1	1
v_{1D}	$\max\{\frac{1}{4}\left(v_{1A}+1\right)^3 - 1,$ $-\sqrt{\frac{2}{5}}\sqrt{1-2v_{1A}^2+v_{3A}}\}$	$\min\{\frac{1}{4}\left(v_{1A}-1\right)^3 + 1,$ $v_{1A}+\sqrt{\frac{2}{5}}\sqrt{1-2v_{1A}^2+v_{3A}}\}$
v_{3D}	$\max\left\{\frac{1}{4}\left(v_{3A}+1\right)^3 - 1, \quad 2v_{1D}^2 - 1\right\}$	$\min\left\{\frac{1}{4}\left(v_{3A}-1\right)^3 + 1, \quad 1\right\}$

4.1.3 Mapping verification

To verify the mapping bounds stated in Table 4.1, 1000 points between -1 and 1 are randomly generated for $\beta_{1A}, \beta_{3A}, \beta_{1D}$ and β_{3D}. The lamination parameter space obtained with the derived maps is shown in Fig 4.2 and 4.3. Figure 4.2 shows the mapping of computational space to lamination parameter space for the same type of lamination parameters (either in-plane or out-of-plane), whereas Fig 4.3 shows the mapping for the relationship between in-plane and out-of-plane lamination parameters. The solid lines show the constraints for lamination parameter design space. The constraints appear to be satisfied at all points considered and, thus, successfully verify the linear scaling maps. The variables $\beta_{1A}, \beta_{3A}, \beta_{1D}$ and β_{3D} are used as design variables in the optimization step 1 to find optimal extensional and bending stiffnesses.

4.2 Laminate Optimization Problem Formulation

A balanced symmetric composite panel of arbitrary shape subjected to arbitrary loading is shown in Fig 4.4. The ply thickness is fixed to t_k, and the number of plies N is allowed to vary such that $2 \leq N \leq N_{max}$. Let the normalized lamination parameter vector $\mathbf{v} = [v_{1A}, v_{3A}, v_{1D}, v_{3D}]^T$ and the computational space variable vector $\boldsymbol{\beta} = [\beta_{1A}, \beta_{3A}, \beta_{1D}, \beta_{3D}]^T$. The optimization problem for lamination parameter optimization (step 1) can be written as

Step 1: Lamination parameter design with FEM.

$$\begin{array}{ll} \textbf{Minimize:} & f(h, \mathbf{v}(\boldsymbol{\beta})) \\ \textbf{By varying:} & h, \boldsymbol{\beta} \\ \textbf{Subject to:} & g(h, \mathbf{v}(\boldsymbol{\beta})) \leq 0 \\ & -1 \leq \boldsymbol{\beta} \leq 1 \end{array}$$

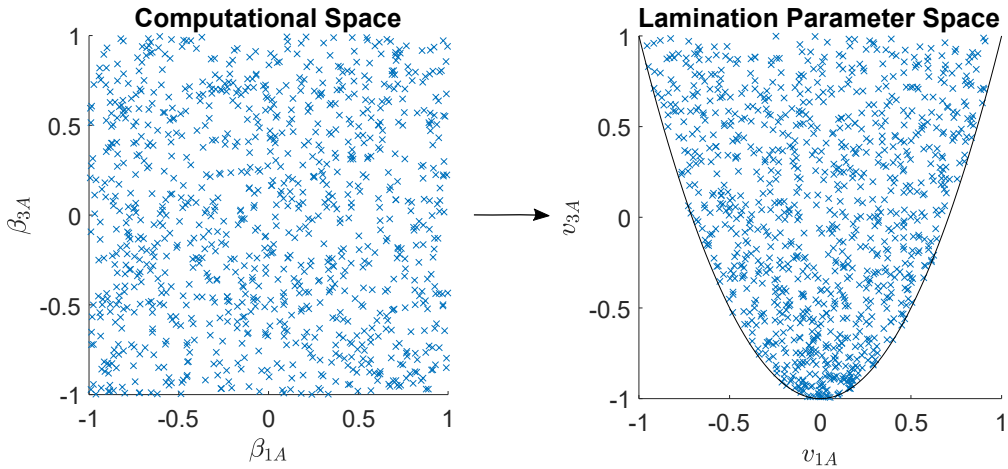

(a) Lamination parameter mapping verification for relationship between v_{1A} and v_{3A}.

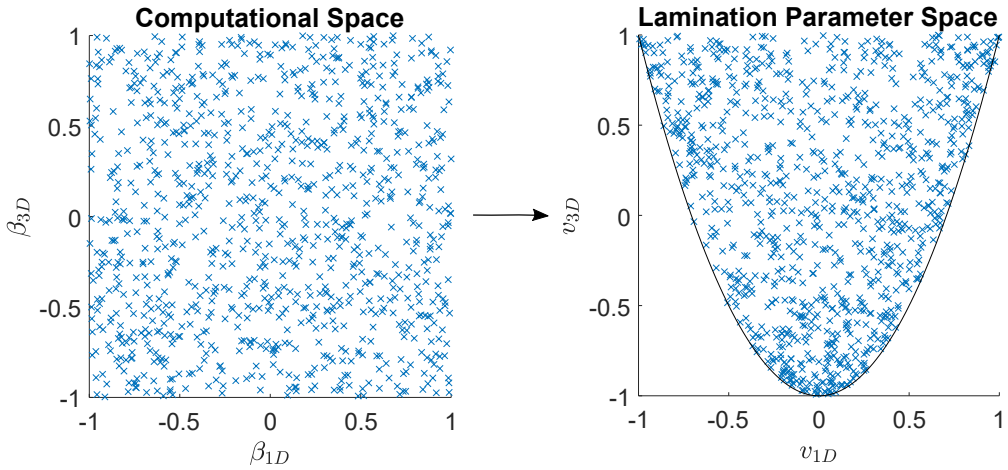

(b) Lamination parameter mapping verification for relationship between v_{1A} and v_{3A}.

Figure 4.2: Mapping verification for the relationship between same-type lamination parameters

Suppose the fiber orientations of each ply can be chosen from set $\Theta \in \{\theta_1, \theta_2, \ldots, \theta_p\}$, the stacking sequence and the number of plies can be retrieved from optimal lamination parameters $\mathbf{v}^*(\boldsymbol{\beta}^*)$ by using the SLO2 formulation as

Here, $\hat{A}_{mn}$ and $\hat{D}_{mn}$ are extensional and bending stiffnesses obtained from Eqn. (2.9) using lamination parameter expressions in binary variables $\mathbf{x}$. In step 2, the number of plies is minimized such that the laminate stiffnesses obtained using integer programming are greater

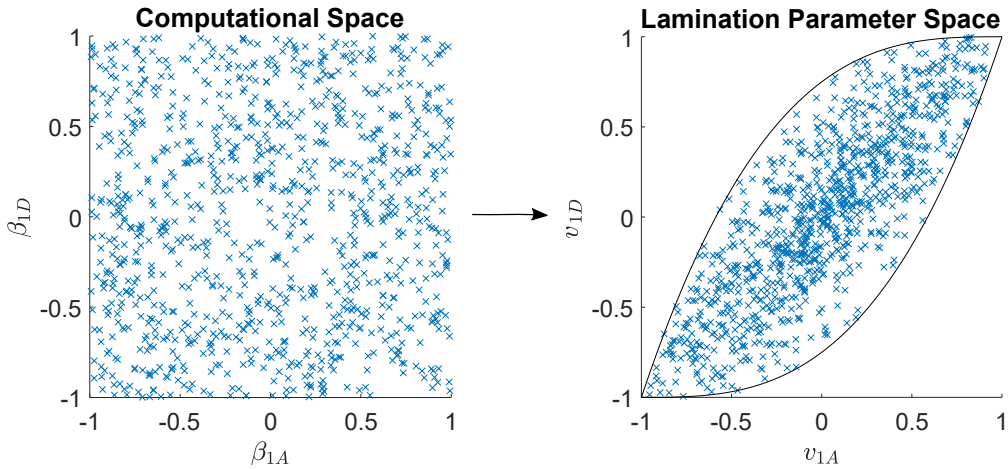

(a) Lamination parameter mapping verification for relationship between v_{1A} and v_{1D}.

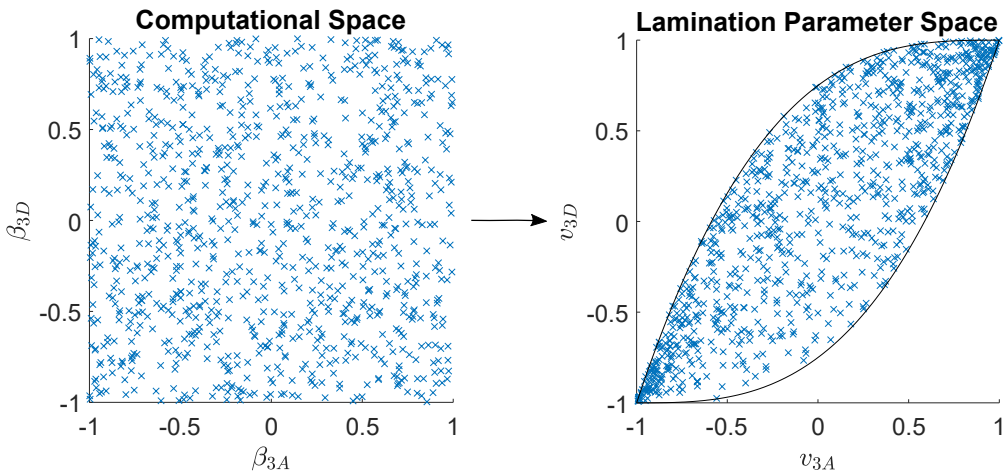

(b) Lamination parameter mapping verification for relationship between v_{3A} and v_{3D}.

Figure 4.3: Mapping verification for the relationship between different-type lamination parameters

than or equal to that obtained from lamination parameter optimization.

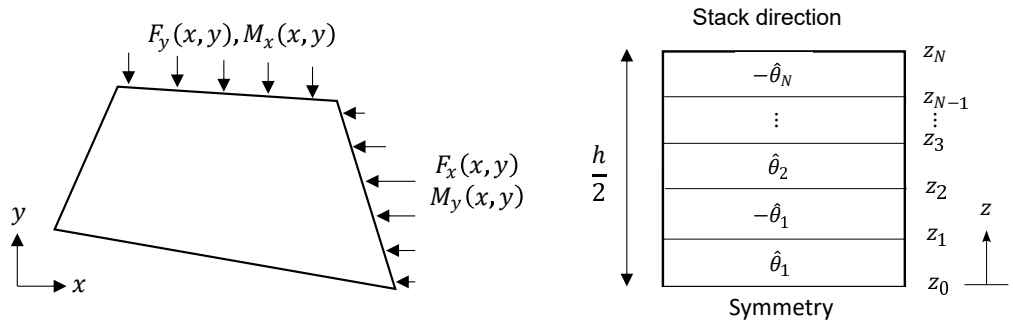

Figure 4.4: Schematic of an arbitrary composite panel.

Step 2: Stiffness matching with integer linear programming.

$$
\begin{array}{lll}
\textbf{Minimize:} & W(\mathbf{x}) = \sum_{k=1}^{N_{max}} \sum_{l=1}^{p} x_{lk} & \\
\textbf{By varying:} & \mathbf{x} & \\
\textbf{Subject to:} & \sum_{l=1}^{p} x_{lk} \leq 1 & k = 1, \ldots, N_{max} \\
 & \sum_{i=k}^{k+3} x_{li} \leq 4 & k = 1, \ldots, N_{max} - 4 \\
 & x_{l_1,k} - x_{l_2,k+1} = 0 & \forall l_1, l_2 \in \{1, \ldots, p\} \\
 & & \theta_{l_1} = -\theta_{l_2} \\
 & & k = 1, \ldots, N_{max} \\
 & \sum_{l=1}^{p} (x_{l,k+1} - x_{lk}) \leq 0 & k = 1, \ldots, N_{max} - 1 \\
 & \hat{A}_{mn}\left(\hat{\mathbf{v}}(\mathbf{x})\right) \geq A_{mn}\left(\mathbf{v}^*\right) & m, n \in \{1, 2, 4, 5, 6\} \\
 & \hat{D}_{mn}\left(\hat{\mathbf{v}}(\mathbf{x})\right) \geq D_{mn}\left(\mathbf{v}^*\right) & m, n \in \{1, 2, 6\} \\
 & \mathbf{x} \in \{0, 1\}^p &
\end{array}
$$

4.3 Laminate Optimization with Lamination Parameters

A simply supported rectangular laminate model is used as in chapter II. The model is meshed with 400 CQUAD4 elements as shown in Fig 4.5. A uniform biaxial in-plane compressive load $N_{xx} = 9999.14$ lb/in. and $N_{yy} = 0.5N_{xx}$ is applied along the edges. The material card MAT2 is used to define the extensional, bending, and shear stiffness of the laminate. The material cards are used with a PSHELL property card to define a homogenous shell layer.

The resulting equivalent shell model is solved for the buckling load factor in Nastran.

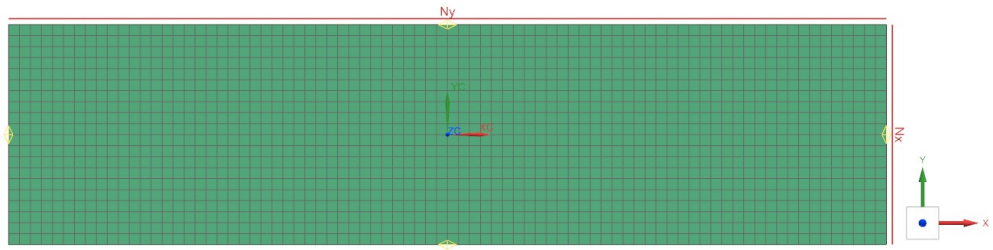

Figure 4.5: FE model of a rectangular composite laminate.

The forward or the direct approach is solved using GA and leads to a minimum number of plies $N = 26$ with $t_k = 0.005$ in. for $\Theta \in \{0, 45, 90\}$. Since the lamination parameter space is convex, a gradient-based optimizer can be used to find optimal lamination parameter values quickly. Even though this is the case, gradient information is not always available when using commercial software to analyze complex structures. Thus, PSO is used for lamination parameter optimization (step 1) in this work. Three runs are performed with different starting points to get a converged solution for lamination parameters to minimize the laminate thickness h so that the buckling constraints are satisfied.

Step 1 yields an optimal thickness value of $h = 0.2355$ in. (Fig 4.6), which is less than that obtained from the direct approach (0.26 in.). The design obtained in step 1 is an ideal design where continuous design space for lamination parameters is assumed, which in turn means a continuous design space for Θ. To match the stiffnesses obtained in step 1, a parametric study is performed in step 2 by varying the set size of Θ, ply thickness t_k, and the maximum number of plies N_{max}. The results obtained in step 2 are presented in Table 4.2. For $\Theta \in \{0 : 45 : 90\}$ and $t_k = 0.005$ in., the optimal thickness retrieved is 0.26 in. for the optimal number of plies $N_{opt} = 26$. It matches with that obtained from the direct approach.

If the resolution of Θ is increased to every 15 degrees, the optimization can better match

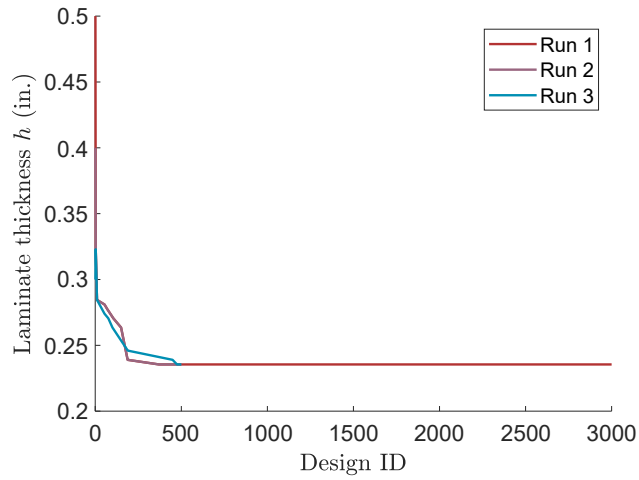

Figure 4.6: Thickness convergence in lamination parameter optimization (step 1).

Table 4.2: Optimal results for stacking sequence retrieval optimization in step 2.

Θ	t_k (in.)	N_{max}	No. of variables	N_{opt}	h_{opt} (in.)	λ_{opt}	Time (s)
$\{0:45:90\}$	0.005	100	150	26	0.26	1.256	0.13
$\{0:45:90\}$	0.0025	200	300	52	0.26	1.256	0.15
$\{0:45:90\}$	0.001	400	600	130	0.26	1.255	0.19
$\{0:15:90\}$	0.005	100	350	24	0.24	1.052	0.15
$\{0:15:90\}$	0.0025	200	700	48	0.24	1.047	0.18
$\{0:15:90\}$	0.001	400	1400	120	0.24	1.040	0.3
$\{0:5:90\}$	0.005	100	950	24	0.24	1.042	0.28
$\{0:5:90\}$	0.0025	200	1900	48	0.24	1.039	0.37
$\{0:5:90\}$	0.001	400	3800	120	0.24	1.040	0.95

the stiffnesses from step 1, and the optimal number of plies reduces to 24. It results in a laminate thickness of 0.24 in., close to the ideal laminate thickness (0.2355 in.). Increasing the angle resolution further sees no improvement in the thickness. Reducing the ply thickness and increasing the number of plies also does not affect the results, as the buckling load is primarily a function of total laminate thickness. For all cases in Step 2, the stacking sequence retrieval is done within a second, improving the performance significantly over heuristic solvers. Additionally, the optimization in Step 1 is not required to be performed again for every change in ply thickness or orientation resolution. This leads to significant savings in computational effort while doing parametric design studies.

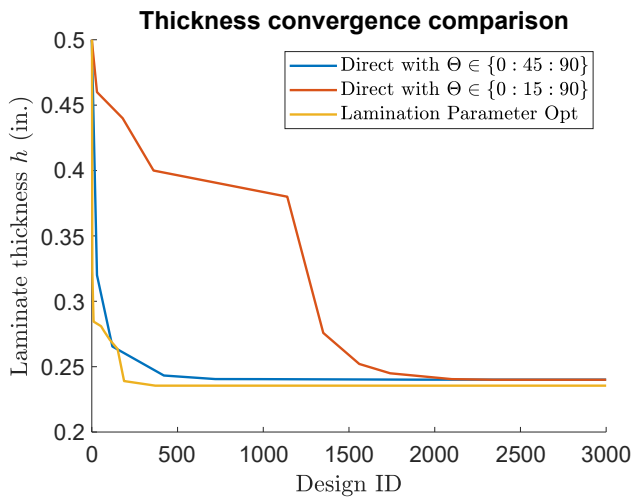

Figure 4.7: Thickness convergence comparison.

A comparison between the performance of lamination parameter optimization and direct optimization with the Genetic Algorithm is shown in Fig 4.7. Here, the direct optimization is run > 20 times with two different resolutions of Θ. Similar to that observed in the results of closed-form solutions in previous chapters, increasing the fiber angle resolution from a 45° interval to a 15° interval in the direct method increases the computational cost 3 times until convergence. The plot highlights the savings in computational effort obtained from using lamination parameters and MIP, especially as the number of design variables increases. This approach is used to efficiently solve a complex spacecraft structural optimization problem in Chapter VI.

Chapter 5

Multidisciplinary Structural Analysis and Design Optimization (MSADO) Framework

The lamination parameter optimization combined with Mixed Integer Programming provides a means to significantly reduce the number of design evaluations in composite structure optimization. It tackles the first of the two main objectives defined in this research. The current chapter targets the second objective to improve multidisciplinary analysis performance. It aims at developing a Multidisciplinary Structural Analysis and Design Optimization Framework (MSADO) for spacecraft structural design.

The primary disciplines that one must account for in the design of spacecraft structures are mechanical, acoustics, and thermal. While acoustics and thermal are part of the mechanical domain, they are separated here based on the load classification. In this study, the structure is optimized/sized for launch vehicles and in-orbit loads. Based on the functionality and project requirements, the Siemens NX [86] pre/post processor package coupled with the NASTRAN [87] solver is the structural analysis software of choice for this study. NX Space Systems Thermal is the solver used for orbital heat transfer analysis and temperature mapping. Simcenter HEEDS [71] is used to integrate different disciplines and governs the overall MSADO process.

In the framework, the analyses for mechanical loads include linear static, buckling, normal modes, sine vibration, random vibration, and shock vibration. The analysis for acoustic loads includes vibroacoustics. The structural response due to temperature variations is included by a non-linear transient heat-transfer analysis followed by linear thermal static and buckling analyses. The MSADO framework is used to optimize a spacecraft's primary structure that is representative of the actual satellite for weight minimization.

5.1 MSADO Framework Description

In the MSADO framework, each block in the design structure matrix represents an analysis of the MSADO process as shown in Fig 5.1. The numbers on each block show the solution sequence of each sub-process or analysis. The same numbers on different blocks indicate that the analyses can run independently in parallel. For example, linear static and heat transfer analysis are independent analyses so that they can be run in parallel for computational efficiency. For small FEM models, the benefit of running a single analysis on multiple cores is seldom advantageous. In such cases, either multiple analyses or multiple designs can be run in parallel to reduce the overall computational cost significantly. On a cluster or a multi-core machine, the cores are evenly distributed for each analysis run in parallel.

In large FEM models with several hundred thousand degrees of freedom, most of the time is spent solving linear systems of equations. Here, GPU acceleration significantly increases the solver's performance. SOL 101 (Linear static), 103 (Normal modes), and 105 (Linear buckling) can benefit from GPU parallelization. SOL 108 (direct frequency response) with a large number of input frequencies also benefits significantly from CPU + GPU processing. Thus, the framework is built to utilize available computer resources optimally. In the current configuration, each of the structural analyses is run on a single core sequentially,

with multiple designs running in parallel. The flow process of MSADO is shown in Fig 5.4. Every design iteration utilizes 20 cores of the available 24 cores of the Intel Xeon W2265 processor. The remaining 4 cores are reserved for system operations. A brief description of loading environments, along with a description of analyses used to simulate them, is given next.

5.1.1 Input and Pre-Processing

Simcenter HEEDS is a design space exploration tool that interfaces with other FEM analysis software. It is used as the primary controller for the MSADO process. The design variables are mapped from the parameters defined in the input file. The objective function and constraints are defined from the list of structural response outputs from different analyses. Heeds updates the input decks after each iteration with new design variable data from the optimizer. The input Python file contains design variable information and preprocessing calculations to compute mass properties, panel stacking properties and effective thermal conductivities. pyNastran is used to write BDF files for different structural properties such as PCOMP, PBEAML, PBUSH, etc., and include it in Nastran DAT files for all analyses.

5.1.2 Normal Modes Analysis

Initially, modal analysis is performed using Nastran SOL 103 to compute spacecraft natural frequencies and associated mode shapes. It is also used for model verification. The modal effective mass fraction is used to sort modes of interest in all six degrees of freedom [88]. In large-scale FEM analyses, the cost of matrix inversion to perform an eigenvalue analysis is very high due to a large number of degrees of freedom. A dynamic model reduction is performed automatically in Nastran using Craig-Bampton method [89]. The recalculation

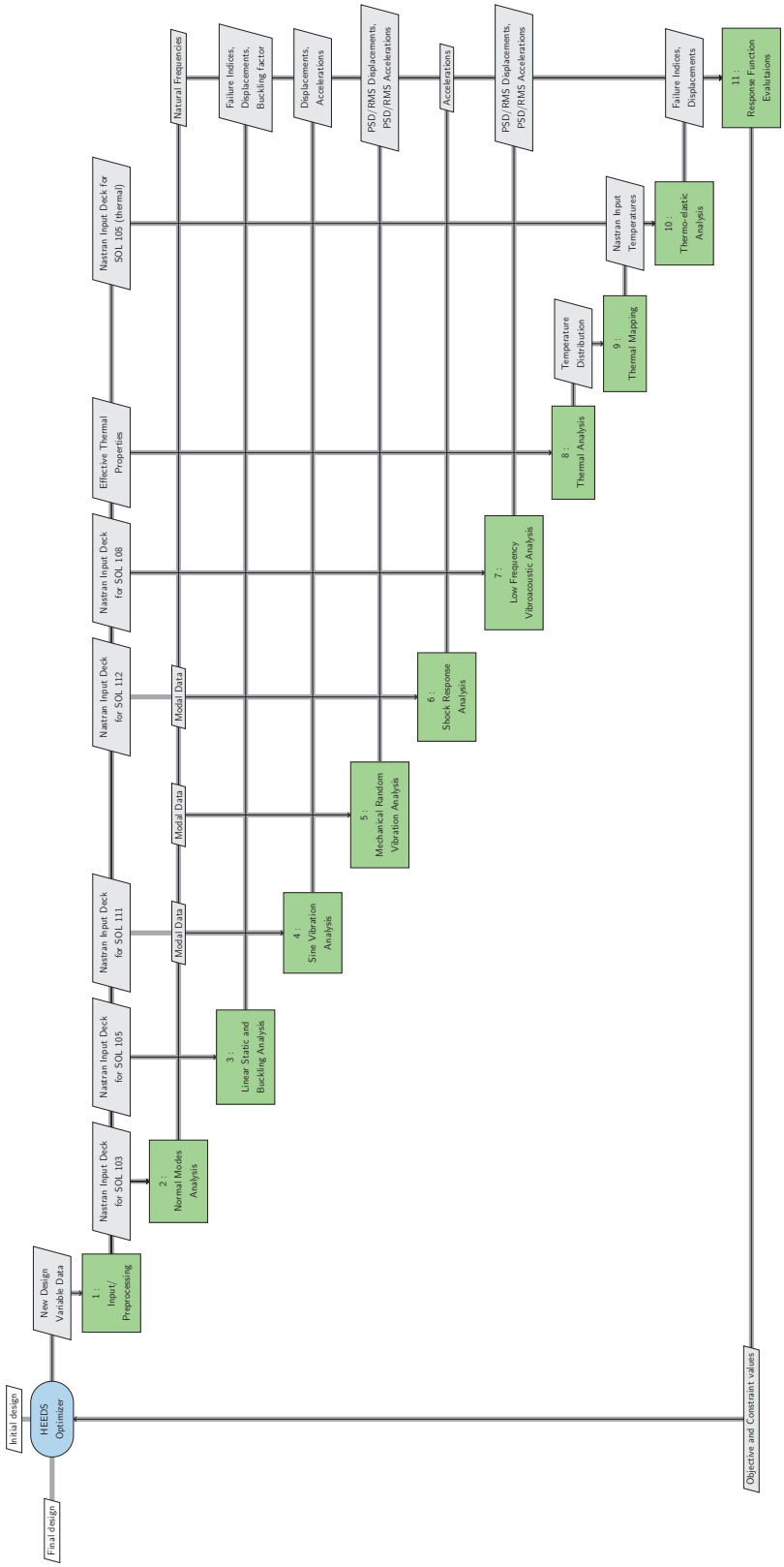

Figure 5.1: MSADO Design Structure Matrix.

of normal modes is prevented by using restarts for frequency response analysis. This is done by storing DBALL and MASTER scratch files using the command *scratch=no* in Nastran.

For any structural system, the equation of motion is given in the form,

$$[M_s]\{\ddot{u_s}(t)\} + [B_s]\{\dot{u_s}(t)\} + [K_s]\{u_s(t)\} = \{F_s(t)\} \tag{5.1}$$

where $[M]$ is the mass matrix, $[B_s]$ is the viscous damping matrix, and $[K_s]$ is the stiffness matrix. $\{F_s(t)\}$ is time dependent generalized force vector and $\{u_s(t)\}$ is the vector for the generalized degrees of freedom. By assuming a harmonic solution $\{u_s\} = \{\phi\}\sin\omega t$ for Eqn. (5.1), the undamped free vibration problem is simplified to

$$([K_s] - \omega^2[M_s])\{\phi\} = 0 \tag{5.2}$$

The eigenvalue problem in Eqn. (5.2) is solved for ω to find natural frequencies $f_i = \frac{\omega_i}{2\pi}(i = 1, 2, 3, \ldots)$. Eigenvectors $\{\phi_i\}$ give the corresponding mode shapes. The generalized mass and stiffness matrix is given as

$$\begin{aligned} [\hat{m}_s] &= \{\phi\}^T[M_s]\{\phi\} \\ [\hat{k}_s] &= \{\phi\}^T[K_s]\{\phi\} \end{aligned} \tag{5.3}$$

By statically applying a unit ground displacement, the resulting displacement of the masses is given by the vector $\{s\}$, also known as the influence vector. The modal participation factor $[\Gamma_i]$ for mode i can be evaluated as

$$\Gamma_i = \frac{\bar{L}_i}{\{\phi_i\}^T[M_s]\{\phi_i\}} = \frac{\bar{L}_i}{\hat{m}_{sii}} = \bar{L}_i(\text{with mass normalization}) \tag{5.4}$$

where $\bar{L}_i = \{\phi_i\}^T[M_s]\{s\}$. The effective modal mass can be evaluated from Eqn. (5.4) as

$m_{eff} = \bar{L}_i^2$. The total effective modal mass in each of the six degrees of freedom must be greater than 90% of the structure's mass to capture responses accurately.

5.1.3 Linear Static and Buckling Analysis with Mechanical Loads

The static and buckling analyses are carried out using Nastran SOL 105. The static analysis computes stresses in each element by solving $[K_s]\{u_s\} = \{F_s\}$ for displacements $\{u_s\}$. The stresses are used to build the geometric stiffness matrix $[K_G]$ to solve the linear buckling eigenvalue problem given in Eqn. (5.5) for buckling load factors λ. Nodal displacements, reaction forces/moments, and element stresses are output to the OP2 results file.

$$([K_s] - \lambda[K_G])\{\phi\} = 0 \tag{5.5}$$

5.1.4 Dynamic Analysis with Mechanical Loads

Sine and Random Vibration

The modal data in DBALL and MASTER files generated from the normal modes analysis is used to restart SOL 111 with sinusoidal loads and random loads. By substituting $\{u(t)\} = \{u_s\}e^{i\omega t} = [\phi]\{\xi(\omega)\}e^{i\omega t}$ in Eqn. (5.1), the equations of motion in modal coordinates ξ can be written as

$$\left[-\omega^2[\phi]^T[M_s][\phi] + i\omega[\phi]^T[B_s][\phi] + [\phi]^T[K_s][\phi]\right]\{\xi(\omega)\} = [\phi]^T\{F_s(\omega)\} \tag{5.6}$$

Except for Rayleigh viscous damping, Eqn. (5.6) is coupled for other types of viscous or structural damping, and the reduced system of equations is solved using the direct frequency solution approach.

Random Vibration is an extension of frequency response analysis where the frequency response functions are generated by applying a unit load in the desired direction. The response of the system subjected to random loads is governed by the power spectral density (PSD) function. Any physical quantity $u_j(\omega)$ can be evaluated using the system's transfer function $H_{ja}(\omega)$ when the system is subjected to excitation $F_a(\omega)$ as $u_j(\omega) = H_{ja}(\omega)F_a(\omega)$. The PSD of the response $S_j(\omega)$ is computed from PSDs of uncorrelated input excitations $S_a(\omega)$ as

$$S_j = \sum_a |H_{ja}(\omega)|^2 S_a \tag{5.7}$$

The root mean square (RMS) value of the response of the physical quantity is given by the square root of the area under the curve of Eqn. (5.7) and is evaluated as

$$u_j^{RMS} = \sqrt{\frac{1}{2\pi}\int_0^\infty S_j(\omega)d\omega} \tag{5.8}$$

Displacement and acceleration responses at locations of interest from sine vibration analysis are stored in the OP2 file. Random response outputs such as PSD/RMS displacements and accelerations computed from Eqn. (5.7) and Eqn. (5.8) are also stored for response function evaluations.

Shock Analysis

The shock imparted on the spacecraft due to payload separation at the payload-launch vehicle adapter interface can be analyzed using the Response Spectrum method or transient analysis. The industry standard for analyzing shock response is by using the modal combination method that can be directly used with shock response spectrum (SRS). In this method, single-degree-of-freedom systems with different natural frequencies and damping coefficients

are solved with shock time histories as base excitations. The response spectrum (displacement, velocity or acceleration) is constructed by recording the peak values of corresponding quantities occurring at each frequency.

The structural response for a given response spectrum is simply the product of response spectrum value at modal frequencies of the structure (independent of the structure) and the corresponding modal participation factors (property of the structure but independent of loading). The resulting response values are the peak values for the corresponding mode, and a modal combination method is used to get the peak response of the structure. The method provides reasonable estimates of peak values for simple systems where the entire system mass can be captured with fewer normal modes. In the case of complex, large-scale systems, the method has two major limitations. Analyzing complex composite spacecraft systems using the modal combination method results in conservative peak values that vary significantly by the inclusion of high-frequency modes. Secondly, designers are interested in the response spectrum of the output quantities, which is not possible with this approach as the response spectrum cannot be applied as base excitation to get the frequency response of the structure. Thus, in this study, a new method is proposed for shock analysis.

Any given SRS excitation can be synthesized into acceleration time history using a series of wavelets. The synthesized time history is applied as base excitation to the spacecraft system to get response time histories at desired locations. These locations are generally the mounting points for substructures, equipment boxes, payloads, or fuel tanks. The response time histories are converted back into response SRS. This gives designers a better understanding of the response of different components to be mounted on such locations without prior knowledge of their physical properties.

An individual wavelet is given as

$$W_m(t) = \begin{cases} 0, \quad t < t_{dm} \\ A_m \sin\left[\frac{2\pi f_m}{N_m}(t - t_{dm})\right] \sin\left[2\pi f_m (t - t_{dm})\right], \quad t_{dm} \leq t \leq t_{dm} + \frac{N_m}{2f_m} \\ 0, \quad t > \frac{N_m}{2f_m} \end{cases} \tag{5.9}$$

where $W_m(t)$ is the acceleration of wavelet m at time t, A_m is the amplitude, f_m is the wavelet frequency, N_m is the number of half-sines in the wavelet and t_{dm} is the wavelet time-delay. From Eqn. (5.9), the acceleration at any time t using a series of n wavelets is evaluated as

$$\ddot{u}(t) = \sum_{m=1}^{n} W_m(t) \tag{5.10}$$

The wavelet parameters A_m, N_m, f_m and t_{dm} must be chosen such that the SRS of the synthesized time history must closely match the SRS of the given excitation. The parameter values can be found as a part of the optimization problem to minimize errors between synthesized and specified SRS as

$$\textbf{minimize} \quad |\mathrm{SRS}_{spec} - \mathrm{SRS}_{synthesized}|$$

Since an infinite number of time histories can correspond to the same SRS, three different synthesized acceleration histories that represent the same SRS specification are chosen for shock analysis. They are used as three loading subcases in SOL 112. The output acceleration time histories from the analysis are converted back to SRS using the Smallwood ramp invariant method [90]. The frequency domain representation of the shock response thus obtained is used to constraint accelerations at different frequencies in the optimization.

5.1.5 Acoustic Analysis

The effect of acoustic noise generated from the fairing on the spacecraft is modeled as a two-way coupled vibroacoustic analysis in Nastran. For structure (spacecraft) placed inside a fluid domain as shown in Fig 5.2, the two-way coupled equations of motion [91] are given as

$$\begin{bmatrix} M_s & 0 \\ A_{fs}^T & M_{fl} \end{bmatrix} \begin{Bmatrix} \ddot{u}_s \\ \ddot{p}_{fl} \end{Bmatrix} + \begin{bmatrix} B_s & 0 \\ 0 & B_{fl} \end{bmatrix} \begin{Bmatrix} \dot{u}_s \\ \dot{p}_{fl} \end{Bmatrix} + \begin{bmatrix} K_s & -A_{fs} \\ 0 & K_{fl} \end{bmatrix} \begin{Bmatrix} u_s \\ p_{fl} \end{Bmatrix} = \begin{Bmatrix} F_s \\ F_{fl} \end{Bmatrix} \tag{5.11}$$

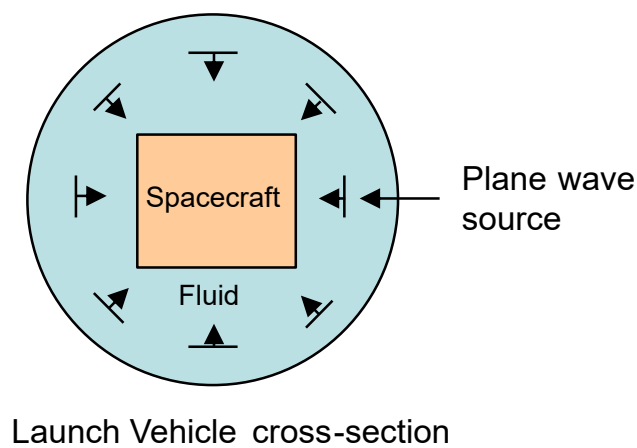

Figure 5.2: Spacecraft subjected to acoustic excitation inside a launch vehicle.

In Eqn. (5.11), the subscripts s and fl represent structural and fluid quantities. M_{fl}, B_{fl} and K_{fl} are known as the compressibility matrix, impedance matrix and mobility matrix, respectively. $\{u_s\}$ is the vector of structural displacements while $\{p_{fl}\}$ is the vector of fluid pressure. Similarly, F_s and F_{fl} are structure-borne and acoustic excitations, respectively.

The fluid-structure coupling matrix or the area matrix $[A_{fs}]$ is given in Eqn. (5.12),

$$[A_{fs}] = \int_S \xi_s^T \xi_f \{n_s\} dS \tag{5.12}$$

where S is the surface area of the structure exposed to fluid, ξ_s and ξ_f are shape functions for structural and fluid elements, respectively, and n_s is the outward normal to the structure at the fluid-structure interface. The acoustic field generated by the fairing is diffused and is modeled using multiple randomly distributed plane wave sources with specified sound pressure levels as input. The analysis is carried out using SOL 108 with the diffused acoustic field as a random excitation.

5.1.6 Orbital Heating Analysis

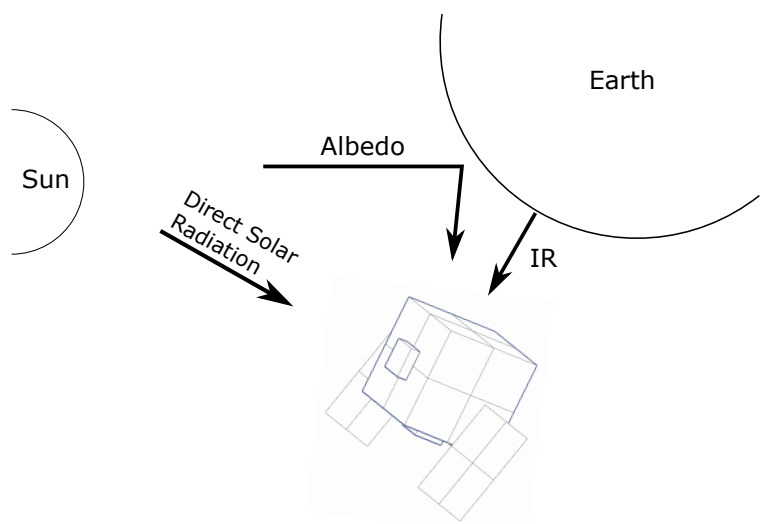

Figure 5.3: Orbital heating of spacecraft.

Orbital heating of the spacecraft results from three main sources of radiative heat fluxes. As shown in Fig. 5.3, at any given time, one or more of the spacecraft's exterior surfaces are exposed to direct solar radiation, albedo, and nearby planet's infrared radiation. The

heating and cooling cycles depend on the spacecraft's orbit. The inclusion of radiation and temperature-dependent properties makes the problem nonlinear. To capture the thermal response of the spacecraft structure with reasonable accuracy at different points in any given orbit, a nonlinear transient heat transfer analysis is conducted using NX Space Systems Thermal, which uses Maya HTT thermal solver. The finite element spatial description of the heat conduction equation [92, 93] is given as.

$$[C]\left\{\dot{T}\right\} + [\mathcal{K}]\{T\} + [R]\{T + T_a\}^4 = \{Q_v^{th}\} + \{Q_s^{th}\} \tag{5.13}$$

where $[C]$ is the heat capacitance matrix, $[\mathcal{K}]$ is the conductive conductance matrix and $[R]$ is the matrix for radiative conductances. $\{Q_v^{th}\}$ is the thermal load vector due to internal heat generation, and Q_s^{th} is the boundary surface heat flux, which can be temperature dependent. In Eqn. 5.13, the capacitance and conductance matrices are analogous to structural matrices since they are multiplied with the primary variables, i.e., nodal temperatures T, and their time derivatives. A temperature factor T_a is added to the radiation term to convert it into the absolute scale. The thermal matrices are computed as

$$\begin{aligned}
[C_{ij}] &= \int_\Omega \rho c \xi_i \xi_j d\Omega \\
[\mathcal{K}_{ij}] &= \int_\Omega \left[\kappa_x(T)\frac{\partial \xi_j}{\partial x}\frac{\partial \xi_i}{\partial x} + \kappa_y(T)\frac{\partial \xi_j}{\partial y}\frac{\partial \xi_i}{\partial y} + \kappa_z(T)\frac{\partial \xi_j}{\partial z}\frac{\partial \xi_i}{\partial z}\right] d\Omega \\
\{Q_{v(j)}^{th}\} &= \int_\Omega q_v \xi_j d\Omega \\
\{Q_{s(j)}^{th}\} &= \int_\Gamma q_s \xi_j d\Gamma
\end{aligned} \tag{5.14}$$

In Eqn. (5.14), ξ is the element shape function, ρ is the density, and c is the specific heat capacity of the material. The thermal conductivities are given by κ_x, κ_y, and κ_z in x, y, and z directions, respectively, whereas q_s is the surface heat flux on the material boundary Γ and q_v is the internal heat generation per unit volume in the material region Ω. The

radiative conductance or the radiation exchange matrix $[R]$ is used to evaluate net radiant heat exchange between different surfaces in an enclosure using view factor data and optical properties of radiating surfaces. The matrix $[R]$ can be computed as

$$[R] = \sigma^{th} \left\{ [A^{th}][e] - [A^{th}][a] \left([A^{th}] - [F^{ex}] + [F^{ex}][a] \right)^{-1} [F^{ex}][e] \right\} \tag{5.15}$$

where σ^{th} is the Stefan-Boltzmann constant, $[A^{th}]$ is the matrix of surface element areas and $[F^{ex}]$ is a matrix of exchange coefficients that are functions of view factors. The optical properties of surfaces form matrices $[e]$ and $[a]$ for emissivities and absorptivities, respectively. A Newton-Raphson scheme with Wilson-Theta time integration is used to solve Eqn. (5.13) for nodal temperatures. The ith iteration at time step $n+1$ can be written as

$$\left(\frac{1}{\vartheta \Delta t_{n+1}} [C]^i_{n+1} + [\mathcal{K}_T]^i_{n+1} \right) \{\Delta T\}^i_{n+1} = \{\mathcal{R}\}^i_{n+1} \tag{5.16}$$

where $\mathcal{R}$ is the residual to be minimized, Δt_{n+1} is the time step at step $n+1$ and $[\mathcal{K}_T]$ is the tangent conductance matrix. An approximation $\frac{1}{\vartheta \Delta t_{n+1}} [C]^i_{n+1} + [\mathcal{K}_T]^i_{n+1} \approx \frac{1}{\vartheta \Delta t_{n+1}} [C]_n + [\mathcal{K}_T]_n$ in Eqn. 5.16 is used to save inversion cost in each equilibrium iteration. The tangent conductance is further approximated as

$$[\mathcal{K}_T]_n \approx [\mathcal{K}]_n + 4[R]_n \{T_n + T_a\}^3 - \left\{ \frac{\partial Q^{th}_s}{\partial T} \right\}_n \tag{5.17}$$

Note that the tangent conductance in Eqn. 5.17 includes both conductive and radiative conductances as well as temperature-dependent loads such as boundary radiation. The right

hand side of Eqn. 5.16, i.e., the residual $\mathcal{R}^i_{n+1}$ is calculated as

$$\begin{aligned}\{\mathcal{R}\}^i_{n+1} = \{Q^{th}_v\}_{n+1} + \{Q^{th}_s\}^i_{n+1} - [\mathcal{K}]^i_{n+1}\{T\}^i_{n+1} - [R]^i_{n+1}\{T^i_{n+1} + T_a\}^4 \\ + \left(\frac{1}{\vartheta} - 1\right)\left(\{Q^{th}_v\}_n + \{Q^{th}_s\}_n - [\mathcal{K}]_n\{T\}_n - [R]_n\{T_n + T_a\}^4\right)\end{aligned} \tag{5.18}$$

Since there is no phase change involved in the thermal analysis of spacecraft with materials considered in this work, the enthalpy terms used to model phase change are not considered in Eqn. 5.18.

First-order implicit time integration ($\vartheta = 1$) is used in the current work. The thermal analysis process starts with the computation of conductive conductance $[\mathcal{K}]$ and capacitance networks $[C]$, followed by view factors for radiation heat fluxes. The thermal couplings are established, and radiative conductances $[R]$ are evaluated to build heat conduction matrices. The task of computing view factors and building radiative conductance matrices is computationally intensive since it involves a significant amount of matrix operations with computational effort scaling of $\mathcal{O}(n_s^3)$ with the number of element surfaces n_s. To improve solver performance, either multiple finite elements can be grouped together to create radiation patches, or the total number of elements in the thermal model can be reduced using parabolic elements.

Alternatively, if the optical properties $[a]$, $[e]$ and the geometry of the structure $[A^{th}]$ are kept constant throughout the optimization process, the gray body view factors remain constant. Thus, from Eqn. 5.15, the radiative conductances $[R]$ remain constant and can be computed only once per optimization to save significant computational resources. In this study, heat transfer analysis is run fully for the first design and the solution is restarted in subsequent optimization iterations with view factor and radiative conductance data of the first analysis. The nodal temperatures are obtained at specified time steps and used for thermal mapping.

5.1.7 Thermal Mapping

Since primary variables like nodal temperatures are the focus of thermal analysis, good accuracy can be obtained even by using coarse meshes. The goal is to use a coarse mesh for the thermal model but a finer mesh for the structural model for more accuracy. The nodal temperatures from the coarse mesh in the orbital heating analysis are mapped to the fine mesh of the structural model using interpolation inside Simcenter 3D. The mapping module also generates the Nastran temperature load files that must be included in thermal-stress analysis.

5.1.8 Thermal-Stress Analysis

With the temperature data obtained from orbital heating, Nastran SOL 105 is run to evaluate thermal deformations, stresses, and buckling load factors of the spacecraft.

5.1.9 Response Evaluation

A Python script is used with pyNastran to extract results from all OP2 files. This is much faster than the parser integrated into HEEDS for large data sets. Desired responses, such as maximum displacement, minimum buckling load factor, maximum failure index, etc., are computed inside the script and sent to HEEDS for optimization. The entire flow process is shown in Fig. 5.4.

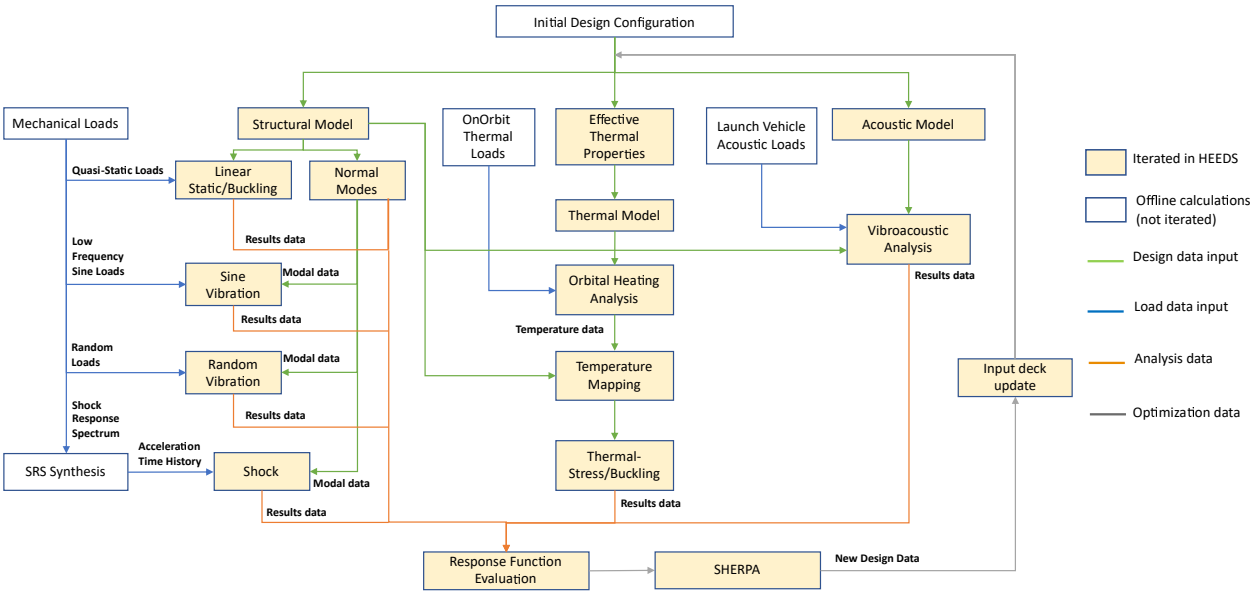

Figure 5.4: MSADO Blueprint

5.2 Multidisciplinary Design Optimization of Composite Laminate

With the description of the optimization framework, a simple composite laminate optimization problem is chosen to demonstrate the MSADO using the structure and thermal disciplines. The structures discipline includes statics, normal modes, frequency response, and transient response analysis, whereas the thermal discipline involves steady-state non-linear heat transfer analysis. Three individual optimizations are performed to maximize the buckling load factor, fundamental frequency, and buckling temperature. The values obtained for each optimum design are used as constraints in the minimum weight design of the laminate. This is done to establish a reference that can be used to explain the results of the laminate MSADO.

5.2.1 Laminate Multidisciplinary Analysis Setup

A simply supported rectangular laminate is subjected to uniform in-plane bi-axial compressive loads, as shown in Fig 5.5. The analysis uses Nastran SOL 105 to evaluate static stress and buckling load constraints. A steady state acceleration is used for frequency response evaluations, and an impulse load is used for the transient response. These are solved using Nastran SOL 111 and SOL 112, respectively, with the modal data extracted from modal analysis performed using SOL 103.

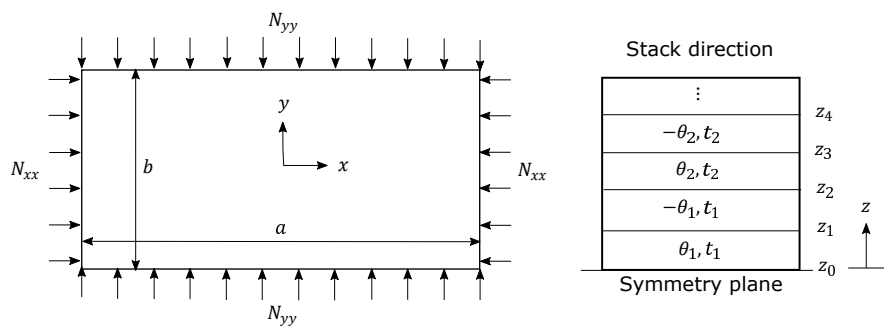

Figure 5.5: Rectangular Composite Panel subjected to Bi-axial Loading.

Evaluation of thermal stresses and buckling temperature requires information about the temperature distribution over the structure. This temperature distribution is a function of the structure's geometric and material properties, and hence, a heat-transfer analysis needs to be performed at every iteration of the optimization process. In this case, the laminate is subjected to a uniform heat flux on the top surface. The boundaries are constrained at ambient temperature to create a thermal gradient. The laminate heat transfer analysis uses Nastran SOL 153 instead of Space Systems Thermal, as orbital heating is not used. The temperature distribution obtained from SOL 153 is used as loads in the thermo-elastic analysis to get thermal stresses and thermal buckling load factor. Due to the limitations of Nastran to support PCOMP property in SOL 153, the laminate is modeled as an equivalent shell. It requires the computation of effective thermal conductivities as input for MAT5

material card. This is done at each iteration using a Python script before SOL 153 is run. The effective conductivities are obtained using simple thermal resistance circuits in series and parallel.

5.2.2 Laminate Optimization with Direct Method

The objective is to minimize the laminate weight by minimizing the number of plies N. The laminate is assumed to be symmetric and balanced. The primary design variables are fiber orientations θ_k. To maintain a balance configuration, a ply with $+\theta_k$ orientation is paired with one having $-\theta_k$ orientation. The number of plies as design variables makes the optimization a variable design space problem. To solve it using available algorithms, the total number of plies is fixed, and a dummy material is used to occupy the removed plies. A binary indicator response I is assigned to each ply to identify plies with dummy material and write a new PCOMP property entry with the actual number of plies in the Nastran input deck in each iteration. This is achieved by running a pyNastran script for pre and post-processing. The optimization is subjected to frequency, deformation, and buckling constraints evaluated from structural and thermal disciplines. The optimization problem formulation and results are presented in the next section.

5.2.3 Individual Objective Maximization

An appropriate optimization algorithm is chosen for the direct method such that it has the capability to handle discrete combinatorial design problems as that observed in large composite structural designs. Depending on the nature of design variables and constraints, appropriate gradient-based or gradient-free optimization algorithms must be used to get quality solutions efficiently. As mentioned earlier, gradient-based optimizers can quickly

arrive at a local optimum and are suited for large-sized problems with a less number of local minima. Global optimization algorithms, in search of the best solution, spend more time than gradient-based optimizers in the solution process. They are more suited for small to medium-sized problems with multiple minima but may incur significant computational costs for large-scale structural optimization. The limitations of conventional heuristic algorithms are seen in the results of Chapters II, II and IV.

HEEDS integrates a global optimization algorithm named SHERPA [94], or Simultaneous Hybrid Exploration, that is Robust, Progressive, and Adaptive. The algorithm uses multiple local and global search methods simultaneously, takes the best attributes of each method, and adapts to the design space accordingly. The tuning parameters of each search method are adjusted based on the evolving knowledge of the design space. Thus, the algorithm efficiently searches across different types of design spaces. This is a suitable strategy for the optimization of large composite structures where all design variables are optimized in one pass.

Optimum designs of the composite laminate subjected to different loading conditions are first studied to understand its response characteristics. Under mechanically induced static loads, the minimum buckling load factor λ_b is maximized, whereas for thermally induced static loads, the minimum buckling temperature λ_T is maximized. A third maximization is performed for obtaining the fundamental frequency f as given in Table 5.1. The laminate is made of T300/5208 material with a ply thickness of 0.005 inches. The number of plies N is fixed to 16 and a symmetric layup is assumed. For buckling load maximization, the laminate is subjected to $N_x = 1$ lb/in. and $N_y = 0.5$ lb/in. whereas for buckling temperature maximization, a uniform ΔT of 1°F is assumed. The optimization is run in HEEDS using the SHERPA algorithm.

The results given in Table 5.2 show that each optimization arrives at a different layup

Table 5.1: Optimization Formulation for Individual Objective Maximization.

Objective	Buckling load	Fundamental frequency	Buckling temperature
maximize	$\min(\lambda_b)$	$\min(f)$	$\min(\lambda_T)$
s.t.	$\theta_k \in \{0°, \pm 45°, 90°\}$ for $k = 1, 2, \ldots, N$		

Table 5.2: Individual Objective Maximization Results for a 16 Ply Laminate.

Parameters	Buckling load factor	Fundamental frequency	Buckling temperature factor
Value	$\lambda_b = 2947.75$	$f = 974.3$ Hz	$\lambda_T = 567.57$
Layup	$[90_2, (\pm 45)_2, 90_2, (\pm 45)_4]_S$	$[90_{16}]_S$	$[90_2, (\pm 45)_3, 90_8]_S$

configuration to achieve the maximum objective value. In the case of buckling load, the optimal stacking sequence consists of ±45° and 90° plies only. The 45° plies provide higher stiffness in the loading direction resulting from bi-axial compression. The 90° plies balance the higher magnitude of total load induced in the transverse direction (N_y). As opposed to buckling load maximization, frequency maximization tries to achieve a configuration where all plies have fibers oriented at 90°. Due to the high aspect ratio, increasing the stiffness in the transverse direction significantly increases the natural frequency of the laminate. In the case of buckling temperature, it is observed that the stacking sequence is dominated by 90° plies. In the weight minimization study, the previously obtained optimal objective values for buckling load and fundamental frequency are used as constraints to establish a baseline for minimum weight design. This means that the total number of plies N in the minimum weight design cannot go lower than 16.

5.2.4 Weight Minimization using MSADO Framework

The laminate design is subjected to constraints where the buckling load factor λ_b must be greater than $\lambda_{cr} = 2940$ and the fundamental frequency f must be greater than $f_{cr} = 970$

Hz. To make the problem multidisciplinary, a steady-state heat transfer analysis is added to calculate the temperature distribution in each iteration. The top surface of the laminate is subjected to a uniform heat flux of 25 lbf/s-in, and the normalized buckling temperature is used as a constraint. A frequency response analysis is added to simulate steady-state acceleration of 1G. A 0.001 in. transverse impulse displacement is induced at the boundaries to capture the laminate's transient response. Transverse displacement output δ from each analysis is constrained to $\delta_{cr} = 0.01$ in. or 3% of the total initial laminate thickness. After careful observation of ply stress values in multiple analysis runs, it is seen that the von Mises stresses in each ply are orders of magnitude lower than the allowable yield stress. Thus, this constraint is not used in the laminate study but instead will be added directly in the spacecraft optimization. The objective to minimize weight is written as the sum of all indicator values I_k. The first four constraints refer to the buckling load limit, fundamental frequency limit, buckling temperature limit, and out-of-plane deformation limit, respectively. The fifth constraint ensures that the unoccupied plies with $I_k = 0$ lie on the outside. The optimization problem takes the form shown below.

$$
\begin{array}{lll}
\textbf{minimize} & W = \sum_{k=1}^{N} I_k & \\
\textbf{w.r.t.} & I_k, \theta_k & k = 1, 2, \ldots, N \\
\textbf{s.t.} & \min(\lambda_b) \geq \lambda_{cr} & \\
 & f \geq f_{cr} & \\
 & \min(\lambda_T) \geq 1 & \\
 & \max(\delta) \leq \delta_{cr} & \\
 & I_k - I_{k+1} \geq 0 & k = 1, 2, \ldots, N-1 \\
 & \theta_k \in \{0^\circ, \pm 45^\circ, 90^\circ\} & \\
 & I_k \in \{0, 1\} &
\end{array}
$$

Minimization of the total number of plies instead of thickness requires us to define an upper limit for the number of plies. The number of orientation variables θ_k depends on the number of plies N, and thus, the total number of design variables must be defined based on the upper limit of N. In this case, the limit is set to $N = 30$ resulting in 15 orientation variables

(paired orientations) and 30 indicator variables. Care is taken to check if the outer ply is an odd-numbered ply and assign it 0° or 90° orientation to maintain a balanced configuration. The optimization is run in HEEDS on an Intel Xeon W2265 with 12 cores, 128 GB RAM, and an Nvidia Quadro RTX 5000 GPU. Since the current model only has 1600 elements, it does not benefit from CPU or GPU parallelization but instead benefits significantly from analysis parallelization as three analyses can be run at the same time. The results of MSADO are presented in Table 5.3 along with objective and constraint history in Fig 5.6.

Table 5.3: Laminate Weight Minimization Results using MSADO Framework.

Parameters	Value
Number of plies N	17
Buckling load factor λ_b	2995.27
Fundamental frequency f (Hz)	971.38
Thermal buckling load factor λ_T	8.38
Maximum displacement δ (in.)	0.001
Layup	$[90_3, \pm 45, 90_{10}, 0_2]_S$
Total design evaluations	3450

The laminate is initialized with $N = 30$ i.e., all indicator values are set to 1. The optimizer has to switch indicator values of outer plies and, at the same time, choose the optimal orientation for the remaining plies. With 45 discrete design variables and multi-modal constraints, the combinatorial problem is challenging to solve. As seen from Fig 5.6(a), it takes the optimizer around 1000 design evaluations to start reducing the number of plies at a faster rate. At the start, the SHERPA algorithm spends time exploring the design space and learning about key parameters that can have a higher impact on the objectives and constraints. Roughly after 1000 designs, it starts converging at a faster rate and arrives at an optimum of $N = 17$ plies in 2200 evaluations. Buckling load factor and frequency constraints are active for the optimum design as seen from Fig 5.6(b) and (c). The buckling load factor strongly depends on the number of plies, whereas the fundamental frequency is more dependent on

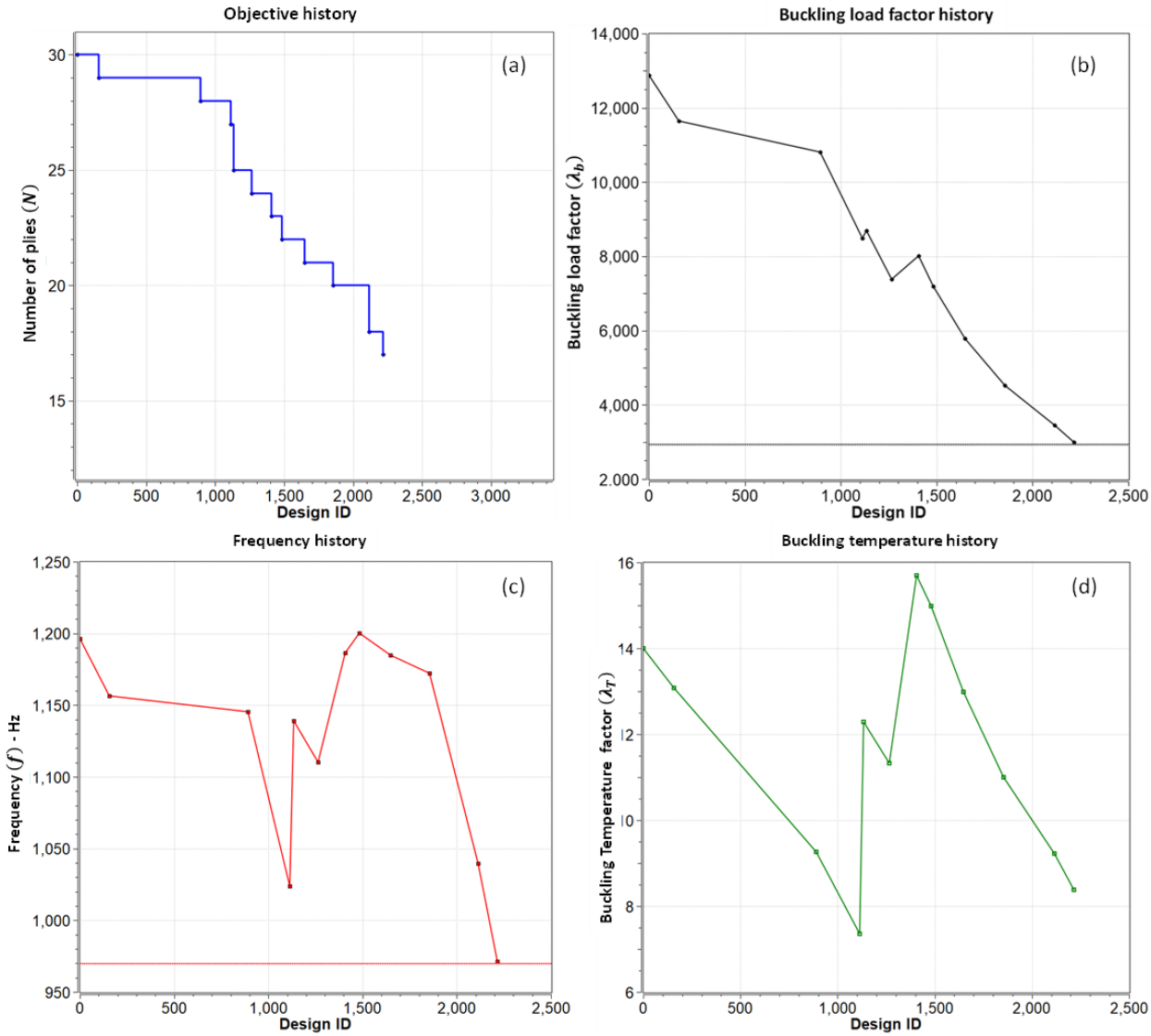

Figure 5.6: Convergence plots for the objective and active constraints, (a) Objective convergence showing the total number of plies, (b) Buckling load factor convergence, (c) Fundamental frequency convergence, and (d) Buckling temperature factor convergence.

the stacking sequence of each ply. Thus, in intermediate design evaluations, there is a discrepancy between the convergence of the above two constraints where the stacking sequence favorable for one constraint may not be favorable for the other. The buckling temperature constraint was never active, as observed from Fig 5.6(d). This might be due to the lower magnitude of heat flux applied to the laminate. Overall, it is seen that the optimizer attains

a global convergence at 17 plies by finding a stacking sequence that is good for the buckling and fundamental frequency constraints. This is also in good correlation with the results from individual objective maximization, where the results are obtained for $N = 16$.

Chapter 6

Multidisciplinary Optimization of a Small Spacecraft

The spacecraft design shown in this chapter complies with standard component-level qualification practices such as General Environmental Verification Standard (GEVS) [95], Space and Missile System Center (SMC-S-016) [96] and Military Standard (MIL-800) [97]. The launch vehicle loading environments and electronic component damage tolerances are defined from the above standards.

6.1 Finite Element Model

6.1.1 Component Description

An idealized model of a small spacecraft is considered in this study. It includes a bus attached with three solar arrays, fourteen electronic boxes, a payload, a fuel tank, and a spacecraft separation adapter ring, as shown in Fig 6.1.

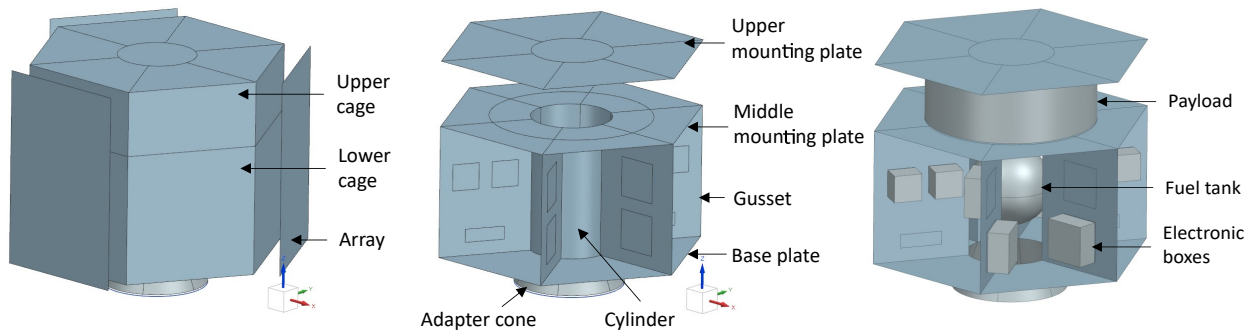

Figure 6.1: Spacecraft CAD Model.

Bus

The bus is modeled as a hexagonal prismatic structure having a base plate, middle mounting plate, and upper mounting plate. The lower section of the bus is separated into six sections using six gusset panels. The electronic boxes are mounted on the gusset panels. A central cylindrical core extends from the adapter cone to the middle mounting plate and houses the fuel tank. The payload is fixed to the middle mounting plate. The bus structure is enclosed with six lower cage and upper cage panels. Each of the bus panels is modeled as a sandwich composite with IM7/9773 face sheets and an Al 5056 honeycomb core. Material properties for the same are given in Table 6.1. The bus panel dimensions are given in Fig 6.2. Partitions are made on the panels at equipment mounting locations for easy definition of connection properties.

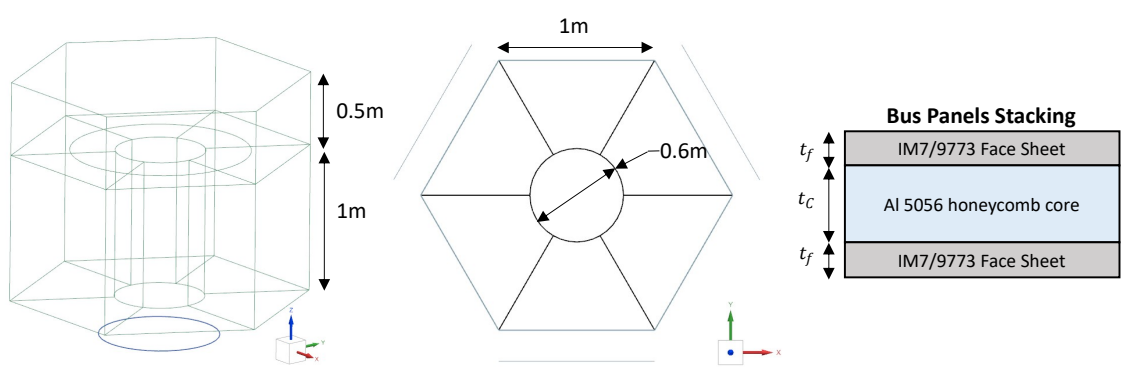

Figure 6.2: Bus Schematic and stacking.

Table 6.1: Material Properties of Bus Module.

Material	IM7/977-3	Al 5056 core with cell size 3/8
Mechanical Properties		
Density (ρ)	1570 kg/m^3	1 pcf
Longitudinal Young's modulus (E_1)	130.4 GPa	-
Transverse young's modulus ($E_2 = E_3$)	8.98 GPa	103.42 MPa
In-plane shear modulus ($G_{12} = G_{13}$)	5.02 GPa	46.88 MPa
Out of plane shear modulus (G_{23})	3 GPa	103 MPa
In-plane Poisson's ratio ($\nu_{12} = \nu_{13}$)	0.32	-
Out of plane Poisson's ratio (ν_{23})	0.496	0.45
Fiber direction tensile strength (X_t)	2900 MPa	-
Fiber direction compressive strength (X_c)	1680 MPa	-
Transverse direction tensile strength (Y_t)	100 MPa	-
Transverse direction compressive strength (Y_c)	247 MPa	-
Out of plane tensile strength (Z_t)	100 MPa	-
Out of plane compressive strength (Z_c)	247 MPa	0.24 MPa
In-plane shear strength ($S_{12} = S_{23}$)	80 MPa	241.31 MPa
Out of plane shear strength (S_{23})	57 MPa	379.21 MPa
Thermo-elastic Properties		
CTE - 1 direction (α_1)	0.18E-6 °C^{-1}	23.5E-6 °C^{-1}
CTE - 2 direction (α_2)	23.4E-6 °C^{-1}	23.5E-6 °C^{-1}
Thermal Properties		
Specific heat (c_p)	885.916 J/kg.K	921.6 J/kg.K
Thermal conductivity - 1 direction (κ_1)	7.1425 W/m.K	0.6 W/m.K
Thermal conductivity - 2 direction (κ_2)	0.5460 W/m.K	1.067 W/m.K

Each spacecraft bus panel is covered with closeout frames to connect two panels using fasteners for a better representation of actual spacecraft panel connections. Two types of closeout sections, along with their dimensions, are shown in Fig 6.3. The C-section or channel section is used for frames covering the panels with angled connections, whereas the I-section is used wherever two panels are connected along the same plane. Closeouts for all bus panels are shown in Fig 6.4.

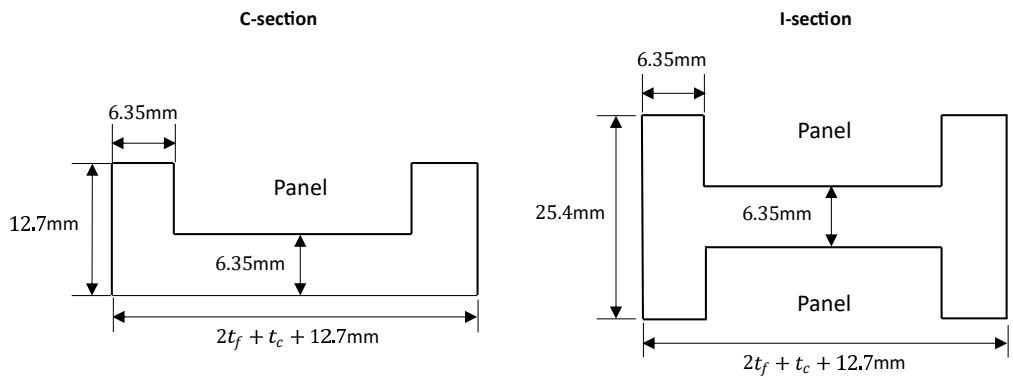

Figure 6.3: Closeout frame sections.

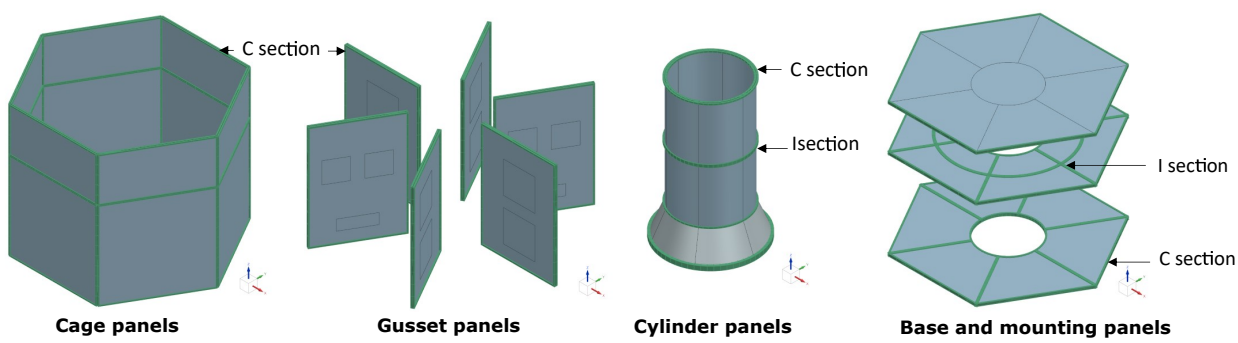

Figure 6.4: Closeout definitions for different panels.

Solar Array

The solar arrays are modeled as sandwich panels as load-bearing elements with a thin film of solar cells covered by glass top as shown in Fig 6.5. Each of the three arrays is placed 0.2 m away from the corresponding adjacent bus panel. The face sheets are made from M55J/CE3 high modulus and high heat conduction composite, while the core is made from Al 5056 with the properties given in Table 6.2.

Electronic Boxes

Three types of electronic boxes are used in the spacecraft model. Each box is modeled as a cuboid of material with the same stiffness as Al 6061 but with a reduced equivalent density

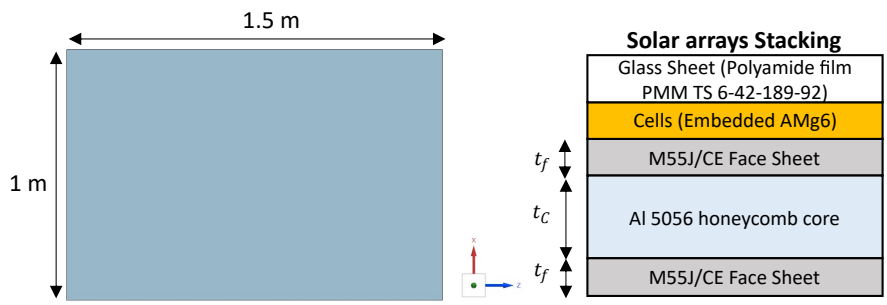

Figure 6.5: Solar array schematic.

Table 6.2: Material Properties of Solar Array.

Material	M55J/CE3	Cells	Glass sheet
Mechanical Properties			
Density (ρ)	1910 kg/m^3	2700 kg/m^3	1650 kg/m^3
Longitudinal Young's modulus (E_1)	275.80 GPa	Not used in structural analysis	
Transverse young's modulus ($E_2 = E_3$)	5.543 GPa		
In-plane shear modulus ($G_{12} = G_{13}$)	5.02 GPa		
Out of plane shear modulus (G_{23})	4.205 GPa		
In-plane Poisson's ratio (ν_{12})	0.27		
Fiber direction strength (X)	772 MPa		
Transverse direction strength ($Y = Z$)	23.44 MPa		
Shear strength (S)	28.95 MPa		
Thermo-elastic Properties			
CTE - 1 direction (α_1)	-1.088E-6 °C^{-1}	Not used in structural analysis	
CTE - 2 direction (α_2)	31.7E-6 °C^{-1}		
Thermal Properties			
Specific heat (c_p)	711.3 J/kg.K	335 J/kg.K	712 J/kg.K
Thermal conductivity - 1 direction (κ_1)	107.77 W/m.K	32.8 W/m.K	1.5 W/m.K
Thermal conductivity - 2 direction (κ_2)	1.01 W/m.K	32.8 W/m.K	1.5 W/m.K

of 833 kg/m^3 to represent casing weight and stiffness accurately. The weight of electronic components is added as point masses using Nastran's CONM2 property. The three boxes, along with dimensions, are shown in Fig 6.6, and the mass breakdown is given in Table. 6.3. These boxes are attached to the gusset panel cutouts using fasteners.

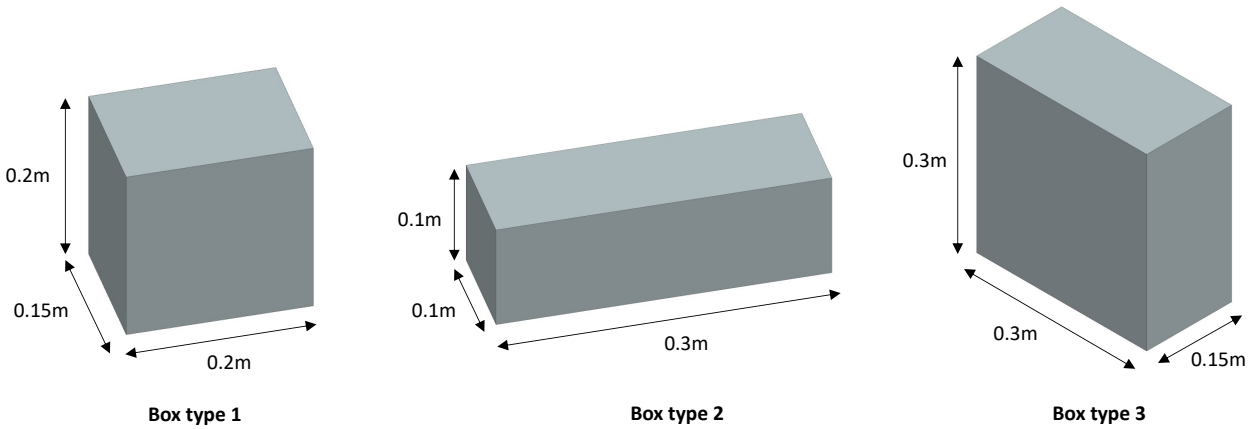

Figure 6.6: Electronic boxes.

Table 6.3: Properties of electronic boxes.

Type	Casing mass (kg)	Point mass (kg)	Total box mass (kg)
1	0.5	15	15.5
2	0.25	20	20.25
3	1.125	10	11.125

Payload

The payload is modeled as a solid cylinder of Al 6061 as shown in Fig 6.7 with a reduced density of 833 kg/m^3 similar to that for electronic boxes. Thus, the casing mass equal to 36 kg with an additional point mass of 65 kg results in a total payload mass of 101 kg. The payload is attached to the middle mounting plate of the bus via fasteners.

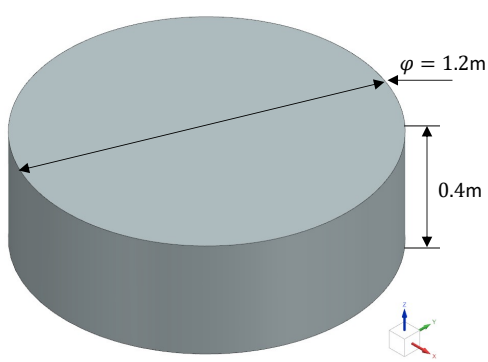

Figure 6.7: Payload schematic.

Fuel Tank

A solid spherical representation of the fuel tank with a radius equal to 0.29 m is considered in this work as shown in Fig 6.8. The tank is made of titanium alloy Ti-6Al-4V with Young's modulus of 121 GPa and Poisson's ratio of 0.34. The density is reduced to 133 kg/m^3 to get an effective casing mass of 12 kg. The mass of the hydrazine fuel is added as a point mass of 100kg by considering an 88% fill ratio.

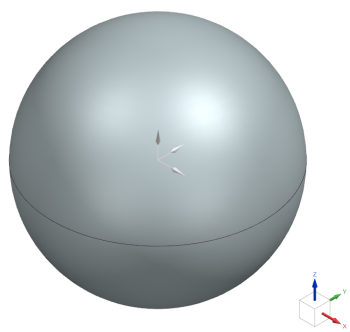

Figure 6.8: Fuel tank schematic.

Spacecraft Separation Adapter

The separation adapter is modeled based on the Planetary Systems Corp. 2000785G MkII lightband [98]. The bolt circle diameter φ is chosen as 31.6 inches to increase the overall stiffness without adding considerable mass to the satellite. Only the upper ring of the lightband is used as a part of the modeling process. The ring is modeled as an Al 7075 beam with a rectangular cross-section, as shown in Fig 6.9. The ring is divided into 60 equal sections for bolt connections.

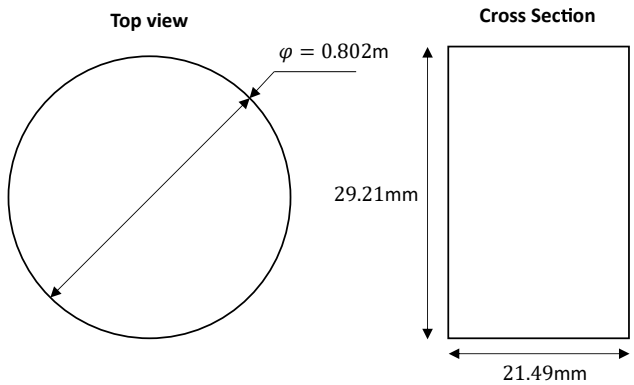

Figure 6.9: Adapter upper Ring Schematic.

6.1.2 Mesh and Assembly

Finite Element Mesh

The spacecraft bus and array panels are meshed with Nastran CQUADR elements having six degrees of freedom per node. The baseline mesh has an element size of 100 mm for the cage, gusset, array, and outer edges of the mounting panels, whereas the mesh is mapped structurally inwards towards the cylinder. A mesh coat is used for closeouts to merge CBEAM elements to panel edges. There are a total of 3984 CQUADR elements and 1374 beam elements. The electronic boxes are modeled using CHEXA8 elements, while the payload and fuel tank are modeled with CTETRA4 elements. The spacecraft mesh is shown in Fig 6.10.

Structural Model Assembly (Stowed Configuration)

The structural model of the stowed spacecraft is used to perform static and dynamic analyses due to mechanical and acoustic loads. The configuration shown in Fig 6.10 represents the spacecraft when it is fixed at the spacecraft separation interface inside the launch vehicle. The solar arrays are positioned parallel to the vertical faces of the bus. The arrays are

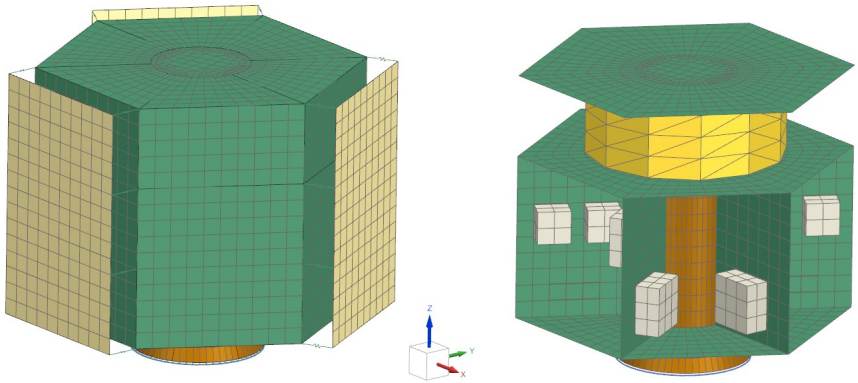

Figure 6.10: Spacecraft mesh.

connected to the bus using beam elements at the midpoint of the bottom edges, as shown in Fig 6.11a. CBUSH elements are used as fastener mounts to constrain eight points on the vertical edges of each array to the nearest bus nodes. Similarly, the electronic boxes and payload are connected to the bus panels using CBUSH as fasteners. A gap of 10 mm is kept between the panel and the boxes. The fuel tank is placed at the center of the cylinder and is connected to the cylinder using CBUSH elements, as shown in Fig 6.11c. To improve the representation of the spacecraft model further, two panels are connected together with coincident CBUSH elements instead of node merging to add fastener stiffness and damping. This is shown in Fig 6.11d.

Vibroacoustic Model Assembly

In addition to the structural model, the finite element method for vibroacoustic analysis requires the definition of a 3D fluid domain that wraps around the structure. To generate the CAD model of the fluid, the structural model is cut out from a solid hexagonal block using NX. With the Automatically Matched Layer (AML) option, a small fluid domain, as shown in Fig 6.12, can be used to increase the computational efficiency of the analysis. Edge blends are used to make the domain convex which is necessary to define AML. The fluid

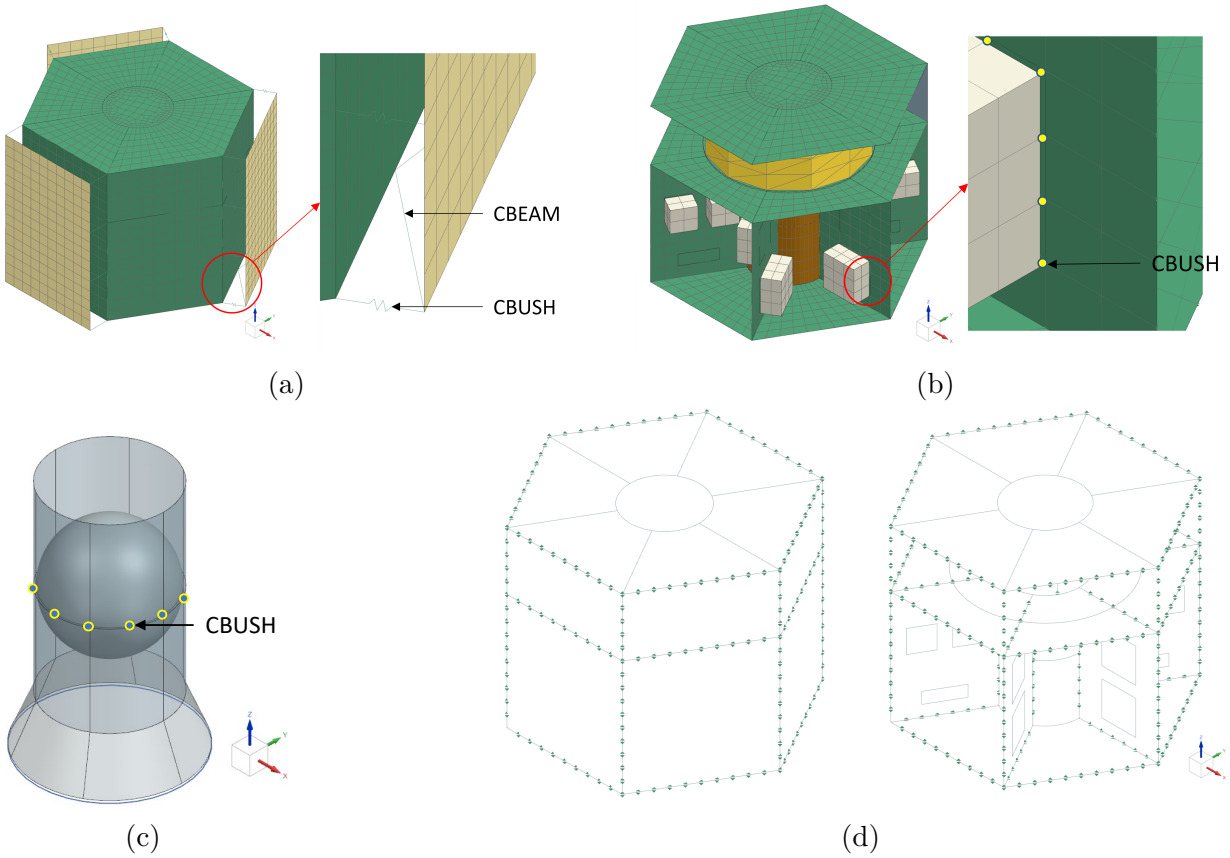

Figure 6.11: Spacecraft structural model assembly.

domain is meshed with CTETRA4 acoustic elements having a baseline size of 150 mm. The spacecraft and fluid domain together are shown in Fig 6.13.

Thermal Model Assembly (Deployed Configuration)

Thermal and thermo-elastic analyses are performed on the spacecraft in the deployed configuration when it is operating in orbit. The solar arrays are rotated such that they are parallel to the Z-plane to represent their deployed state as shown in Fig 6.14. The CBUSH connections are unnecessary in this configuration and, thus, are removed from the model. When the satellite is in orbit, the heat transfer is mainly due to conduction between structural elements and radiation from stars and planets. For a suitable depiction of heat flow

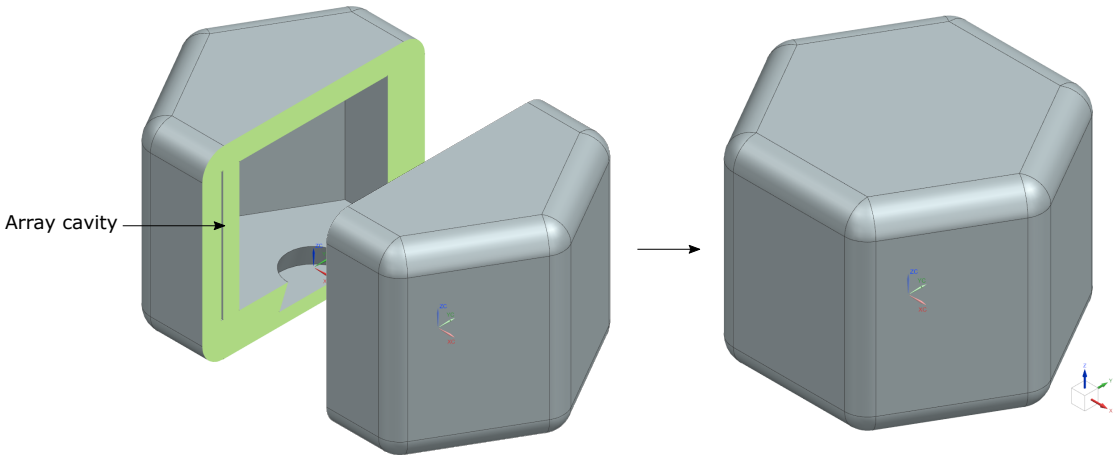

Figure 6.12: Fluid domain for the vibroacoustic model.

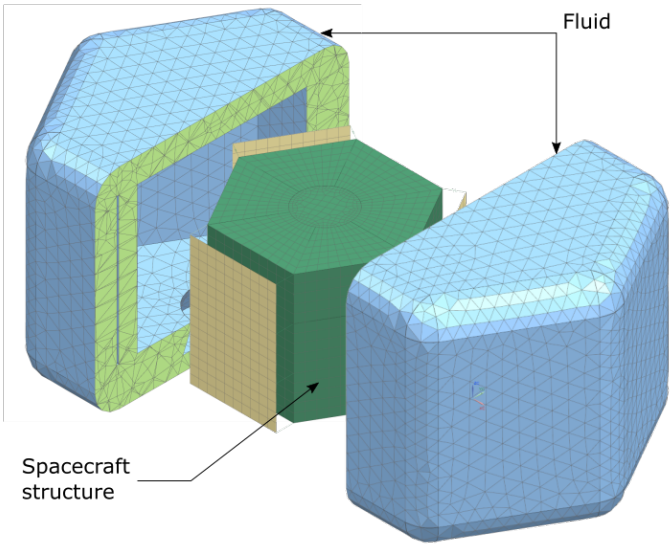

Figure 6.13: Vibroacoustic model setup.

due to radiation, surface treatments with optical properties given in Table 6.4 are used for each component. Multi-layer shells are used wherever possible to allow heat conduction in the out-of-plane direction. For simplification, the face sheet is modeled as a single layer with effective thermal properties. Thus, a total of five shell layers are used for each solar array and three shell layers are used for the bus. The electronic boxes, payload, and fuel tank are assumed to be thermally decoupled and insulated.

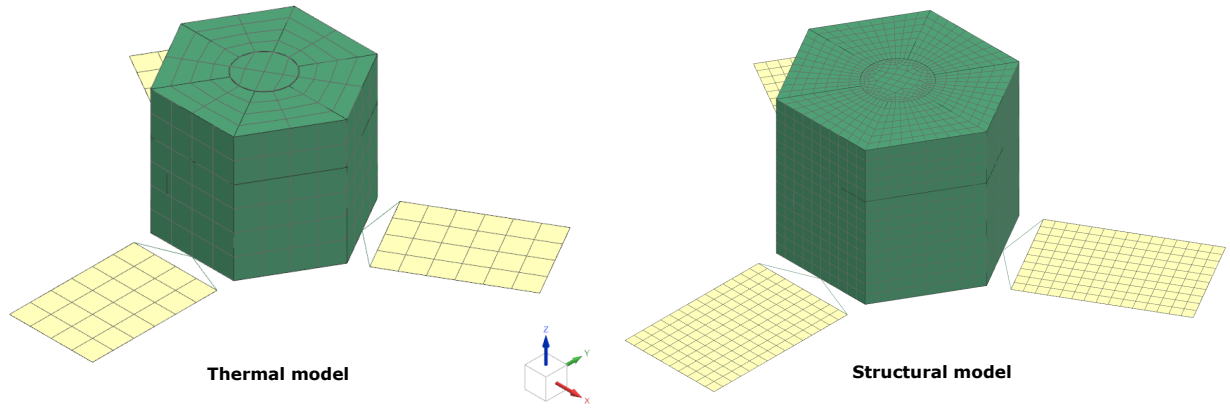

Figure 6.14: Deployed spacecraft used in the thermal and thermo-elastic analysis.

Table 6.4: Optical properties of different material surfaces [9].

Material	Glass outer surface	Cells	Array top face sheet	Array bottom face sheet	Bus face sheets	Core
Absorptivity (a)	0.05	0.89	0.9	0.39	0.55	0.15
Emissivity (e)	0.9	0.85	0.74	0.88	0.85	0.05
Transmissivity (τ)	0.95	-	-	-	-	-

Response Output

Linear static analyses with mechanical and thermal loads are used to output lamina failure indices, beam stresses, and nodal deflections at all locations except near fasteners and constraints. In dynamic analyses, the displacements and accelerations are of primary concern since the working of many components is sensitive to small movements. The displacements and accelerations in all dynamic analyses are obtained at equipment mounting locations. RBE3 elements are used to connect all nodes at mounting locations to a single point at the center where the response is measured. Thus, it gives the average deflection/acceleration of the mounting location with respect to the spacecraft base. It helps the designer predict forces transmitted to any standard equipment or secondary component. The response output locations for displacements and accelerations in dynamic analyses are shown in Fig 6.15.

These locations constitute 19 mounts, each for electronic box types 1, 2, and 3, payload, fuel tank, and solar arrays.

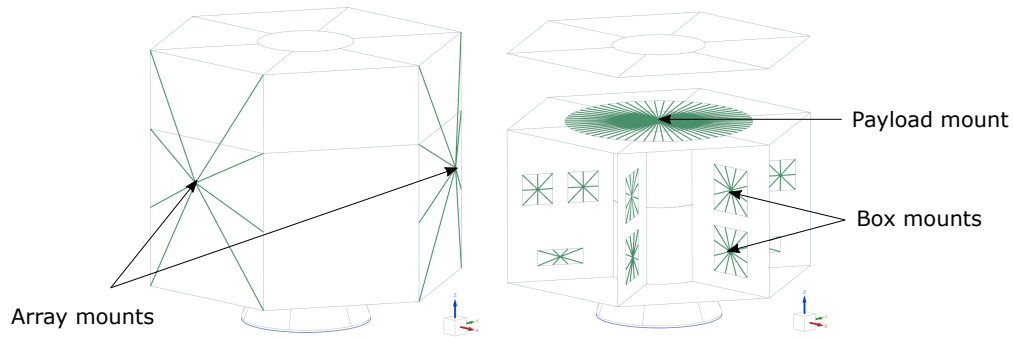

Figure 6.15: Response output locations of spacecraft for dynamic analyses.

6.1.3 Model Verification

The finite element model is verified using mesh convergence for structural and thermal responses. Normal modes analysis is run to determine the frequency range for extraction of modes having a total mass fraction greater than 0.9 in all six degrees of freedom. It is ensured that the strain energy density variation is small between adjacent elements and that the sum of reaction forces at the adapter is equal to the structure's weight when the structure is subjected to a unit acceleration load. The baseline spacecraft panel properties used for all verification studies are given in Table 6.5.

Table 6.5: Panel properties for baseline design.

Panel group	Ply thickness (mm)	Core thickness (mm)	Stacking Sequence
Cage	0.0762	25	$[(\pm 45)_{10}/(\mp 45)_{10}/\text{core}/(\pm 45)_{10}/(\mp 45)_{10}]$
Gusset	0.0762	25	$[(\pm 45)_{10}/(\mp 45)_{10}/\text{core}/(\pm 45)_{10}/(\mp 45)_{10}]$
Cylinder	0.0762	25	$[(\pm 45)_{10}/(\mp 45)_{10}/\text{core}/(\pm 45)_{10}/(\mp 45)_{10}]$
Base, mount	0.0762	25	$[(\pm 45)_{10}/(\mp 45)_{10}/\text{core}/(\pm 45)_{10}/(\mp 45)_{10}]$
Array	0.0762	25	$[0_2/90_2/0_4/90_2/0_2/\text{core}/0_2/90_2/0_4/90_2/0_2]$

Mass properties

The mass property breakdown with respect to different spacecraft components is given in Table 6.6. The gross weight of the spacecraft with baseline configuration is 798kg with the center of mass shown in Fig 6.16.

Table 6.6: Mass properties for baseline design of spacecraft.

Primary component	Count	Total mass (kg)
Lower cage panel	6	64.68
Upper cage panel	6	32.43
Gusset panels	6	45.41
Cylinder panels with cone	12	26.97
Base panel	6	25.04
Middle mounting panel	6	25.04
Upper mounting panel	7	28.09
Closeouts for cage panel	-	40.84
Closeouts for gusset panel	-	19.84
Closeouts for the base and mounting panel	-	38.72
Closeouts for cylinder panel	-	6.31
Spacecraft primary structure	-	≈ 354
Secondary component	**Count**	**Total mass (kg)**
Solar array panel	3	21.3
Electronic box type 1	4	62
Electronic box type 2	2	40.5
Electronic box type 3	8	89
Payload	1	101
Fuel tank & fuel	1	112
Spacecraft gross	-	≈ 798

Normal Modes

The structure is fixed at the payload adapter interface using the RBE2 element. Normal modes analysis is run to verify the finite element model constraints, get the fundamental frequency and compute modal effective mass fractions. The number of recovered modes, total modal effective mass fraction in each degree of freedom (DOF), and solver times are

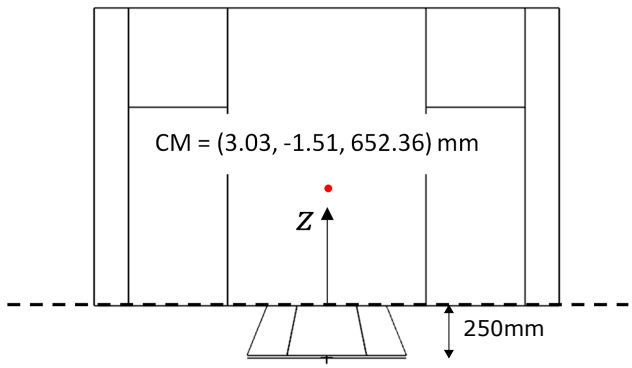

Figure 6.16: Schematic to show spacecraft center of mass for the baseline design.

tracked. From Fig 6.17, the range from 0 Hz to 300 Hz captures modes with a total mass fraction greater than 0.95 in all DOFs with only 24 modes. Even though this is the case, the modes related to the solar array and cage panels are missing in this range. These modes are crucial in vibroacoustic analysis as they are in direct contact with the surrounding fluid. Increasing the range to 600 Hz captures the array and cage modes as shown in Fig 6.19. Any further increase in the range captures only slightly more modal content despite of significant increase in the number of modes. Thus, the range between 0 Hz and 600 Hz is chosen in this study.

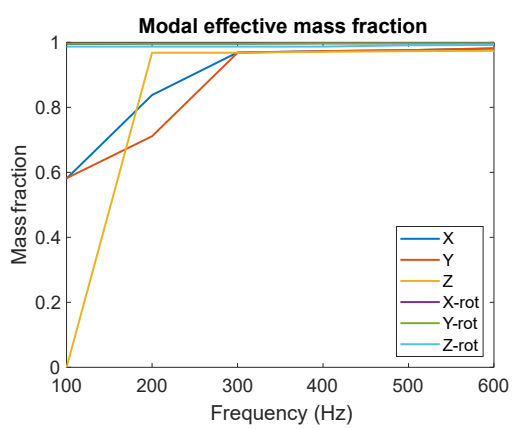

Figure 6.17: Effective mass fraction of normal modes in each degree of freedom from 0 Hz to 600 Hz.

From mass fractions in Table. 6.7, most of the mass is concentrated in low-frequency modes

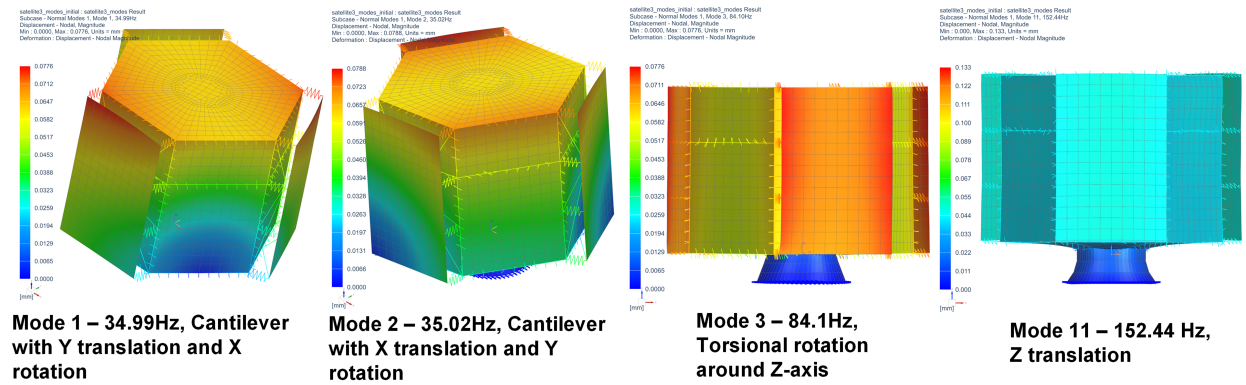

(a) Normal modes.

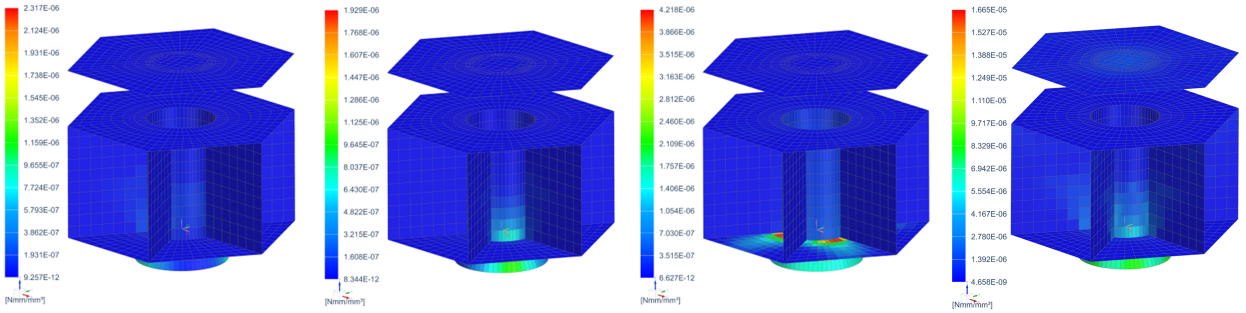

(b) Strain energy density in each mode.

Figure 6.18: Normal modes of spacecraft with maximum modal mass participation in each degree of freedom.

where the sine and random vibration can dominate the structural failure. Figure 6.18a shows modes with maximum mass participation factor in each degree of freedom. The finite element model is sufficiently constrained with the lowest fundamental frequency f_{cr}=34.99 Hz. Parallelization of SOL 103 is tried with shared memory and distributed memory parallel configurations using 2, 4, and 8 threads. The solver times are similar in each case, with each analysis taking around 4s. This is because geometric or frequency decomposition is more useful in large DOF models.

The element strain energy density for modes of interest is shown in Fig 6.18b. The first three modes have high-strain energy at the constrained location between the adapter cone and the cylinder, as expected. The mode with Z-translation results in the translation of solar arrays

Table 6.7: Modes with maximum mass participation in each degree of freedom.

DOF	X	Y	Z	X-rot	Y-rot	Z-rot
Mode	2	1	10	1	2	3
Frequency (Hz)	35.02	34.99	149.25	34.99	35.02	84.1
Mass fraction	0.46	0.46	0.81	0.78	0.78	0.98

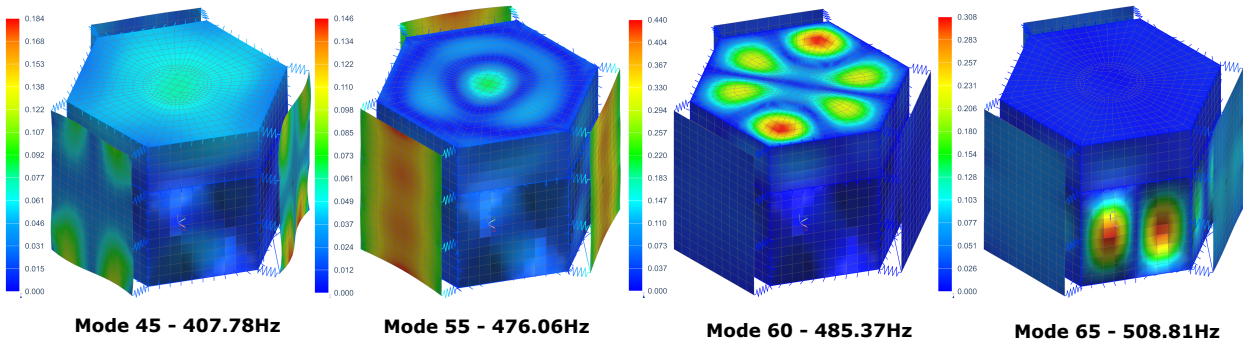

Figure 6.19: Spacecraft array and cage modes.

parallel to the Z-axis. Similar to the first three modes, the strain energy is high at eight locations where each array is constrained to the bus structure using CBUSH and CBEAM elements. The strain energy variation in the rest of the structure is very low, indicating that the mesh is sufficiently fine to capture structural responses at far-field locations. Note that capturing stresses accurately at the interface, constrained, or fastener locations requires multiscale modeling with joint strength analysis. The current work is limited to sizing the structure for global responses.

Unit Acceleration Load

A 1G acceleration is applied in the -Z direction as shown in Fig 6.20a. The corresponding deformations are shown in Fig 6.20b. The total reaction force in the Z direction measured at the spacecraft separation interface is equal to 7822.1 N, which is equivalent to the spacecraft weight at launch.

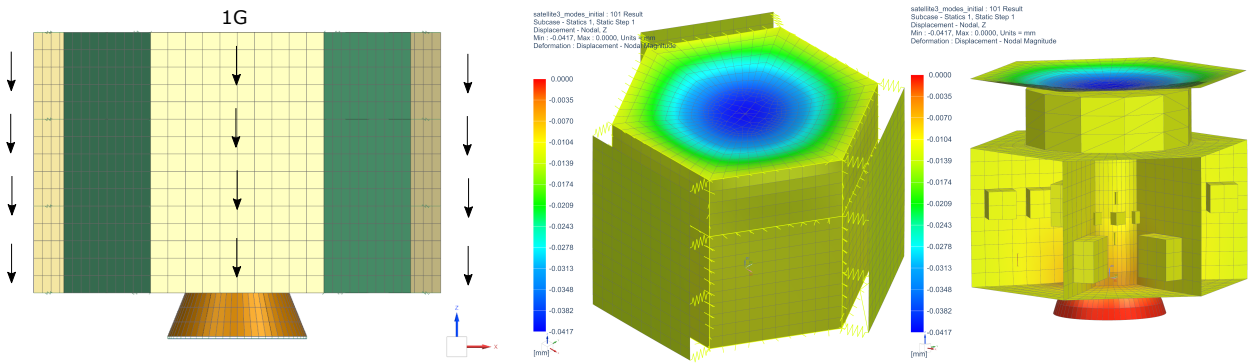

(a) Spacecraft with 1G load. (b) Spacecraft deformation under 1G load.

Figure 6.20: Spacecraft subjected to unit acceleration load.

Vibroacoustic Mesh Convergence

The optimal acoustic fluid mesh is found by performing a convergence study with different fluid element sizes. For the specific study, the vibroacoustic analysis is run with 16 processors using the *dmp* option in Nastran. The sound pressure level excitation is taken from SpaceX Falcon 9 launch vehicle user manual [7], and the PSD and RMS accelerations at equipment mounting locations are obtained for each analysis. From Fig 6.21, the acceleration response at all output locations is the same for acoustic element sizes of 150mm, 100mm, and 75mm. The response of mesh with 200mm element size is slightly different at certain frequencies, which also changes the RMS acceleration compared to that obtained from the other three meshes. This is seen from Table 6.8. From convergence results, an element size of 150 mm is considered for all vibroacoustic analyses. It is observed that the chance of excitation at array mounts is high at higher frequencies as the acoustic fluid is directly in contact with them.

h

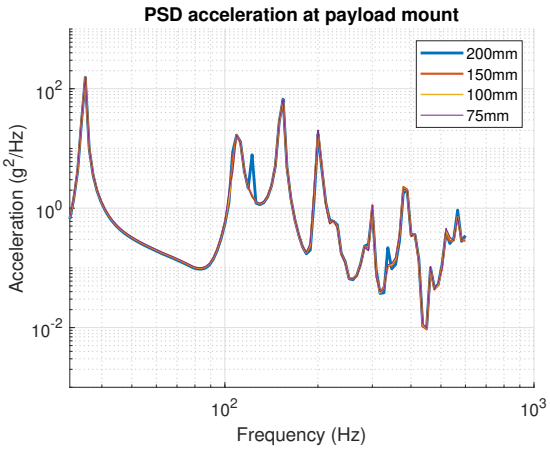

(a) Payload mount

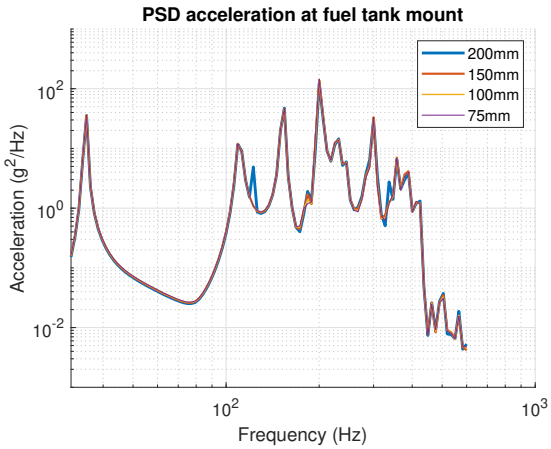

(b) Fuel tank mount

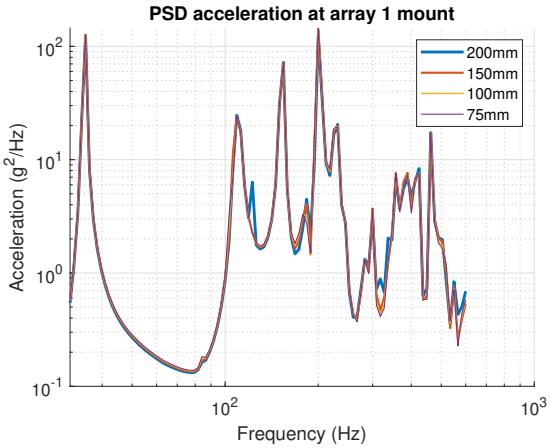

(c) Array 1 mount

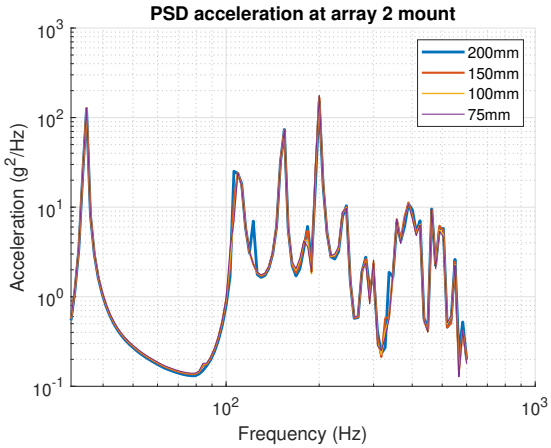

(d) Array 2 mount

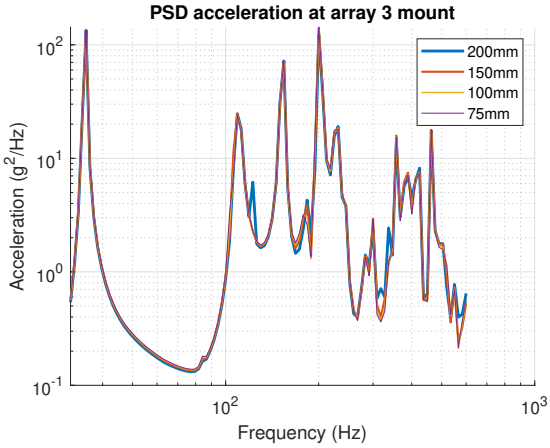

(e) Array 3 mount

Figure 6.21: Acceleration spectral density at mount locations with different element size acoustic meshes.

Table 6.8: RMS acceleration in Gs at different mount locations.

Element size (mm)	Payload	Fuel tank	Array 1	Array 2	Array 3
200	0.539	0.823	0.943	0.958	0.956
150	0.536	0.843	0.961	0.969	0.974
100	0.535	0.845	0.962	0.969	0.975
75	0.536	0.849	0.964	0.972	0.977

6.2 Spacecraft Analysis Setup

The static and dynamic load factors used in the multidisciplinary analysis are taken from SpaceX Falcon 9 launch vehicle user manual [7]. Multiple cases accounting for loads acting in different directions are considered based on the load factors.

6.2.1 Steady State Acceleration Loads

The response due to steady-state acceleration loads is analyzed using linear static and buckling analysis. The Falcon 9 manual gives load factors for spacecraft weight less than 4000 lbs as shown in Fig 6.22. Two extreme axial accelerations ($a_{z1} = 8$g and $a_{z2} = -4$g) are chosen as two primary cases. The lateral acceleration $a_{lateral}$ is resolved into components as shown in Fig 6.23 where $a_x = a_{lateral} \times \cos\phi$ and $a_y = a_{lateral} \times \sin\phi$.

Since the structure is asymmetrical, different loading subcases are built by spanning the angle ϕ by 360° in eight intervals. Thus, $\phi \in \{0°, 45°, 90°, \ldots, 315°\}$ to account for multiple loading combinations for the given load factors. The resolution of ϕ can be increased to provide greater accuracy but with an increase in computational time. Together with a_z, there are a total of 16 static load cases used in SOL 105.

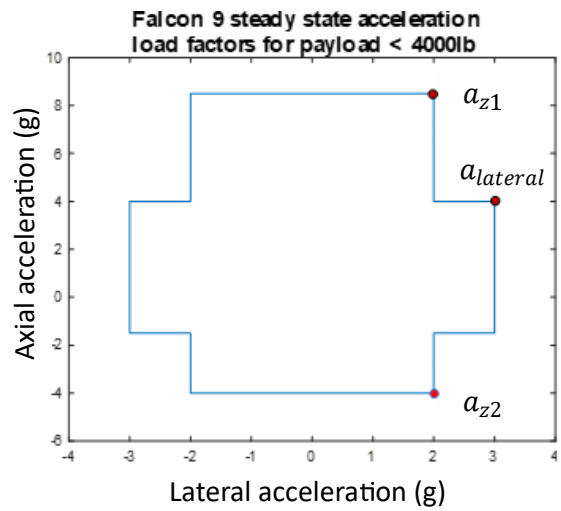

Figure 6.22: Steady state acceleration load factors. Source: [7].

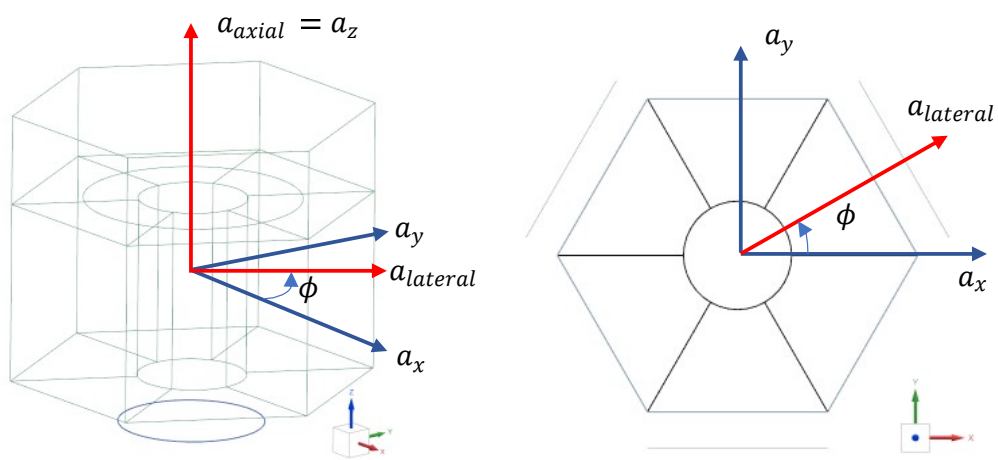

Figure 6.23: Component resolution for different load cases.

6.2.2 Sine and Random Loads

The load factors for sine and random vibration are given in Fig 6.24. Similar to steady-state acceleration, the lateral sine vibration is resolved into two components using $\phi = \{0°, 45°, 90°, 135°\}$. It results in 4 load cases each for SOL 111 frequency response analysis and SOL 111 random analysis. For random analysis, 1g acceleration is applied in each direction and the ASD is defined in the random subcase. The frequency response output is defined using the FREQ4 card that spreads the output frequencies near the modal fre-

quencies. Three evenly spaced frequencies with a spread of 0.1 are defined for each modal frequency between 0 Hz and 100 Hz for sine vibration, whereas a frequency range of 0 Hz - 400 Hz is used for random vibration.

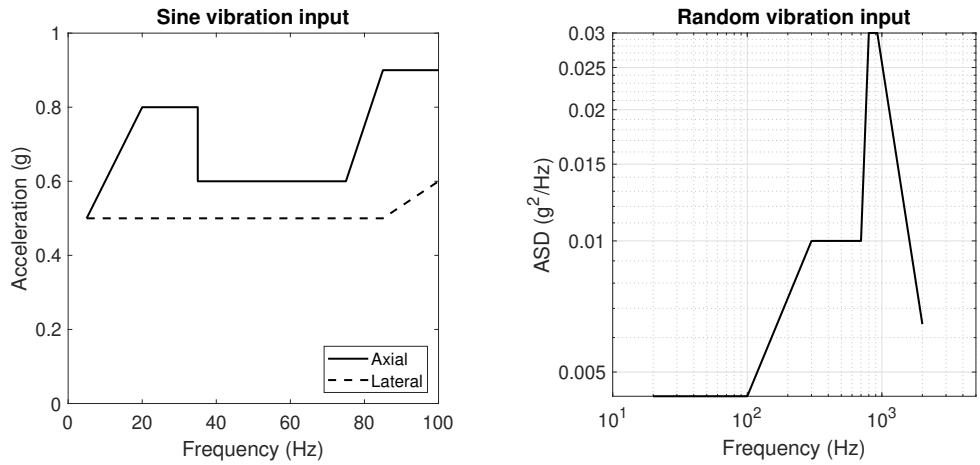

(a) (b)

Figure 6.24: Falcon 9 load factors for sine and random vibration analysis. Source: [7].

6.2.3 Shock Loads

The shock response spectrum from Falcon 9 user manual is synthesized into three acceleration time histories as shown in Fig 6.25. A third-party Matlab toolbox by *VibrationData* [99] is used for this purpose. The time histories are used as excitations in the axial direction in SOL 112. A rule of thumb is to include a minimum of 20 time steps per highest frequency of interest for reasonable accuracy. The highest frequency of interest defined from the modal solution is 600 Hz. Thus, a step time of 8.33E-5s is used with 7500 steps to get the transient response.

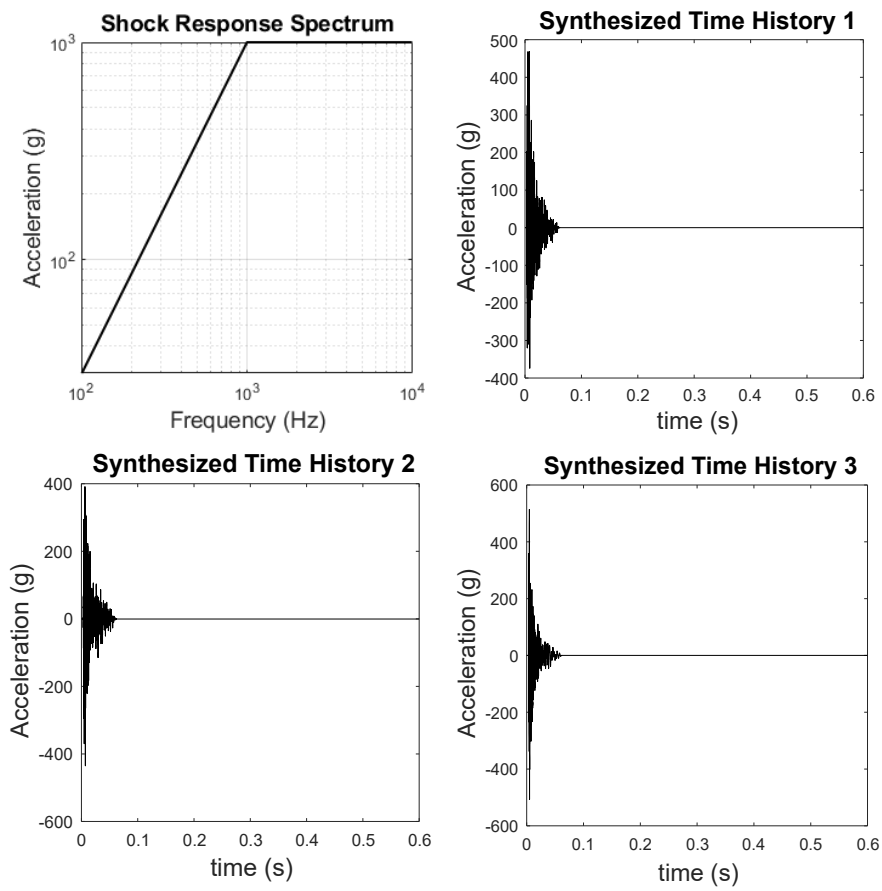

Figure 6.25: Acceleration shock response spectrum [7] and synthesized time histories.

6.2.4 Acoustic Loads

For the vibroacoustic analysis, 50 randomly distributed plane waves are used to simulate a diffused acoustic field as shown in Fig 6.26a. The sound pressure level from Falcon 9 manual is converted into sound pressure PSD using Eqn. (6.1)

$$p_{PSD} = 10^{\frac{SPL}{10}} \left(\frac{p_{ref}^2}{\Delta f} \right) \tag{6.1}$$

where $p_{ref} = 20\mu Pa$ and Δf is the bandwidth. A logarithmic sweep between 31.5 Hz and 600 Hz with an octave spacing of 1/24 is used to define 102 output frequencies. For a model

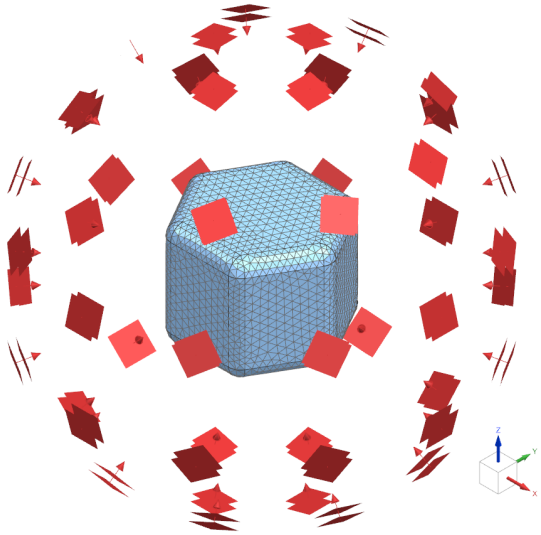

(a) Diffused acoustic field simulation with randomly distributed plane waves.

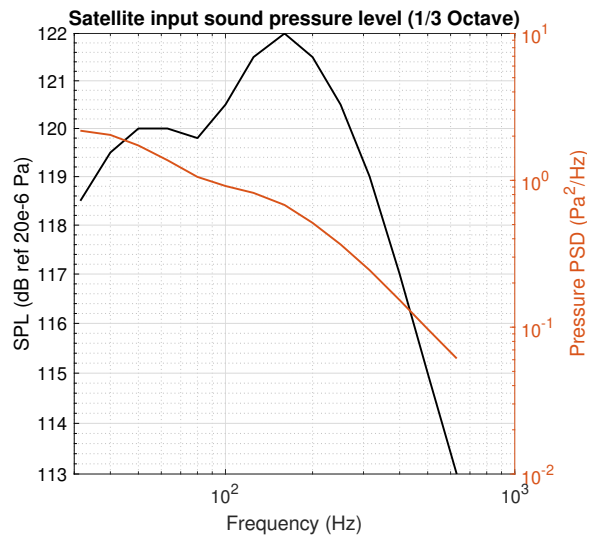

(b) Launch vehicle sound pressure level. Source: [7].

Figure 6.26: Vibroacoustic load model using distributed plane waves and sound pressure level.

with fewer structural DOFs, the computation of fluid modes takes significantly longer than that for structural modes. Using SOL 108 instead of SOL 111 is more efficient in such cases.

6.3 Spacecraft Optimization with Direct Method

6.3.1 Optimization Problem Formulation for Direct Method

The spacecraft structure is optimized using the SHERPA algorithm for minimum weight by determining optimal sizing parameters such as ply fiber orientations of face sheets, the number of plies in a face sheet, and thickness of the honeycomb core for individual panel groups as shown in Fig 6.27. The thickness of each ply is fixed at 0.0762 mm. Since a balanced and symmetric layup is used for most applications, each positively oriented ply is followed by a negatively oriented ply of the same fiber angle. The number of design variables for fiber

orientations is reduced using face sheets and laminate symmetries. Thus, every addition or removal of ply in the optimization corresponds to the addition or subtraction of 4 plies in a face sheet, respectively. As the number of plies for each panel group is a design variable, the maximum number of plies N_{max} must be predefined. The number of fiber orientation design variables depends on N_{max}.

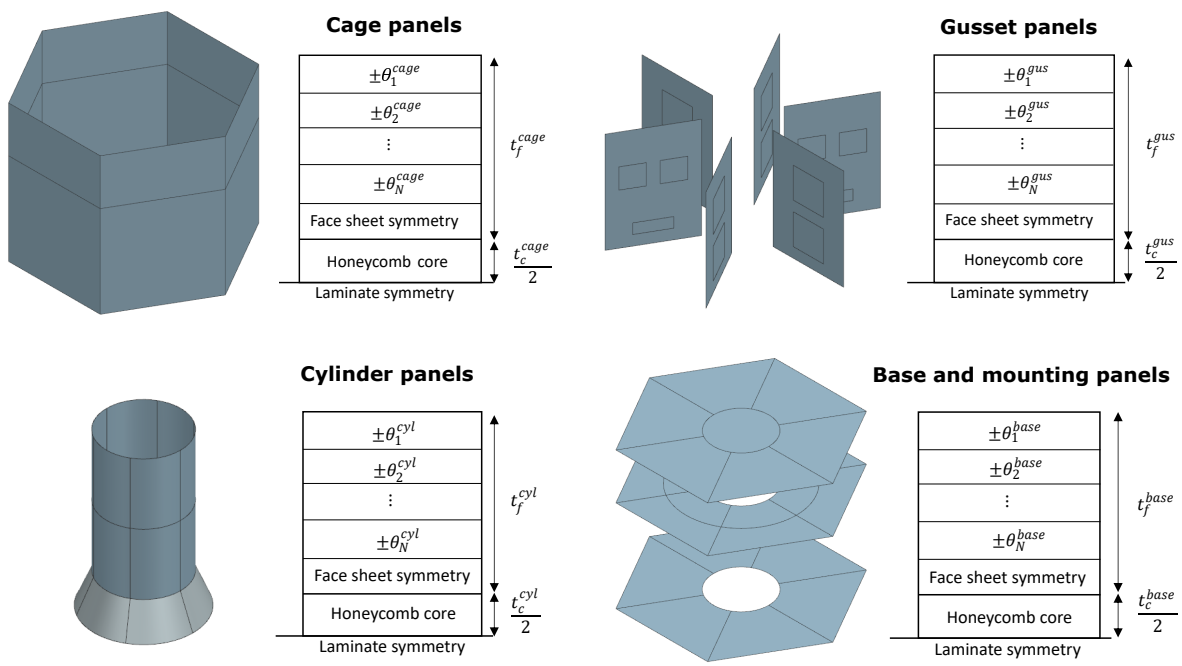

Figure 6.27: Design variable description for spacecraft sizing optimization.

Apart from panel variables, the closeout cross-sectional dimensions are used as dependent variables as shown in Fig 6.3. In the current optimization, N_{max} is set to 10 for all panels, which corresponds to 40 plies per face sheet. This results in 10 discrete fiber orientation design variables and one continuous hexagonal core thickness variable per face sheet per panel group. Thus, the optimization problem has a total of 40 discrete fiber orientation variables, 4 continuous thickness variables, and 4 integer variables for the number of plies.

The description of all constraints, along with their limiting values, is given in Table 6.9. The responses are kept purely structural. The minimum frequency of the spacecraft with

Table 6.9: Spacecraft optimization constraints.

Constraint	Notation	Limits
Critical buckling load factor (mechanical, thermal)	λ_{cr}	≥ 0.67
Fundamental frequency in each degree of freedom	f_{cr}	≥ 20 Hz
Tsai-Wu failure index (mechanical, thermal)	F_{cr}	≤ 0.67
Deformation due to static loads (mechanical, thermal)	δ_{cr}^{stat}	≤ 20 mm
Deformation due to dynamic loads	δ_{cr}^{dyn}	≤ 20 mm
Acceleration due to sine loads	a_{cr}^{sine}	≤ 10 g
RMS acceleration due to random loads	a_{cr}^{rand}	≤ 10 g
PSD displacements due to random loads	δ_{PSD}	≤ 400 mm^2/Hz
ASD due to random loads	a_{PSD}	≤ 100 g^2/Hz
Acceleration due to shock loads	a_{cr}^{shock}	≤ 1.6 g/Hz $\times f$
Wrinkling	t_f^j	$\geq 0.04(2t_f^j + t_c^j)$
Fastener (CBUSH) failure index (mechanical, thermal)	F_{fast}	≤ 1

modes having a mass fraction greater than 0.35 in each of the six DOFs must be greater than 20 Hz. Ply failure indices using the Tsai Wu criterion, buckling load factor, and panel deformations are used as static failure metrics. In the case of dynamic analysis, accelerations and displacements at secondary component mounting locations are constrained to limit their transmission to sensitive equipment. The acceleration SRS for shock excitations is constrained using values defined in [97]. A safety index of 1.5 is used in the static analysis and a 2.5% critical damping is used in dynamic analyses. The optimization problem takes the form:

$$
\begin{array}{lll}
\textbf{Minimize:} & \text{Mass } W(N^j) & \\
\textbf{Subject to:} & g(\theta_k^j, N^j, t_c^j) \leq 0 & \\
 & \theta_k^j \in \{0°, 45°, 90°\} & j \in \{\text{cage, gus, cyl, base}\} \\
 & 1 \leq N^j \leq 10 & k = 1, \ldots, N_{max}^j \\
 & 12.5 \text{ mm} \leq t_c^j \leq 50 \text{ mm} &
\end{array}
$$

Sandwich panels are prone to local instabilities like wrinkling and dimpling. Wrinkling is dominant in panels with very thin face sheets and thick cores. Without considering wrinkling failure, the optimization can lead to designs with increased core thickness to increase the bending rigidity and stiffness. Since the core has a much lower density than face sheets,

the mass penalty for increasing the core thickness is low. It results in panels with very thin face sheets and thick cores susceptible to wrinkling. To add wrinkling constraint using the global response of the structure, the ratio of face sheet thickness to total panel thickness is restricted as given in [100].

Failure at fastener locations is common in aerospace structures. Accurate prediction of failure response at such locations requires local high-fidelity simulations that are computationally expensive. Instead, a failure criterion is used per NASA Technical Standard 5020B [101] to constrain forces in CBUSH elements. As per the standard, the fastener failure index F_{fast} due to combined multi-axial loading is given as

$$\left(\frac{P_{su}}{P_{su-allow}}\right)^{2.5} + \left(\frac{P_{tu}}{P_{tu-allow}} + \frac{f_{bu}}{F_{tu}}\right)^{1.5} \leq 1 \tag{6.2}$$

where, P_{su} is the induced shear load per shear plane, P_{tu} is the induced tensile load, f_{bu} is the induced bending stress, F_{tu} is the ultimate allowable tensile stress and $P_{tu-allow}$ is the ultimate allowable tensile load. $P_{su-allow} = \frac{\pi d^2 F_{su}}{4}$ is the allowable ultimate shear load with F_{su} as the ultimate shear strength. The quantities P_{su}, P_{tu} and f_{bu} can be found from CBUSH forces.

6.3.2 MSADO Results with Direct Method

The optimization is run for 8000 design evaluations with 10 different starting points. The results for two extreme starting points (maximum and minimum possible mass) are shown here. Intel Xeon W2264 having 12 cores and 24 threads, is used with 10 designs running in parallel on 10 cores. Each module in the multidisciplinary analysis is run serially on a single core. Figures 6.28 and 6.29 show design history plots for the objective function and responses at or near their constraint values. The optimizer initially tries to attain a feasible

design by increasing the design variable values, thereby increasing the mass. The SHERPA algorithm spends time exploring the design space and learning about key parameters that can have a higher impact on the objectives and constraints.

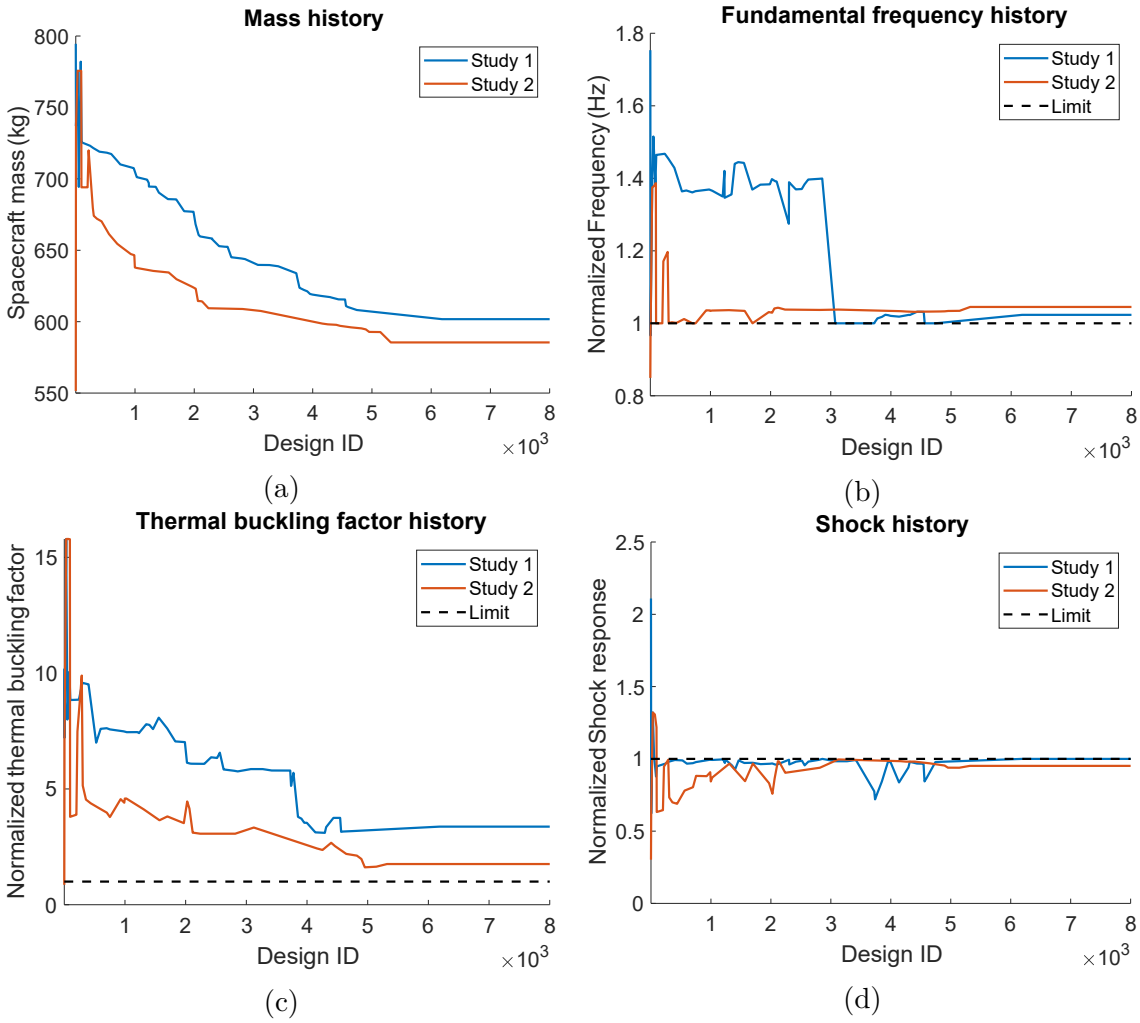

Figure 6.28: Design history plot for objective, frequency, shock acceleration, and thermal buckling factor.

The two studies converge at different masses from Fig 6.28a. This is due to the probabilistic nature of SHERPA, which seeks the global optimum with random perturbations in algorithm parameters. Also, the presence of many local optima may cause the optimizer to get stuck in one of the minima. Thus, the best value among multiple optimization runs must be chosen.

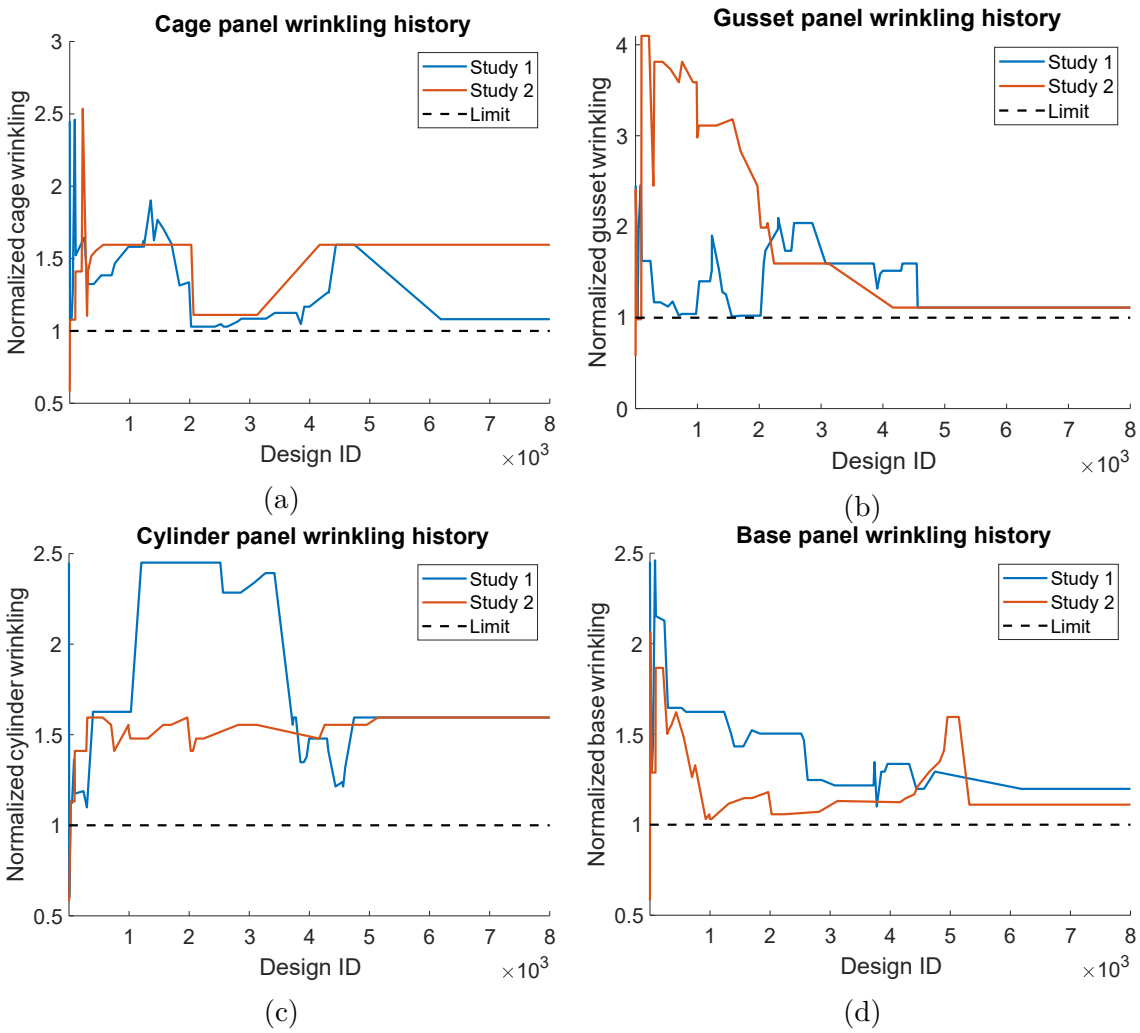

Figure 6.29: Design history plot for panel wrinkling constraints.

Study 2 gives the best mass value of 585.49 kg while satisfying all constraints, which is $\approx$ 26.6% reduction from the baseline design. The constraints at or near the limit in this study are given in Table 6.10.

Table 6.10: Constraints that are at or near the limit from study 1.

Constraint	Normalized value	True value
SRS (Array mount @ 100 Hz)	$0.95 \leq 1$	152 g $\leq$ 160 g @100 Hz
Fundamental frequency	$1.045 \geq 1$	20.9 Hz $\geq$ 20 Hz
Wrinkling	$1.11 \geq 1$	$0.044 \geq 0.04$
Thermal buckling factor	$2.63 \geq 1.5$	$2.63 \geq 1.5$

The shock response constraint is at its limit, followed by the fundamental frequency and panel wrinkling. Reducing the number of plies is the fastest way for the optimizer to reduce mass, but the wrinkling constraint also forces the core thickness not to keep on increasing. Recall that increasing the core thickness increases the bending stiffness, which is crucial for satisfying stiffness-based constraints like maximum bending stresses, deformations, accelerations, buckling load factors, and frequencies. Thus, the wrinkling constraint increases the number of plies to increase face sheet thickness. The critical buckling load factor across all mechanical load cases is 69.43. Since none of the strength-based constraints are close to their limits, the design is purely driven by the structure's stiffness.

The variation of the number of plies and honeycomb core thickness for each panel group is shown in Fig 6.30. The optimization in study 1 is started with $N^{cage} = N^{gus} = N^{cyl} = N^{base} = 10$, i.e., 40 plies per face sheet, and study 2 is started with $N^{cage} = N^{gus} = N^{cyl} = N^{base} = 10$. The minimum is attained at $N^{cage} = N^{cyl} = 3$ (12 plies per face sheet) and $N^{gus} = N^{base} = 2$ (8 plies per face sheet). Similarly, the honeycomb core thickness attains a minimum of 12.5 mm for all panels. The optimal number of balanced symmetric plies per face sheet results in optimal fiber orientations per panel face sheet given in Table 6.11.

Table 6.11: Optimal face sheet stacking sequences.

Panel	Stacking
Cage	$[90_2/\pm 45/0_2]_S$
Gusset	$[0_4]_S$
Cylinder	$[\pm 45/90_4]_S$
Base & mount	$[\pm 45/0_2]_S$

The baseline and optimal designs are compared by comparing normal modes and strain energy densities as shown in Figs 6.32 and 6.33. Modes 1, 2 and 3 in the optimal design correspond to the same DOFs as in the baseline design. In the optimal design, the modal frequencies are grouped closer than the baseline design indicating a higher modal density.

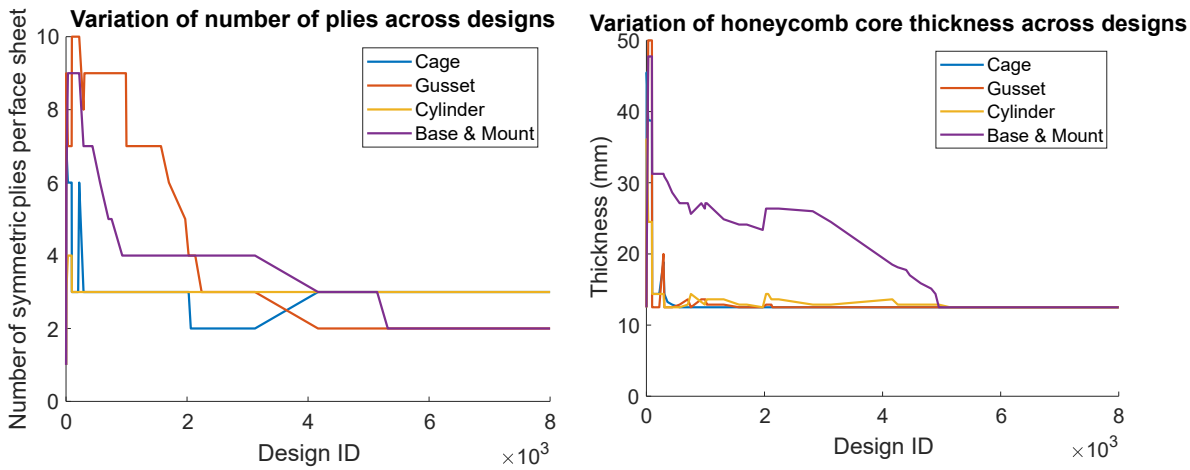

(a) (b)

Figure 6.30: Design variable history of study 2 for the number of plies and honeycomb core thickness of each panel group.

The mode having maximum mass participation in Z-translation is switched from mode 11 to mode 5 in the optimal design. The strain energy densities at the base, gusset and cylinder interface are also reduced, especially for torsional rotation and Z-translation modes.

The shock response is compared in Fig 6.34. The baseline design, despite having high mass, is prone to shock damage in the electronic boxes, payload, and solar arrays at an excitation frequency of around 160 Hz. The mode corresponding to 160 Hz is translational in the Z direction. The optimization significantly reduces the response at this frequency by shifting the modes with relatively high mass factions in Z translation to lower frequencies. As a result, the modal density in the optimal design is higher than the baseline design, as shown in Fig 6.35.

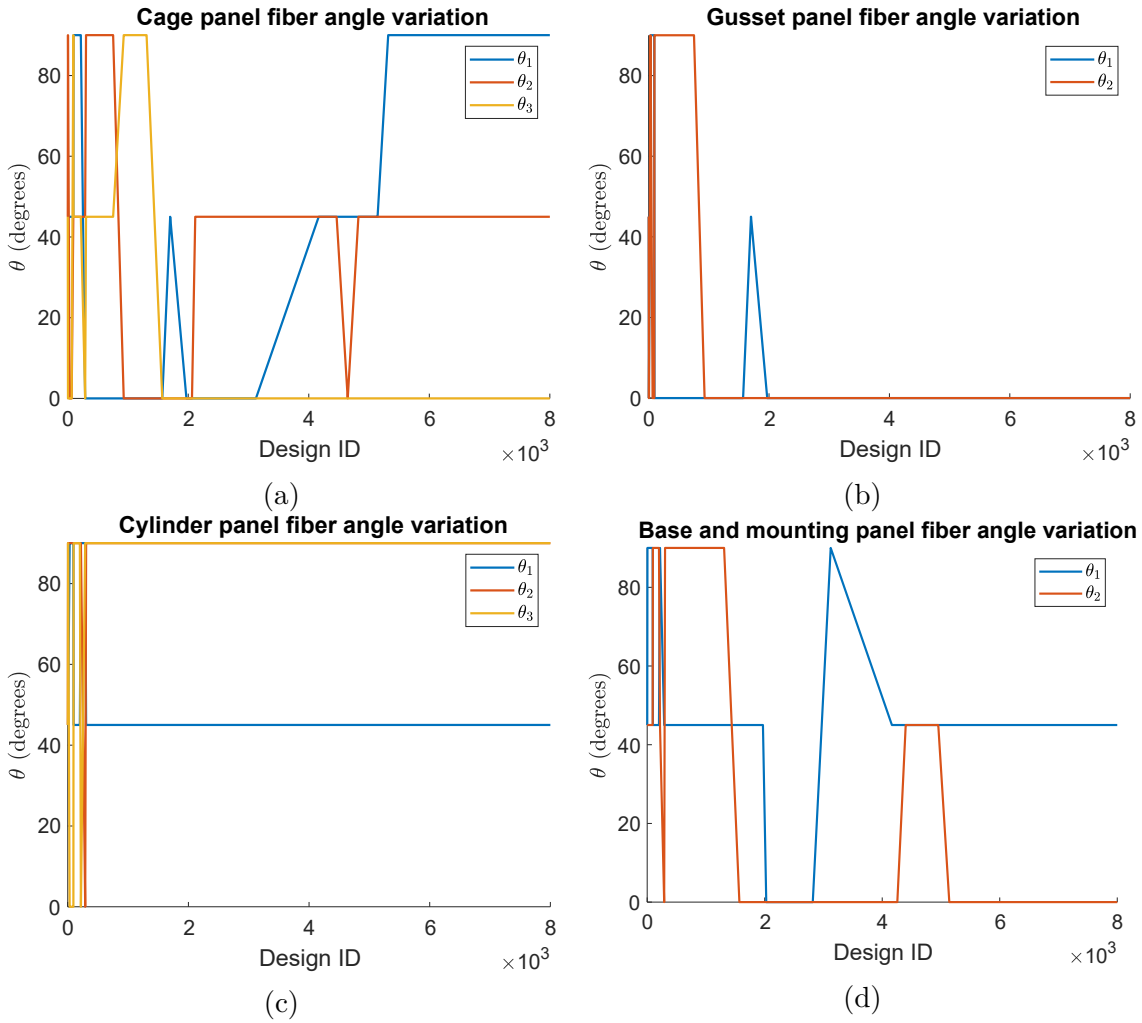

Figure 6.31: Design variable history of study 1 for panel fiber orientations.

6.4 Spacecraft Optimization with Lamination Parameters and Mixed Integer Programming

The formulations required to enable the use of lamination parameter optimization in the MSADO framework are given in this section. The MSADO framework with lamination parameters is then used to optimize the spacecraft model to demonstrate performance improvements over the direct method.

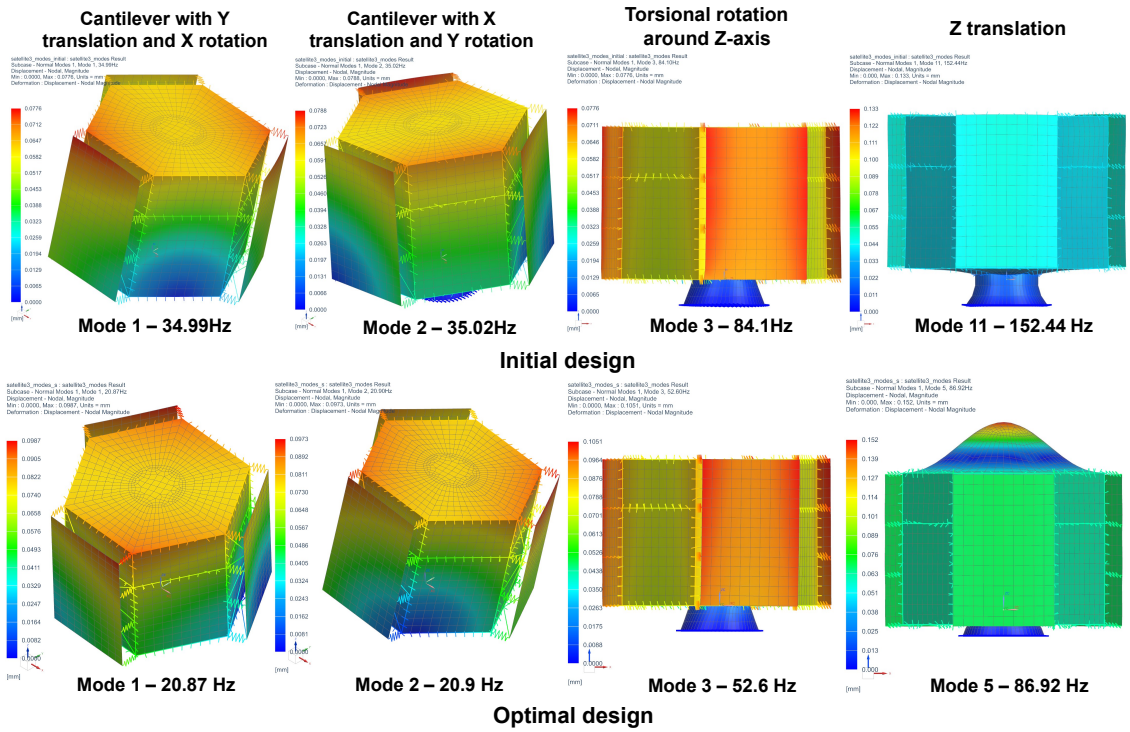

Figure 6.32: Comparison of normal modes between baseline and optimal design.

6.4.1 Extension of Lamination Parameters to Thermal Analysis

The MSADO framework includes heat transfer and thermal stress analysis, where the thermal conductivity and coefficient of thermal expansion of composite panels are a function of ply fiber orientations. To apply the lamination parameter optimization technique in a multidisciplinary thermal-structural environment, the lamination parameters must be independently linked to thermal conductivities and the coefficient of thermal expansions, i.e., without the inclusion of ply fiber orientations $\hat{\theta}$.

Lamination Parameters and Thermal Conductivity

Suppose the lamina thermal conductivities in 1,2 and 3 directions are given as κ_1, κ_2, and κ_3, respectively. The thermal conductivities in material coordinates must be transformed

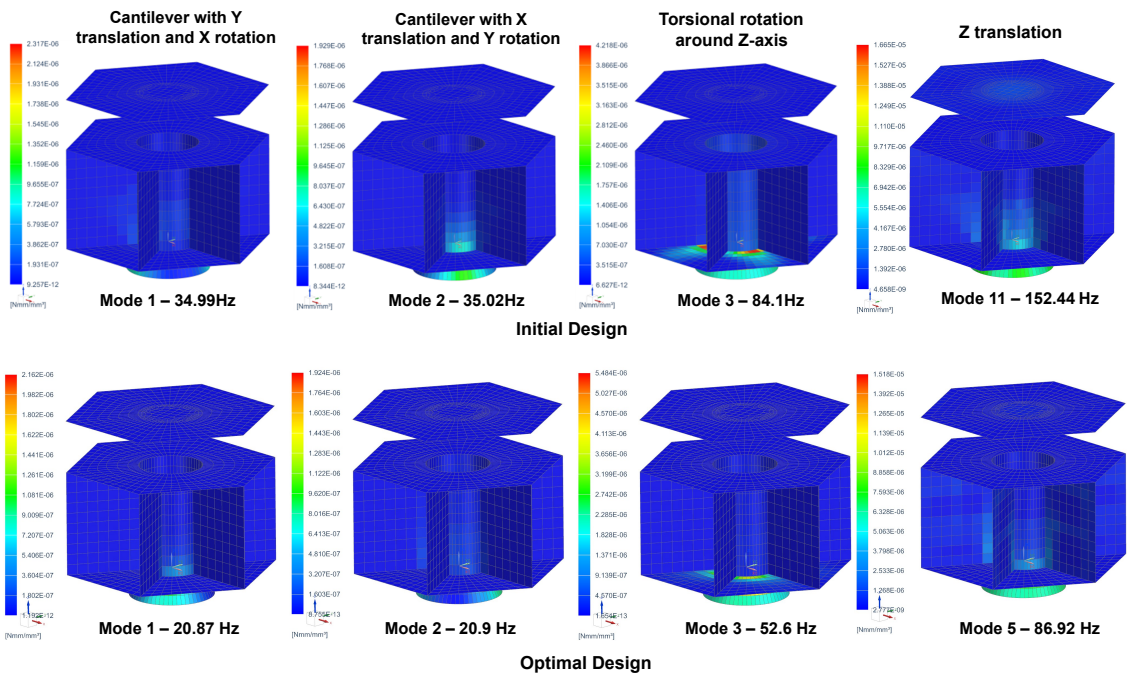

Figure 6.33: Comparison of strain energy densities between baseline and optimal design corresponding to normal modes in 6.32.

to global coordinates to find the thermal conductivity of the equivalent shell. Let thermal conductivities of ply k in global coordinates be κ_{kx}, κ_{ky}, and κ_{kz} in x, y, and z directions, respectively. The coordinate transformations are given as in Eqn. (6.3).

$$\begin{aligned} \kappa_{kx} &= \kappa_1 \cos^2 \hat{\theta}_k + \kappa_2 \sin^2 \hat{\theta}_k \\ \kappa_{ky} &= \kappa_1 \sin^2 \hat{\theta}_k + \kappa_2 \cos^2 \hat{\theta}_k \\ \kappa_{kz} &= \kappa_3 \end{aligned} \tag{6.3}$$

The equivalent thermal conductivity of the laminate can be found using Eqn. (6.4) with thermal resistance in series and parallel. κ_x and κ_y are equivalent laminate conductivities in x and y directions, respectively. They are obtained by using a thermal resistance configuration in parallel. The laminate conductivity κ_z is obtained using thermal resistance configuration in series and is equal to the lamina conductivity in the stack direction, assuming the material

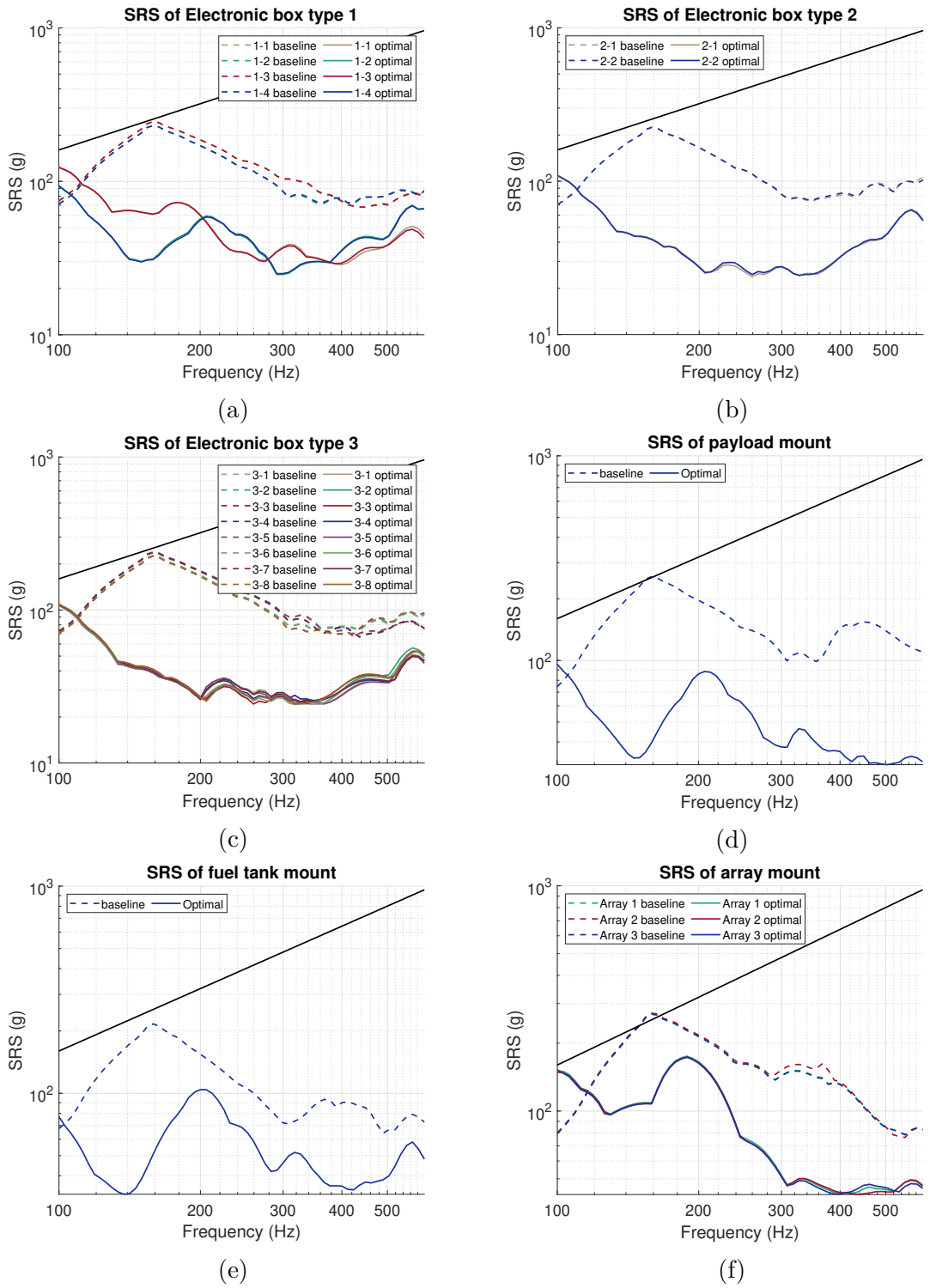

Figure 6.34: Shock response comparison between baseline and optimal design.

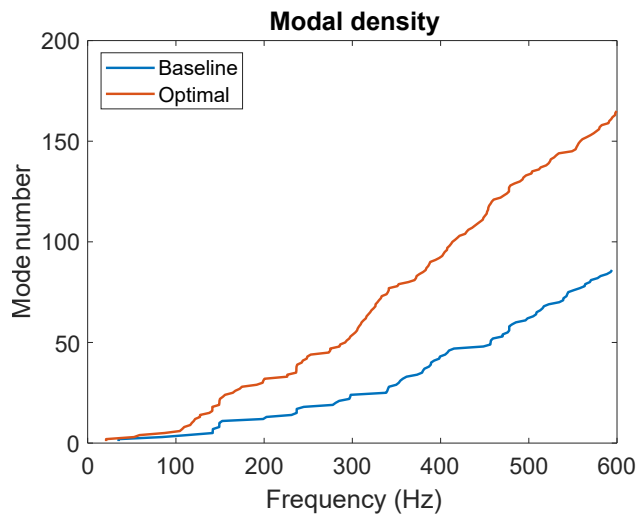

Figure 6.35: Spacecraft modal density comparison.

remains constant.

$$\kappa_x = \frac{\sum_{k=1}^{N} \left(\kappa_{kx}\hat{t}_k\right)}{\sum_{k=1}^{N} \hat{t}_k}$$
$$\kappa_y = \frac{\sum_{k=1}^{N} \left(\kappa_{ky}\hat{t}_k\right)}{\sum_{k=1}^{N} \hat{t}_k} \tag{6.4}$$
$$\kappa_z = \frac{\sum_{k=1}^{N} \hat{t}_k}{\sum_{k=1}^{N} \frac{\hat{t}_k}{\kappa_{kz}}}$$

The equivalent shell conductivities are functions of ply fiber orientations and thickness similar to lamination parameters. Thus, it can be intuitively said that there is a relationship between lamination parameter v_{1A} and κ_x, κ_y, and κ_z. The lamination parameter v_{1A} can be rewritten using trigonometric identities as shown in Eqn. (6.5). By rearranging the terms and using $\sum \hat{t}_k = h$, the expression for $\cos^2 \hat{\theta}_k$ in terms of lamination parameter v_{1A} can be found.

Similarly, using a second trigonometric identity for $\cos 2\theta$, the expression for $\sin^2 \hat{\theta}_k$ in terms of lamination parameters is evaluated as shown in Eqn. (6.6).

$$v_{1A}h = \sum_{k=1}^{N} \hat{t}_k \cos 2\hat{\theta}_k = \sum_{k=1}^{N} \hat{t}_k (2\cos^2 \hat{\theta}_k - 1) \tag{6.5}$$

$$\begin{aligned} \sum_{k=1}^{N} \hat{t}_k \cos^2 \hat{\theta}_k &= \frac{h}{2}(1 + v_{1A}) \\ \sum_{k=1}^{N} \hat{t}_k \sin^2 \hat{\theta}_k &= \frac{h}{2}(1 - v_{1A}) \end{aligned} \tag{6.6}$$

From Eqns. (6.3), (6.4) and (6.6), the equivalent thermal conductivities as functions of a single lamination parameter are given in Eqn. (6.7).

$$\begin{aligned} \kappa_x &= \frac{1}{2}\left[\kappa_1(1 + v_{1A}) + \kappa_2(1 - v_{1A})\right] \\ \kappa_y &= \frac{1}{2}\left[\kappa_1(1 - v_{1A}) + \kappa_2(1 + v_{1A})\right] \\ \kappa_z &= \kappa_3 \end{aligned} \tag{6.7}$$

Lamination Parameters and Coefficient of Thermal Expansion

The in-plane lamina longitudinal and transverse coefficient of thermal expansions (CTEs) are given as α_1 and α_2, respectively. Miller [102] used material invariants in evaluating shell equivalent properties of the CTEs with lamination parameters. The material invariants for thermo-elastic analysis are presented in Eqn. (6.8).

$$\begin{Bmatrix} U_1^T \\ U_2^T \end{Bmatrix} = \begin{bmatrix} \alpha_1 & \alpha_1 + \alpha_2 & \alpha_2 \\ \alpha_1 & -\alpha_1 + \alpha_2 & -\alpha_2 \end{bmatrix} \begin{Bmatrix} Q_{11} \\ Q_{12} \\ Q_{22} \end{Bmatrix} \tag{6.8}$$

Here, Q_{11}, Q_{12} and Q_{22} are reduced stiffnesses of the lamina. U_1^T and U_2^T are the thermo-elastic invariants. The shell equivalent CTEs can be computed as shown in Eqn. (6.9). The equivalent membrane CTEs are denoted as α_x^A, α_y^A and α_{xy}^A whereas the equivalent bending CTEs are α_x^D, α_y^D and α_{xy}^D. Since A and D are purely functions of lamination parameters, the equations for equivalent CTEs can be used in lamination parameter optimization with thermal-structural analysis.

$$\begin{aligned}
\begin{Bmatrix} \alpha_x^A \\ \alpha_y^A \\ \alpha_{xy}^A \end{Bmatrix} &= \frac{h}{2}[A]^{-1} \begin{bmatrix} 1 & v_{1A} \\ 1 & -v_{1A} \\ 0 & v_{2A} \end{bmatrix} \begin{Bmatrix} U_1^T \\ U_2^T \end{Bmatrix} \\
\begin{Bmatrix} \alpha_x^D \\ \alpha_y^D \\ \alpha_{xy}^D \end{Bmatrix} &= \frac{h^3}{24}[D]^{-1} \begin{bmatrix} 1 & v_{1D} \\ 1 & -v_{1D} \\ 0 & v_{2D} \end{bmatrix} \begin{Bmatrix} U_1^T \\ U_2^T \end{Bmatrix}
\end{aligned} \tag{6.9}$$

With Eqns. (6.7) and (6.9), a multidisciplinary analysis with structural and thermal disciplines can be performed with lamination parameters alone.

6.4.2 Analysis of Sandwich Panels with Lamination Parameters

Optimizing sandwich composite panels involves finding the optimal core thickness in addition to the face sheet thickness. When the ply level information is available, the extensional and bending stiffness computation of sandwich construction follows the same method as that of a standard unidirectional composite laminate by modeling the core as a separate ply that is sandwiched between face sheet plies. Suppose lamination parameters are to be used instead. In that case, the bending stiffness of the sandwich panel must be computed as a function of the bending stiffness of the two face sheets together (without the core) and the bending

stiffness of the core. The offset in the bending stiffness of face sheets due to the addition of the core must also be accounted for in such cases, as shown by Silva and Meddaikar [103].

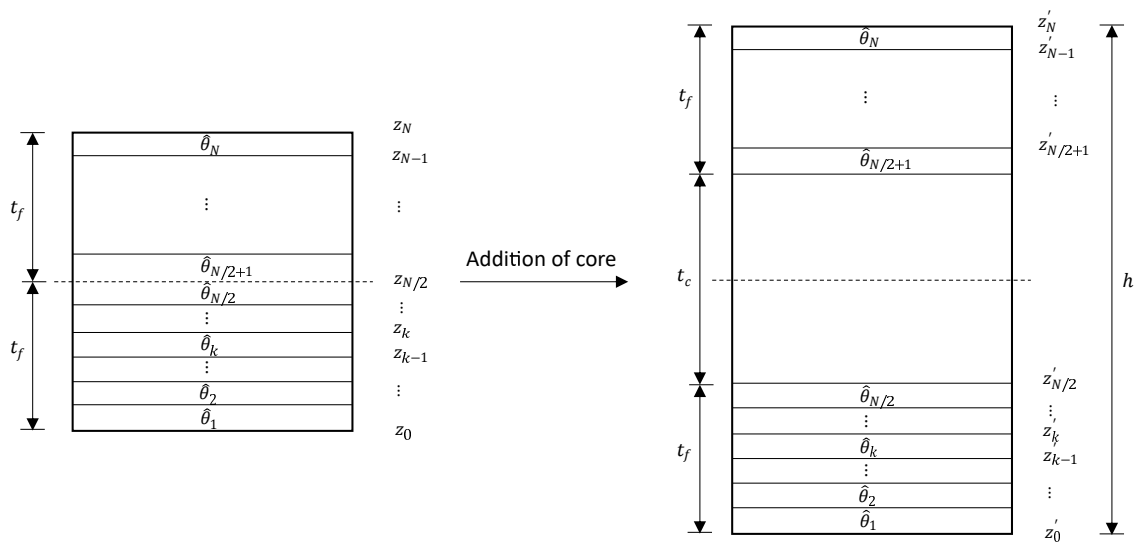

Figure 6.36: Composite panel construction without and with honeycomb core.

For laminate configurations shown in Fig 6.36, let A_f, B_f and D_f be the stiffnesses for the panel without the core (left). A_c, B_c and D_c are the core stiffnesses, and A, B and D are the stiffness of the entire sandwich panel (right). Adding a core of thickness t_c at the center changes the z-coordinate values of face sheet plies such that $z'_k = z_k - t_c/2$ for $k \in [0, \ldots, N/2]$ and $z'_k = z_k + t_c/2$ for $k \in [N/2, \ldots, N]$. After substituting the new coordinate translations into stiffness expressions, the contribution of face sheet stiffnesses having a symmetric configuration with the offset can be written as

$$\begin{aligned} A' &= A_f \\ D' &= D_f - t_c B_f^u + \frac{1}{2} t_c^2 A_f \end{aligned} \tag{6.10}$$

where B_f^u is the upper half of B_f. Note that if the total sandwich stiffness is written in terms of face sheet and core stiffnesses, the offset t_c results in the upper part of B_f

matrix that must be included in the offset stiffness terms. The offset method is crucial for lamination parameter formulation as the face sheets can be designed directly using A_f and D_f as functions of lamination parameters. Instead of computing B_f, an approximation is proposed in [103] where $B_f^u = 1/2(A_f + D_f)$ provides a reasonable estimate for evaluating D'. The total stiffness of the sandwich panel can be calculated using Eqns (6.10) and (6.11) as

$$\begin{aligned} A &= A_c + A' \\ D &= D_c + D' \end{aligned} \tag{6.11}$$

Since the sandwich stiffness expressions in Eqn (6.11) are explicitly composed of face sheet and core stiffnesses, the lamination parameters of face sheets can be used as design variables along with face sheet and core thickness variables for sandwich panel optimization.

6.4.3 Optimization Problem Formulation with Lamination Parameters and Mixed Integer Programming

The design variable description for the spacecraft model is shown in Fig 6.37. The lamination parameters of individual panel groups $\mathbf{v}^j$, the face sheet thickness t_c^j and the core thicknesses t_f^j are considered as design variables in the step 1 optimization with MSADO framework. Since a balanced symmetric configuration is assumed for ply stacks, the lamination parameters corresponding to coupling terms are assumed to be 0. The vector of lamination parameter can be written as $\mathbf{v}^j = [v_{1A}^j, v_{3A}^j, v_{1D}^j, v_{3D}^j]$ where $j \in \{\text{cage, gus, cyl, base}\}$. The feasible region of lamination parameters is established using a set of constraints and linear scaling maps as shown by Macquart et al. [84]. The resulting optimization problem for lamination parameters becomes

Step 1: Lamination parameter optimization.

$$
\begin{aligned}
&\textbf{Minimize:} && W(t_f^j, t_c^j) \\
&\textbf{Subject to:} && g(t_f^j, t_c^j, \mathbf{v}^j) \leq 0 \\
& && -1 \leq \mathbf{v}^j \leq 1 \\
& && 12.5 \leq t_c^j \leq 50 \text{ (mm)} \\
& && 0.1524 \leq t_f^j \leq 3.04 \text{ (mm)}
\end{aligned}
$$

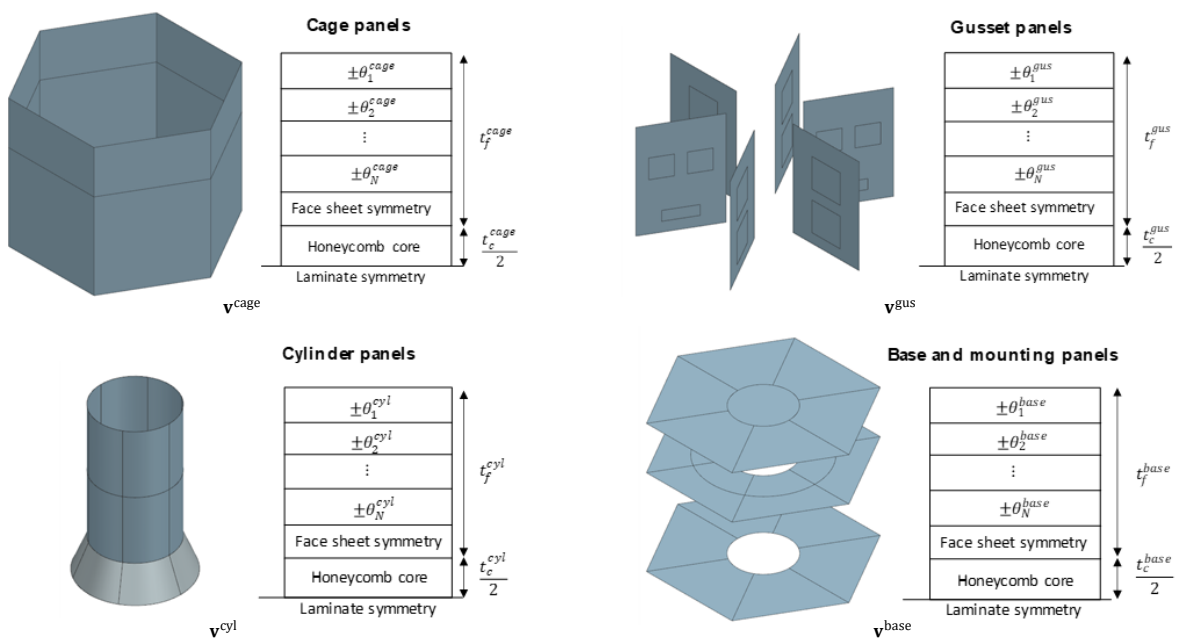

Figure 6.37: Design variable description for the optimization of spacecraft with lamination parameters.

The fiber orientations of each ply are chosen from set $\Theta \in \{\theta_1, \theta_2, \ldots, \theta_p\}$, the stacking sequence and the number of plies are retrieved from optimal lamination parameters $\mathbf{v}^*$ from step 2 formulation.

Here, A and D are extensional and bending stiffness obtained using optimum lamination parameter values $\mathbf{v}^*$, whereas $\hat{A}$ and $\hat{D}$ are extensional and bending stiffnesses obtained using lamination parameter expressions in binary variables $\mathbf{x}$. $l(\mathbf{x})$ are linear constraints corresponding to laminate design rules such as ply adjacency, balance and contiguity.

Step 2: Stiffness matching with integer linear programming to retrieve panel stacking sequence.

$$\begin{aligned}
&\textbf{Minimize:} && W(\mathbf{x}) \\
&\textbf{Subject to:} && l(\mathbf{x}) \leq 0 \\
& && \hat{A}^j\left(\hat{\mathbf{v}}^j(\mathbf{x})\right) \geq A^j\left(\mathbf{v}^{*j}\right) \\
& && \hat{D}^j\left(\hat{\mathbf{v}}^j(\mathbf{x})\right) \geq D^j\left(\mathbf{v}^{*j}\right) \\
& && \mathbf{x} \in \{0,1\}^p
\end{aligned}$$

6.4.4 MSADO Results with Lamination Parameters and Mixed Integer Programming

The spacecraft is optimized to get lamination parameters for each panel group using the MSADO framework. The results are compared with those obtained using direct optimization. Using lamination parameters reduces the number of panel design variables, and the resulting continuous design space significantly improves optimization performance, as seen from Fig 6.38. Moreover, it is able to obtain a better optimum of 576.08 kg with panel thicknesses given in Table 6.12. The reduction in mass from the direct method is expected as optimization with lamination parameters leads to idealized values of face sheet thickness which can only be obtained from a continuous distribution of fiber orientation through the thickness, i.e., infinite resolution of Θ with infinitely small ply thickness.

Table 6.12: Panel properties from optimization using lamination parameters (step 1).

Panel	Cage	Gusset	Cylinder	Base/Mount
t_f (mm)	0.6157	0.5867	0.9921	0.5578
t_c (mm)	12.5	12.5	12.5	12.5

The stacking sequence is retrieved for different resolutions of Θ and ply thicknesses to show convergence with step 1 results. The results obtained from step 2 are verified using a multidisciplinary analysis and checked for constraint satisfaction, including strength-based constraints. Tables 6.13 and 6.14 give optimal panel properties obtained using step 2. The

first case denotes the standard configuration used in direct optimization with fiber orientations discretized in the intervals of 45° and ply thickness of 0.0762 mm. The corresponding optimum number of plies per face sheet is specified in the first row of table 6.14. The configuration results in a mass of 589.58 kg, which is higher than that obtained using direct optimization. An advantage of this approach is that the fiber orientation resolutions and ply thicknesses can be varied without rerunning MSADO, i.e., step 1, which saves significant computational resources.

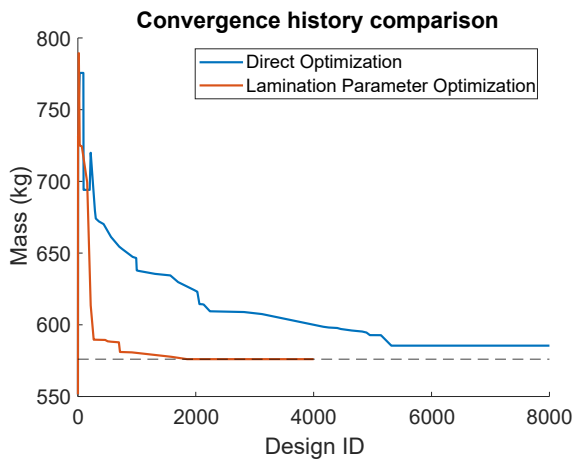

Figure 6.38: Convergence rate comparison between direct and lamination parameter based optimization.

Table 6.13: Stacking sequence retrieval results for different orientation and ply thickness resolutions.

Θ	t_{ply} (mm)	Mass (kg)	Retrieval time (s)
$\{0:45:90\}$	0.0762	589.58	0.39
$\{0:45:90\}$	0.0381	580.84	0.428
$\{0:5:90\}$	0.0762	584.73	0.872
$\{0:5:90\}$	0.0381	580.24	1.16
$\{0:5:90\}$	0.01	576.67	6.52
$\{0:5:90\}$	0.005	576.67	7.03

Reducing the ply thickness increases the number of plies to maintain the total panel thickness. It expands the design space with better possible solutions than the first case. As the

Table 6.14: Actual optimal spacecraft panel properties corresponding to studies in Table 6.13.

N^{cage}	t_f^{cage} (mm)	N^{gus}	t_f^{gus} (mm)	N^{cyl}	t_f^{cyl} (mm)	N^{base}	t_f^{base} (mm)
10	0.762	10	0.762	16	1.2192	10	0.762
18	0.6858	16	0.6096	30	1.143	16	0.6096
10	0.762	10	0.762	14	1.0668	8	0.6096
18	0.6858	16	0.6096	28	1.0668	16	0.6096
62	0.62	60	0.6	102	1.02	56	0.56
124	0.62	120	0.6	204	1.02	112	0.56

resolution of angles is improved further and ply thickness is reduced, the optimum configuration slowly converges to the ideal configuration obtained in step 1 with a mass of 576.67 kg. This can be seen by comparing values from Table 6.12 and Table 6.14. Stacking sequences retrieved from configurations in rows 2 through 6 yields better spacecraft designs compared to direct optimization for a fraction of the cost. Since mixed integer programming is used in step 2, it only takes a few seconds to retrieve stacking sequences, even if a large number of plies are used. The fewer evaluations required in step 1, combined with the negligible cost of step 2, make optimization using lamination parameters a promising approach for the multidisciplinary designing of large composite spacecraft structures.

Chapter 7

Summary and Future Work

7.1 Summary

The research tackles two problems in complex structural design. One is the seamless integration of different disciplines, and the other is the efficient optimization of composite panels from which most aerospace structures are made. The first part explores mixed integer programming (MIP) as an alternative to Genetic Algorithm (GA) and Particle Swarm Optimization (PSO) for composite laminate design. Three formulations are developed to optimize standard and hybrid laminates with fiber orientations, ply thickness, and the number of plies as design variables. The non-convex optimization problem of finding optimal fiber orientations is converted into the convex form using binary design variables and solved using integer programming algorithms. Optimizing a simply supported rectangular panel using closed-form solutions for buckling and strain constraints shows a significant improvement in performance and robustness over heuristic solvers like GA and PSO. Reformulation linearization techniques are used to exactly linearize quadratic and cubic constraints that are functions of binary variables. The use of distinct ply thickness expands the design space exponentially with respect to addition of a new binary variable but aids in obtaining a design with lower mass than that obtained from uniform ply thicknesses.

The integer programming formulation is employed to optimize structures analyzed using the finite element method. This is done using a two-step procedure where the lamination pa-

rameters are optimized first as continuous design variables, with the optimization subjected to various design constraints. The best stacking sequence is retrieved in step 2 using integer programming. Similar to previous studies, a significant reduction in computational effort is achieved with the two-step approach. The non-convex optimization problem is solved as two separate convex optimization problems resulting in the performance improvements and robustness.

A multidisciplinary structural design framework is built in part II that efficiently integrates structures, thermal and acoustic disciplines using commercial software like NX, HEEDS, and Simcenter 3D, and open-source python libraries like pyNastran. A small spacecraft's simplified finite element modeling is demonstrated along with its multidisciplinary design using the framework. A direct optimization is performed for various launch vehicle and in-orbit loads that comply with GEVS, SMC, and MIL 810E standards. It is found that the optimization is driven by the structure's stiffness which is the case for most global aerospace structural designs.

The lamination parameter formulation is extended to work with thermal-structural analysis. The formulations for thermal conductivities and coefficient of thermal expansion as functions of lamination parameters are demonstrated. It enables the use of heat-transfer and thermo-mechanical analysis to be performed using lamination parameters as design variables. The MSADO framework is used to optimized the small spacecraft with lamination parameters as design variables. Since the stacking sequence are retrieved using MIP, the overall optimization performance is vastly improved compared to the direct method.

A disadvantage of using lamination parameters in the optimization is that the ply level strength based constraints cannot be used. But, as demonstrated in this work, if the structural design is driven by stiffness, the lamination parameter optimization combined with MIP yields orders of magnitude improvement in the optimization performance by signif-

icantly reducing the number of design evaluation required till convergence and preventing complete re-optimization when the ply level design parameters (fiber orientation resolutions, ply thickness and maximum number of plies) are changed.

7.2 Future Research Avenues

The present work offers the potential for numerous other research avenues to be pursued. These ideas include, but are not limited to, investigating various applications and extensions of the current methodology, exploring new theoretical frameworks, and conducting further empirical studies. A few research directions possible with the current work are mentioned below.

- **Incorporating ply level strength based constraints in optimization with lamination parameters:** The optimum design obtained before the stacking sequence retrieval step is performed can be used to compute post optimality sensitivities of mid plane stresses or strains S_0 with respect to lamination parameter variables. A linear approximation of mid plane stresses/strains S can be constructed and then transformed using ply fiber orientation binary variables $\mathbf{x}$ to get corresponding ply level values S_{ply} as shown in Eqn (7.1).

$$\begin{aligned} S(\mathbf{x}) &= S_0 + \frac{\partial S_0}{\partial \mathbf{v}}(\mathbf{v}(\mathbf{x}) - \mathbf{v_0}) \\ S_{ply} &= T(\mathbf{x})S(\mathbf{x}) \end{aligned} \tag{7.1}$$

  The quadratic expressions for S_{ply} in terms of binary variables can be used as constraints in stacking sequence retrieval step with MIP. The formulation results in a large number of quadratic constraints depending on the size of the finite element model

and the number of plies in each element. An active set strategy must be devised that chooses only the constraints that are violated or near limit to reduce the optimization problem size.

- **Modeling composites panels with ply drops and blends:** In large scale structures such as aircraft wings, using ply drops and blends is a common design choice to alleviate stress discontinuities between different panels. To extend MIP based formulation to such cases, two sets of design variables can be used. A global set of binary variables can govern the base layup and local panel orientations can be chosen from the base layup using local sets of binary variables.

- **Stiffened composite panel designs:** The methods described in this research can be easily translated to the design of straight and curvilinearly stiffened panels.

- **Variable angled tow (VAT) laminates:** With a high resolution of fiber orientations values in set Θ, MIP can be used in designing VAT laminates where the spatial distribution of angles can be optimized using control points.

- **Multi-scale analysis for predicting fastener failure response in the MSADO framework:** The failure response at the fastener locations can be predicted with a greater accuracy by using a multi-scale analysis involving micro and macro scale damage simulations.

- **Modeling thermal protection systems:** The scope of this research is limited to using structural responses as optimization constraints. Since certain parts of the spacecraft must be kept within specified temperatures to prevent their failure, the use of thermal blankets and other protection layers can be explored.

Bibliography

[1] Douglass, B. P., *Agile Systems Engineering*, Morgan Kaufmann, 2015.

[2] Estefan, J. A. et al., "Survey of Model-based Systems Engineering (MBSE) Methodologies," *Incose MBSE Focus Group*, Vol. 25, No. 8, 2007, pp. 1–12.

[3] Eppinger, S. D. and Browning, T. R., *Design Structure Matrix Methods and Applications*, MIT press, 2012.

[4] Lambe, A. B. and Martins, J. R., "Extensions to the Design Structure Matrix for the Description of Multidisciplinary Design, Analysis, and Optimization Processes," *Structural and Multidisciplinary Optimization*, Vol. 46, No. 2, 2012, pp. 273–284.

[5] Zhao, W., Jrad, M., Gupta, R., and Kapania, R. K., "Multidisciplinary Design Analysis and Optimization of Performance Adaptive Aeroelastic Wings," *AIAA Atmospheric Flight Mechanics Conference*, 2017, p. 1392.

[6] Love, N. J. and Kapania, R. K., "Structural Optimization of a Novel Flying Wing Supersonic Aircraft Configuration," *AIAA Scitech 2020 Forum*, 2020, p. 0166.

[7] SpaceX, *Falcon User's Guide*, Space Exploration Technologies Corporation.

[8] Karakaya, Ş. and Soykasap, Ö., "Natural Frequency and Buckling Optimization of Laminated Hybrid Composite Plates using Genetic Algorithm and Simulated Annealing," *Structural and Multidisciplinary Optimization*, Vol. 43, No. 1, 2011, pp. 61–72.

[9] Meseguer, J., Pérez-Grande, I., and Sanz-Andrés, A., *Spacecraft Thermal Control*, Elsevier, 2012.

[10] Rumbaugh, J., *The Unified Modeling Language Reference Manual*, Pearson Education India, 2005.

[11] Group, O. M., "OMG SysML Specification," *OMG Adopted Specification, OMG Document ptc/06-05-04*, 2006.

[12] Friedenthal, S., "Object Oriented Systems Engineering," *Process Integration*, 2000.

[13] Lykins, H., Friedenthal, S., and Meilich, A., "Adapting UML for an Object Oriented Systems Engineering Method (OOSEM)," *INCOSE International Symposium*, Vol. 10, Wiley Online Library, 2000, pp. 490–497.

[14] Kruchten, P., *The Rational Unified Process: An Introduction*, Addison-Wesley Professional, 2004.

[15] Long, J. E., "Systems Engineering (SE) 101: CORE: Product & Process Engineering Solutions," *Vitech training materials, Vitech Corporation, Vienna, VA*, 2000.

[16] Dori, D., "Object-process Methodology," *Encyclopedia of Knowledge Management, Second Edition*, IGI Global, 2011, pp. 1208–1220.

[17] Mieloszyk, J. and Goetzendorf-Grabowski, T., "Introduction of Full Flight Dynamic Stability Constraints in Aircraft Multidisciplinary Optimization," *Aerospace Science and Technology*, Vol. 68, 2017, pp. 252–260.

[18] Martins, J. R. and Lambe, A. B., "Multidisciplinary Design Optimization: A Survey of Architectures," *AIAA journal*, Vol. 51, No. 9, 2013, pp. 2049–2075.

[19] Benaouali, A. and Kachel, S., "Multidisciplinary Design Optimization of Aircraft Wing using Commercial Software Integration," *Aerospace Science and Technology*, Vol. 92, 2019, pp. 766–776.

[20] Love, N. J., Kapania, R. K., and Allison, D. L., "Integrated Aircraft Parametric Structural & Outer Mold Line Geometry Modeling Software," *58th AIAA/ASCE/AHS/ASC Structures, Structural Dynamics, and Materials Conference*, 2017, p. 0800.

[21] Gur, O., Bhatia, M., Schetz, J. A., Mason, W. H., Kapania, R. K., and Mavris, D. N., "Design Optimization of a Truss-Braced-Wing Transonic Transport Aircraft," *Journal of aircraft*, Vol. 47, No. 6, 2010, pp. 1907–1917.

[22] Gupta, R., Love, N. J., Kapania, R. K., and Schmidt, D., "Development of Longitudinal Flight Dynamics Analysis Framework with Controllability and Observability Metrics," *2018 Multidisciplinary Analysis and Optimization Conference*, 2018, p. 3425.

[23] Sanmugadas, V., Gupta, R., Zhao, W., Kapania, R. K., and Schmidt, D. K., "Effect of Aeroelastic Tailoring of Composite Skin Laminates on Modal Controllability/Observability of Aircraft Structures," *AIAA Aviation 2021 Forum*, 2021, p. 3084.

[24] Budianto, I. A. and Olds, J. R., "Design and Deployment of a Satellite Constellation using Collaborative Optimization," *Journal of Spacecraft and Rockets*, Vol. 41, No. 6, 2004, pp. 956–963.

[25] Jilla, C. D. and Miller, D. W., "Multi-objective, Multidisciplinary Design Optimization Methodology for Distributed Satellite Systems," *Journal of Spacecraft and Rockets*, Vol. 41, No. 1, 2004, pp. 39–50.

[26] Hwang, J. T., Lee, D. Y., Cutler, J. W., and Martins, J. R., "Large-scale Multidisciplinary Optimization of a Small Satellite's Design and Operation," *Journal of Spacecraft and Rockets*, Vol. 51, No. 5, 2014, pp. 1648–1663.

[27] Wu, W., Huang, H., Chen, S., and Wu, B., "Satellite Multidisciplinary Design Op-

timization with a High-fidelity Model," *Journal of Spacecraft and Rockets*, Vol. 50, No. 2, 2013, pp. 463–466.

[28] Thornton, E. and Foster, R., "Dynamic Response of Rapidly Heated Space Structures," *33rd Structures, Structural Dynamics and Materials Conference*, 1992, p. 2207.

[29] Thornton, E. A. and Kim, Y. A., "Thermally Induced Bending Vibrations of a Flexible Rolled-up Solar Array," *Journal of Spacecraft and Rockets*, Vol. 30, No. 4, 1993, pp. 438–448.

[30] Chung, P. and Thornton, E., "Torsional Buckling and Vibrations of a Flexible Rolled-up Solar Array," *36th Structures, Structural Dynamics and Materials Conference*, 1995, p. 1355.

[31] Murozono, M. and Thornton, E. A., "Buckling and Quasistatic Thermal-structural Response of Asymmetric Rolled-up Solar Array," *Journal of spacecraft and rockets*, Vol. 35, No. 2, 1998, pp. 147–155.

[32] Xue, M.-D., Duan, J., and Xiang, Z.-H., "Thermally-induced Bending-torsion Coupling Vibration of Large Scale Space Structures," *Computational Mechanics*, Vol. 40, No. 4, 2007, pp. 707–723.

[33] Agrawal, O. and Shabana, A., "Application of Deformable-body Mean Axis to Flexible Multibody System Dynamics," *Computer Methods in Applied Mechanics and Engineering*, Vol. 56, No. 2, 1986, pp. 217–245.

[34] Apiwattanalunggarn, P., Shaw, S. W., and Pierre, C., "Component Mode Synthesis using Nonlinear Normal Modes," *Nonlinear Dynamics*, Vol. 41, No. 1, 2005, pp. 17–46.

[35] Nikravesh, P. E. and Lin, Y.-S., "Use of Principal Axes as the Floating Reference

Frame for a Moving Deformable Body," *Multibody System Dynamics*, Vol. 13, No. 2, 2005, pp. 211–231.

[36] Friberg, O., "A Method for Selecting Deformation Modes in Flexible Multibody Dynamics," *International Journal for Numerical Methods in Engineering*, Vol. 32, No. 8, 1991, pp. 1637–1655.

[37] Ambrósio, J., "Geometric and Material Nonlinear Deformations in Flexible Multibody Systems," 2001.

[38] Weeger, O., Wever, U., and Simeon, B., "On the use of Modal Derivatives for Nonlinear Model Order Reduction," *International Journal for Numerical Methods in Engineering*, Vol. 108, No. 13, 2016, pp. 1579–1602.

[39] Bauchau, O. A. and Rodriguez, J., "Formulation of Modal-based Elements in Nonlinear, Flexible Multibody Dynamics," *International Journal for Multiscale Computational Engineering*, Vol. 1, No. 2&3, 2003.

[40] Wu, L. and Tiso, P., "Nonlinear Model Order Reduction for Flexible Multibody Dynamics: A Modal Derivatives Approach," *Multibody System Dynamics*, Vol. 36, No. 4, 2016, pp. 405–425.

[41] Nikravesh, P. E. and Ambrosio, J. A., "Systematic Construction of Equations of Motion for Rigid-flexible Multibody Systems Containing Open and Closed Kinematic Loops," *International Journal for Numerical Methods in Engineering*, Vol. 32, No. 8, 1991, pp. 1749–1766.

[42] Shabana, A. A., "Flexible Multibody Dynamics: Review of Past and Recent Developments," *Multibody System Dynamics*, Vol. 1, No. 2, 1997, pp. 189–222.

[43] Yun, H., Liu, L., Li, Q., and Yang, H., "Investigation on Two-stage Vibration Suppression and Precision Pointing for Space Optical Payloads," *Aerospace Science and Technology*, Vol. 96, 2020, pp. 105543.

[44] Likins, P. W., "Dynamics and Control of Flexible Space Vehicles," 1970.

[45] Hughes, P. C. and Skelton, R. E., "Controllability and Observability for Flexible Spacecraft," *Journal of Guidance and Control*, Vol. 3, No. 5, 1980, pp. 452–459.

[46] Le Riche, R. and Haftka, R. T., "Optimization of Laminate Stacking Sequence for Buckling Load Maximization by Genetic Algorithm," *AIAA Journal*, Vol. 31, No. 5, 1993, pp. 951–956.

[47] Le Riche, R. and Haftka, R. T., "Improved Genetic Algorithm for Minimum Thickness Composite Laminate Design," *Composites Engineering*, Vol. 5, No. 2, 1995, pp. 143–161.

[48] Bargh, H. G. and Sadr, M., "Stacking Sequence Optimization of Composite Plates for Maximum Fundamental Frequency using Particle Swarm Optimization Algorithm," *Meccanica*, Vol. 47, No. 3, 2012, pp. 719–730.

[49] Haftka, R. T. and Gürdal, Z., *Elements of Structural Optimization*, Vol. 11, Springer Science & Business Media, 2012.

[50] Omkar, SN., Mudigere, D., Naik, G. N., and Gopalakrishnan, S., "Vector Evaluated Particle Swarm Optimization (VEPSO) for Multi-Objective Design Optimization of Composite Structures," *Computers & Structures*, Vol. 86, No. 1-2, 2008, pp. 1–14.

[51] Omkar, SN., Khandelwal, R., Ananth, T., Naik, G. N., and Gopalakrishnan, S., "Quantum Behaved Particle Swarm Optimization (QPSO) for Multi-Objective Design Opti-

mization of Composite Structures," *Expert Systems with Applications*, Vol. 36, No. 8, 2009, pp. 11312–11322.

[52] Chang, N., Wang, W., Yang, W., and Wang, J., "Ply Stacking Sequence Optimization of Composite Laminate by Permutation Discrete Particle Swarm Optimization," *Structural and Multidisciplinary Optimization*, Vol. 41, No. 2, 2010, pp. 179–187.

[53] Erdal, O. and Sonmez, F. O., "Optimum Design of Composite Laminates for Maximum Buckling Load Capacity using Simulated Annealing," *Composite Structures*, Vol. 71, No. 1, 2005, pp. 45–52.

[54] Deng, S., Pai, P.-F., Lai, C.-C., and Wu, P.-S., "A Solution to the Stacking Sequence of a Composite Laminate Plate with Constant Thickness using Simulated Annealing Algorithms," *The International Journal of Advanced Manufacturing Technology*, Vol. 26, No. 5-6, 2005, pp. 499–504.

[55] Akbulut, M. and Sonmez, F. O., "Design Optimization of Laminated Composites using a New Variant of Simulated Annealing," *Computers & Structures*, Vol. 89, No. 17-18, 2011, pp. 1712–1724.

[56] Schmit, L. A. and Mehrinfar, M., "Multilevel Optimum Design of Structures with Fiber-Composite Stiffened-Panel Components," *AIAA Journal*, Vol. 20, No. 1, 1982, pp. 138–147.

[57] Liu, B., Haftka, R. T., and Akgün, M. A., "Two-level Composite Wing Structural Optimization using Response Surfaces," *Structural and Multidisciplinary Optimization*, Vol. 20, No. 2, 2000, pp. 87–96.

[58] Kapania, R. K., Li, J., and Kapoor, H., "Optimal Design of Unitized Panels with

Curvilinear Stiffeners," *AIAA 5th ATIO and16th Lighter-Than-Air Sys Tech. and Balloon Systems Conferences*, 2005, p. 7482.

[59] Locatelli, D., Mulani, S. B., and Kapania, R. K., "Wing-box Weight Optimization using Curvilinear Spars and Ribs (SpaRibs)," *Journal of Aircraft*, Vol. 48, No. 5, 2011, pp. 1671–1684.

[60] Liu, Q., Jrad, M., Mulani, S. B., and Kapania, R. K., "Global/local Optimization of Aircraft Wing using Parallel Processing," *AIAA Journal*, 2016, pp. 3338–3348.

[61] Zhao, W. and Kapania, R. K., "BLP Optimization of Composite Flying-wings with Sparibs and Multiple Control Surfaces," *2018 AIAA/ASCE/AHS/ASC Structures, Structural Dynamics, and Materials Conference*, 2018, p. 2150.

[62] Wolsey, L. A., *Integer Programming*, Vol. 52, John Wiley & Sons, 1998.

[63] Haftka, R. T. and Walsh, J. L., "Stacking-Sequence Optimization for Buckling of Laminated Plates by Integer Programming," *AIAA Journal*, Vol. 30, No. 3, 1992, pp. 814–819.

[64] Shahabsafa, M., Mohammad-Nezhad, A., Terlaky, T., Zuluaga, L., He, S., Hwang, J. T., and Martins, J. R., "A Novel Approach to Discrete Truss Design Problems using Mixed Integer Neighborhood Search," *Structural and Multidisciplinary Optimization*, Vol. 58, No. 6, 2018, pp. 2411–2429.

[65] Zein, S. and Bruyneel, M., "A Bilevel Integer Programming Method for Blended Composite Structures," *Advances in Engineering Software*, Vol. 79, 2015, pp. 1–12.

[66] Chang, C.-T., "An Efficient Linearization Approach for Mixed-Integer Problems," *European Journal of Operational Research*, Vol. 123, No. 3, 2000, pp. 652–659.

[67] Adams, W. P. and Forrester, R. J., "A Simple Recipe for Concise Mixed 0-1 Linearizations," *Operations Research Letters*, Vol. 33, No. 1, 2005, pp. 55–61.

[68] Herencia, J. E., Haftka, R. T., Weaver, P. M., and Friswell, M. I., "Lay-up Optimization of Composite Stiffened Panels using Linear Approximations in Lamination Space," *AIAA Journal*, Vol. 46, No. 9, 2008, pp. 2387–2391.

[69] Peeters, D., van Baalen, D., and Abdallah, M., "Combining Topology and Lamination Parameter Optimisation," *Structural and Multidisciplinary Optimization*, Vol. 52, No. 1, 2015, pp. 105–120.

[70] Fedon, N., Weaver, P. M., Pirrera, A., and Macquart, T., "A Method using Beam Search to Design the Lay-ups of Composite Laminates with Many Plies," *Composites Part C: Open Access*, Vol. 4, 2021, pp. 100072.

[71] Software, S. D. I., "Getting Started with HEEDS," 2022.

[72] Doyle, S., Danial, A., and Gasiorek, M., "PyNastran: A Python-based Interface Tool for Nastran's File Formats," *User Manual, Release 0.8-dev*, 2016.

[73] Tsai, S. W. and Pagano, N. J., "Invariant Properties of Composite Materials." Technical Report, Air Force Materials Lab Wright-Patterson AFB Ohio, 1968.

[74] Borwankar, P., Zhao, W., Kapania, R. K., and Bansal, M., "Two-level Weight Optimization of Composite Laminates using Integer Programming," *AIAA Journal*, 2022, pp. 1–11.

[75] Reddy, J. N., *Theory and Analysis of Elastic Plates and Shells*, CRC press, 2006.

[76] Galos, J., "Thin-ply Composite Laminates: A Review," *Composite Structures*, Vol. 236, 2020, pp. 111920.

[77] Gurobi Optimization, L., "Gurobi Optimizer Reference Manual," 2020.

[78] Kretsis, G., "A Review of the Tensile, Compressive, Flexural and Shear Properties of Hybrid Fibre-Reinforced Plastics," *Composites*, Vol. 18, No. 1, 1987, pp. 13–23.

[79] Glover, F., "Improved Linear Integer Programming Formulations of Nonlinear Integer Problems," *Management Science*, Vol. 22, No. 4, 1975, pp. 455–460.

[80] Soremekun, G., Gürdal, Z., Haftka, R., and Watson, L., "Composite Laminate Design Optimization by Genetic Algorithm with Generalized Elitist Selection," *Computers & Structures*, Vol. 79, No. 2, 2001, pp. 131–143.

[81] Fukunaga, H. and Vanderplaats, G. N., "Stiffness Optimization of Orthotropic Laminated Composites using Lamination Parameters," *AIAA Journal*, Vol. 29, No. 4, 1991, pp. 641–646.

[82] Bloomfield, M. W., Herencia, J. E., and Weaver, P. M., "Enhanced Two-level Optimization of Anisotropic Laminated Composite Plates with Strength and Buckling Constraints," *Thin-Walled Structures*, Vol. 47, No. 11, 2009, pp. 1161–1167.

[83] Albazzan, M. A., Harik, R., Tatting, B. F., and Gürdal, Z., "Efficient Design Optimization of Nonconventional Laminated Composites using Lamination Parameters: A State of the Art," *Composite Structures*, Vol. 209, 2019, pp. 362–374.

[84] Macquart, T., Maes, V., Bordogna, M. T., Pirrera, A., and Weaver, P. M., "Optimisation of Composite Structures–Enforcing the Feasibility of Lamination Parameter Constraints with Computationally-efficient Maps," *Composite Structures*, Vol. 192, 2018, pp. 605–615.

[85] Bloomfield, M. W., Diaconu, C., and Weaver, P., "On Feasible Regions of Lamination Parameters for Lay-up Optimization of Laminated Composites," *Proceedings of the*

Royal Society A: Mathematical, Physical and Engineering Sciences, Vol. 465, No. 2104, 2009, pp. 1123–1143.

[86] Software, S. D. I., "Discovering NX," 2022.

[87] Software, S. D. I., "Simcenter Nastran Quick Reference Guide," 2022.

[88] Abdelal, G. F., Abuelfoutouh, N., and Gad, A. H., *Finite Element Analysis for Satellite Structures: Applications to their Design, Manufacture and Testing*, Springer Science & Business Media, 2012.

[89] Craig Jr, R. R. and Bampton, M. C., "Coupling of Substructures for Dynamic Analyses." *AIAA Journal*, Vol. 6, No. 7, 1968, pp. 1313–1319.

[90] Smallwood, D. O. et al., "An Improved Recursive Formula for Calculating Shock Response Spectra," *Shock and Vibration Bulletin*, Vol. 51, No. 2, 1981, pp. 211–217.

[91] Hambric, S. A., Sung, S. H., and Nefske, D. J., *Engineering Vibroacoustic Analysis: Methods and Applications*, John Wiley & Sons, 2016.

[92] Lewis, R. W., Nithiarasu, P., and Seetharamu, K. N., *Fundamentals of the Finite Element Method for Heat and Fluid Flow*, John Wiley & Sons, 2004.

[93] Stevenson, J. and Grafton, J., "Radiation Heat Transfer Analysis for Space Vehicles," Tech. rep., North American Aviation Inc Downey CA, 1961.

[94] Red Cedar Technology, "SHERPA – An Efficient and Robust Optimization/Search Algorithm," Tech. rep.

[95] National Aeronautics and Space Administration, "General Environmental Verification Standard (GEVS) for GSFC Flight Programs and Projects," 2021.

[96] Air Force Space Command, "Space and Missile System Center Standard," 2014.

[97] U.S. Department of Defense, "Environmental Test Methods and Engineering Guidelines," 1989.

[98] Planetary Systems Corporation, *2000785G MkII MLB User Manual*, Planetary Systems Corp.

[99] Irvine, T., "Shock Response Spectrum Synthesis via Wavelets," Tech. rep., Vibrationdata, 08 2000.

[100] Carlsson, L. A. and Kardomateas, G. A., *Structural and Failure Mechanics of Sandwich Composites*, Vol. 121, Springer Science & Business Media, 2011.

[101] National Aeronautics and Space Administration, "Requirements for Threaded Fastening Systems in Spaceflight Hardware," 2021.

[102] Miller, A. K., "Thermal Expansion Coefficients for Laminates Obtained from Invariant Lamina Properties," *Fibre Science and Technology*, Vol. 13, No. 5, 1980, pp. 397–409.

[103] Silva, G. H. and Meddaikar, Y., "Lamination Parameters for Sandwich and Hybrid Material Composites," *AIAA Journal*, Vol. 58, No. 10, 2020, pp. 4604–4611.